

Structure-property relationships in PVC-lubricant compounds

by

Johannes Lodewiekus Barnard

*Dissertation presented for the degree of Doctor of Science in the Faculty of Chemistry and
Polymer Science at Stellenbosch University*

The crest of Stellenbosch University is a shield with a red border. The shield is divided into four quadrants: top-left is red with a white cross, top-right is blue with a white cross, bottom-left is yellow with a red cross, and bottom-right is blue with a white cross. The shield is flanked by two red lions. Above the shield is a crown.

Supervisor:

Prof. A.J. van Reenen

Co-supervisor:

Dr. D.D. Robertson

March 2021

Declaration

By submitting this dissertation electronically, I declare that the entirety of the work contained therein is my own, original work, that I am the sole author thereof (save to the extent explicitly otherwise stated), that reproduction and publication thereof by Stellenbosch University will not infringe any third party rights and that I have not previously in its entirety or in part submitted it for obtaining any qualification.

J.L. Barnard

January 2021

Copyright © 2021 Stellenbosch University

All rights reserved

Abstract

This thesis was constructed with the aim of developing and improving current methods for tracking lubricants during the single screw extrusion of unplasticized polyvinyl chloride (uPVC).

First a set of commercial waxes were selected to develop this method. These waxes were sourced from industries making use of different production technologies and therefore varied widely in chemical composition and morphology.

The lubricant behaviour was monitored over three stages. In stage 1, it was essential to fully characterize the waxes according to their chemical composition and morphological properties. During stage 2, it was necessary to evaluate any inherent chemical or physical association interactions between any of the components within a uPVC formulation. For stage 3, full uPVC formulations were extruded using a single screw Brabender extruder and subsequently analysed.

In stage 1 the waxes were characterized using various analytical techniques such as High-temperature size exclusion chromatography (HT-SEC), attenuated total reflectance Fourier transform infrared (ATR-FTIR) spectroscopy, ^{13}C nuclear magnetic resonance (^{13}C -NMR) spectroscopy, solid state NMR (SS-NMR), differential scanning calorimetry (DSC) and, X-ray diffraction (XRD) spectroscopy. In stage 2, uPVC formulations were hot-melt mixed at high speed and evaluated using scanning electron microscopy coupled to energy dispersive X-ray spectroscopy (SEM-EDS). This allowed for the effective determination of additive positions before extrusion. In stage 3 the extrudates were also analysed using SEM-EDS. This technique helped to establish the additive positions after PVC fusion, effectively tracking additive migration. At this point it was established that calcium stearate (CaSt) facilitated the dispersion of the nonpolar wax across the surface of a PVC particle and that there exists a competition effect between polar waxes and CaSt. The extrudates showed some interesting results such as a complete phase separation for formulations containing CaSt and a polar wax.

The method was further refined using a screw-freezing technique which allowed in-extruder sampling to be done. The method was applied to a second set of polar and nonpolar waxes (Wax set 2). No trends could be observed at this stage due to the waxes differing too much in chemical composition and morphology. It was therefore decided to synthesize a new set of polar waxes and fully characterize them.

A new set of waxes were successfully synthesized by ozonolysis of FT (Fischer-Tropsch) waxes. These waxes were fully characterized, and an attempt was made to track the lubricants' migration. Migration could not be track and the samples were subjected to commercial testing. Through combining the stage 3 experiments and commercial fusion studies a deeper understanding of the currently accepted model for lubricant migration was gained. Additionally, the model was expanded to include the effect of oxidized waxes.

Acknowledgements

I would like to take this opportunity to thank my family, Vic, Mandi, and Yolandi for their continued love, support and inspiration during this time. I would not have been able to do this without you.

To Prof van Reenen, it has been a complete privilege and amazing experience to work under your guidance for so long. Your positivity and friendliness create a wonderful working environment for everyone around you. Thank you for always being available for some (a lot of) advice not only academically but also in life.

To Dr Divann Robertson, thank you for not only being an awesome mentor but also a true friend. I can only hope that some of your work ethic and light heartedness has rubbed off on me. Thank you for all your patience with me, I know it must have been difficult at times. Thank you for all the time spent in planning of experiments and editing of documents.

I would also like to thank the olefins group for being the best study group in the world, this thesis was definitely a team effort. Special thanks to Ben for helping me to fix the Brabender. Thank you, Megan, for the long hours spent in figuring out the NMR experiments. Thank you, Anthony, for running all the chromatography experiments. I would also like to thank Heidi Duveskog (Contextualize Pty. Ltd) for project planning and guidance.

Thanks to all my friends and the Malans for your undeniable support. Thank you to Dr Rudolf Dreyer for starting and finishing this journey with me. It has been a privilege to gain a lifetime friend.

To Hildegard du Plessis, thanks for all your guidance, love and inspiration during the tough times. You have kept me focussed and goal driven which made everything much easier. I look forward to our journey together as I know that with you by my side, we will be able to achieve any goal on any journey that we embark upon.

Table of contents

Abstract	i
Acknowledgements	iii
Table of contents	iv
List of Figures	ix
List of Tables	xiii
List of abbreviations.....	xiv
Introduction.....	1
Chapter 1: Background.....	2
1.1 Industrial importance.....	2
1.2 PVC polymerisation	2
1.3 PVC Processing.....	3
1.4 PVC Additives.....	4
1.5 Lubrication	5
1.6 Previous studies on the mechanism of lubrication.	6
1.7 Types of waxes and their production	7
1.7.1 Petroleum derived waxes	8
1.7.2 Fisher-Tropsch wax	8
1.7.3 Functionalized waxes.....	9
Chapter 2: Method development	10
2.1 Outline for method development.....	10
2.2 Stage 1 (Wax set 1)	12
2.3 Experimental: Stage 1	13
2.3.1 High temperature – size exclusion chromatography (HT-SEC).....	13
2.3.2 Attenuated total reflectance – Fourier transform infrared spectroscopy (ATR-FTIR)	14
2.3.3 ¹³ C Nuclear magnetic resonance (¹³ C-NMR)	14
2.3.4 Solid-state NMR (SS-NMR).....	14

2.3.4	Differential scanning calorimetry (DSC).....	15
2.3.5	X-ray Diffraction (XRD)	15
2.4	Experimental: Stage 2	15
2.4.1	Scanning electron microscopy – Energy dispersive x-ray spectrometry (SEM-EDS)	16
2.5	Experimental: Stage 3	16
Chapter 3:	Method development: Results and discussion	18
3.1	Stage 1 (Wax set 1)	18
3.1.1	High temperature size exclusion chromatography (HT-SEC).....	18
3.1.2	Attenuated total reflection Fourier transform infrared spectroscopy (ATR-FTIR)	19
3.1.3	¹³ C Nuclear magnetic resonance spectroscopy (¹³ C NMR).....	24
3.1.4	Solid-state NMR (SS-NMR).....	24
3.1.5	X-Ray diffraction (XRD).....	27
3.1.6	Differential scanning calorimetry (DSC).....	29
3.1.7	Concluding remarks for stage 1 of the method development	31
3.2	Results and discussion of stage 2	31
3.2.1	Scanning electron microscopy (SEM)	31
3.2.2	Scanning electron microscopy – energy dispersive X-ray spectroscopy (SEM-EDS)	32
3.2.3	Association interactions using DSC.....	34
3.2.4	Concluding remarks for stage 2 of the method development	37
3.3	Results and discussion of stage 3	37
3.3.1	Concluding remarks for stage 3 of the method development	39
Chapter 4:	Method application	40
4.1	Binary blends.....	40
4.1.1	Stage 2.....	40
4.1.2	Stage 3.....	41

4.2	Ternary blends.....	42
4.2.1	Stage 2.....	42
4.2.2	Stage 3.....	44
4.3	Concluding remarks to Chapter 4.....	45
Chapter 5: Peer-reviewed manuscript published in Polymer Testing journal		46
5.1	Introduction	47
5.2	Materials and methods	49
5.2.1	Materials	49
5.2.2	Technique.....	49
5.3	Experimental	49
5.3.1	Sample preparation for all three stages:.....	49
5.3.1.1	Stage I.....	49
5.3.1.2	Stage II	49
5.3.1.3	Stage III.....	50
5.3.2	Sample characterization techniques.....	51
	Stage I	51
5.3.2.1	High temperature – size exclusion chromatography (HT-SEC)	51
5.3.2.2	Attenuated total reflectance – Fourier transform infrared spectroscopy (ATR-FTIR)	51
5.3.2.3	¹³ C Nuclear magnetic resonance (¹³ C-NMR).....	51
5.3.2.4	Differential scanning calorimetry (DSC)	51
	Stage II and III	52
5.3.2.5	Scanning electron microscopy – Energy dispersive x-ray spectrometry (SEM-EDS)	52
5.4	Results and discussion.....	52
	Stage I	52
	Stage II.....	56
	Stage III.....	58

5.5	Conclusion.....	61
Chapter 6:	Method improvement.....	62
6.1	Applying the screw freezing technique.....	62
6.2	Selection of Wax set 2.....	67
6.3	Results and discussion of stage 1 (Wax set 2)	68
6.3.1	HT-SEC.....	68
6.3.2	Attenuated total reflectance – Fourier transform infrared spectroscopy (ATR-FTIR)	69
6.3.3	Differential scanning calorimetry (DSC).....	69
6.3.4	¹³ C Nuclear magnetic resonance (¹³ C-NMR)	71
6.4	Results and discussion of stage 2 (Wax set 2)	71
6.5	Results and discussion of stage 3 (Wax set 2)	75
6.6	Concluding remarks to the method improvement chapter	77
Chapter 7:	Method refinement and commercial testing	78
7.1	Oxidized wax synthesis (Wax set 3)	78
7.2	Experimental for stage 1 (Wax set 3):.....	82
7.2.1	High temperature - Solvent gradient interaction chromatography (HT-SGIC)	82
7.3	Results and discussion of stage 1 (Wax set 3)	83
7.3.1	Quantitative ¹³C Nuclear magnetic resonance spectroscopy (¹³C NMR) ...	83
7.3.2	Differential scanning calorimetry (DSC).....	86
7.3.4	High temperature - size exclusion chromatography (HT-SEC).....	90
7.3.5	High temperature - solvent gradient interaction chromatography (HT-SGIC)..	93
7.3.5.1	Reverse phase HT-SGIC.....	93
7.3.5.2	Normal phase HT-SGIC.....	95
7.4	Results and discussion of stage 2 (Wax set 3)	97
7.5	Results and discussion of stage 3 (Wax set 3)	100
7.6	Commercial application (Fusion testing).....	101
7.7	Association interactions using SS NMR.....	107

7.8 Concluding remarks	109
General conclusion and suggestions for future studies	111
List of references.....	113

List of Figures

Figure 1.1: Schematic view of a single screw extruder ¹⁸ showing the; 1) feeding zone, 2) compression zone and, 3) metering zone.	4
Figure 1.2: Schematic of surfactants and slip agents proposed by Rabinovitch et al. ³¹	6
Figure 3.1: HT-SEC chromatograms of waxes in a) category 1 and b) category 2.	18
Figure 3.2: FTIR absorbance range of Methylene (CH ₂) and methyl (CH ₃) stretching regions.	21
Figure 3.3: Methylene scissoring and rocking vibrations of slow cooled and quench cooled polyethylenes ⁵⁵	22
Figure 3.4: Normalized methylene a) scissoring and b) rocking bands.	23
Figure 3.5 ATR-FTIR spectra of a) A typical hydrocarbon wax sample and b) A high density polyethylene polymer.	23
Figure 3.6: ATR-FTIR carbonyl (C=O) stretching and alkene (C=C) stretching vibrations...23	
Figure 3.7: ¹³ C-NMR spectra of a) highly linear, b) branched and unsaturated, and c) oxidised waxes.	25
Figure 3.8: ¹³ C CP-MAS NMR spectra of Wax set 1.	26
Figure 3.9: ¹ H Wideline spectra of Wax set 1.....	26
Figure 3.10: A typical XRD diffractogram obtained for the waxes (W52 sample illustrated).	27
Figure 3.11: Crystallite sizes of waxes calculated from each crystal plane.	28
Figure 3.12: DSC melting endotherms of a) lower melting waxes (group 1) and b) higher melting waxes (group 2).	29
Figure 3.13: DSC thermogram of neat PVC showing its glass transition event.	30
Figure 3.14: SEM electron images of a) PVC, b) PVC : CaSt, c) PVC : J75, d) PVC : CaSt : J75, e) PVC : Ceranox 40L90. Scalebar = 20 µm.....	32
Figure 3.15: SEM-EDS images of PVC blends. a) PVC, b) PVC : CaSt, c) PVC : J75, d) PVC : CaSt : J75, e) PVC : Ceranox 40L90. (Scalebar = 100 µm, Chlorine = blue, Carbon = red, Calcium = purple, Oxygen = green)	34
Figure 3.16: T _g of PVC with varying concentration of CaSt.	35
Figure 3.17: DSC melting endotherm overlays, a) J75 series and b) J100 series.....	36
Figure 3.18: A typical DSC cycle of J100 showing the disappearance of CaSt monohydrate peak at 127 °C.....	37
Figure 3.19: Example of an extruded rod and cross section imbedded in an epoxy resin.	38

Figure 3.20: SEM-EDS images of rods from blends a) PVC (carbon signal), b) PVC (chlorine signal) c) PVC : CaSt, d) PVC : J75, e) PVC : CaSt : J75, f) PVC : Ceranox 40L90. (Scalebar = 2 mm, Chlorine = blue, Carbon = red)	39
Figure 4.1: SEM-EDS images of binary PVC : Wax blends during Stage 2: a) W52; b) J100; c) J75; d) Marcus 300; e) FRP; f) PAO; g) Microwax; h) Ceranox 28L56; i) Ceranox 40L90. Electron image = grey (A). Chloride = blue (B); Carbon = red (C). Scalebar = 20µm.....	41
Figure 4.2: SEM-EDS images of binary PVC:Wax blends during Stage 3. a) W52; b) J100; c) J75; d) Marcus 300; e) FRP; f) PAO; g) Microwax; h) Ceranox 28L56; i) Ceranox 40L90. Electron image = grey (A). Chloride = blue (B); Carbon = red (C). Scalebar = 2mm.....	42
Figure 4.3: SEM-EDS images of ternary PVC : CaSt : Wax blends during Stage 2. a) W52; b) J100; c) J75; d) Marcus 300; e) FRP; f) PAO; g) Microwax; h) Ceranox 28L56; i) Ceranox 40L90. Electron image = grey (A). Chloride = blue (B); Carbon = red (C); Calcium = purple. Scalebar = 2 mm.....	43
Figure 4.4: SEM-EDS images of ternary PVC : CaSt : Wax blends during Stage 3. a) W52; b) J100; c) J75; d) Marcus 300; e) FRP; f) PAO; g) Microwax; h) Ceranox 28L56; i) Ceranox 40L90. Electron image = grey (A). Chloride = blue (B); Carbon = red (C); Calcium = purple (D). Scalebar = 2mm.	44
Figure 5.1: DSC thermograms for polar and nonpolar waxes, a) melting endotherms and b) crystallization exotherms.....	54
Figure 5.2: ATR-FTIR spectra for both waxes.	55
Figure 5.3: ¹³ C-NMR spectra for both waxes.	55
Figure 6.1: Burgess et al. ¹⁷ showing identical fields of view for a) light microscope images, b) fluorescent microscope images along the extruder screw. Arrow = extrusion direction. Scalebar = 100 µm.....	63
Figure 6.2: Section of a pulled screw filled with PVC formulation. Polymer flow is shown in the direction of the velocity arrow.	63
Figure 6.3: SEM-EDS images of screw freezing technique. Sample = PVC : CaSt : J75 (100 : 5 : 10). Electron image = Grey; Chloride = Blue; Carbon = red. Calcium = purple. Scalebar = 2 mm.	66
Figure 6.4: Electron images of PVC particles during stage 2 for the a) extrusion method and b) screw freezing method. PVC = light grey; Wax = dark grey. Scalebar = 20 µm.	67
Figure 6.5: HT-SEC results of a) nonpolar and b) polar waxes.....	68

Figure 6.6: ATR-FTIR spectra of a) nonpolar; b) polar and c) carbonyl absorbance of polar waxes.	70
Figure 6.7: DSC thermograms of a) nonpolar and b) polar waxes.	70
Figure 6.8: Solution ¹³ C-NMR Spectra of a) nonpolar waxes and b) polar waxes.	72
Figure 6.9: SEM-EDS images of binary blends of nonpolar waxes. a) FRP; b) FT; c) Microwax; d) PAO. Carbon = red. Scalebar = 400 μm.	73
Figure 6.10: SEM-EDS images of ternary blends of nonpolar waxes. a) FRP; b) FT; c) Microwax; d) PAO. Carbon = red. Calcium = purple. Scalebar = 400 μm	74
Figure 6.11: SEM-EDS images of binary blends of polar waxes. a) oHDPE; b) oLDPE; c) oFT28; d) oFT40. Carbon = red. Scalebar = 400 μm.	74
Figure 6.12: SEM-EDS images of ternary blends of polar waxes. a) oHDPE; b) oLDPE; c) Sasol A28; d) Ceranox 40L90. Carbon = red. Calcium = purple. Scalebar = 400 μm.	75
Figure 6.13: SEM-EDS images of binary blends (left) of nonpolar waxes. a) FRP; b) FT; c) Microwax; d) PAO and ternary blends (right) of nonpolar waxes e) FRP; f) FT; g) Microwax; h) PAO. Chloride = blue. Carbon = red. Calcium = purple. Scalebar = 2 mm.	76
Figure 6.14: FRP ternary blend showing calcium and carbon signal association.	76
Figure 6.15: SEM-EDS images of binary blends (left) of polar waxes a) oHDPE; b) oLDPE; c) oFT28; d) oFT40 and ternary blends (right) of polar waxes e) oHDPE; f) oLDPE; g) oFT28; h) oFT40. Carbon = red. Calcium = purple. Scalebar = 2 mm.	77
Figure 7.1: ATR-FTIR spectra of oJ75_40 and Ceranox 40L90. The absorbance ranges shown are for the a) full, b) hydroxyl and c) carbonyl regions.	80
Figure 7.2: ATR-FTIR spectra of oJ100_40 and Ceranox 40L90. The absorbance ranges shown are for the a) full, b) hydroxyl and c) carbonyl regions.	81
Figure 7.3: ATR-FTIR spectra showing the progression of oxidation during ozonolysis.	82
Figure 7.4: Enlarged ¹³ C NMR Spectroscopy results of a) upfield and b) downfield chemical shift regions for J75 samples.	85
Figure 7.5 Enlarged ¹³ C NMR Spectroscopy results of a) upfield and b) downfield chemical shift regions for J100 samples.	85
Figure 7.6: DSC melting thermograms showing the effect of oxidation on melting behaviour of a) J75 and b) J100 waxes.	89
Figure 7.7: DSC crystallization thermograms showing the effect of oxidation on crystallization behaviour of a) J75 and b) J100 waxes.	90

Figure 7.8: HT-SEC chromatograms of a) J75 and b) J100 waxes.....	92
Figure 7.9: Reverse phase HT-SGIC elution profiles for the J75 sample set.	94
Figure 7.10: Reverse-phase HT-SGIC elution profiles for the J100 sample set.	95
Figure 7.11: Normal-phase HT-SGIC elution profiles of the J75 sample set. 1-Hexanol flow rate profile = red dashed line.	96
Figure 7.12: Normal-phase HT-SGIC elution profiles of the J100 sample set. 1-Hexanol flow rate profile = red dashed line.	96
Figure 7.13: SEM-EDS images of PVC/wax binary blends for a) oJ75_10; b) oJ75_40; c) oJ100_10 and d) oJ100_40. Electron image = grey; Carbon = red; Oxygen = green. Scale bar = 2 mm.	98
Figure 7.14: SEM-EDS images of PVC/wax/CaSt ternary blends for a and c) oJ75_10; b and d) oJ75_40. Electron image = grey; Chloride = blue; Carbon = red. Calcium = purple; Oxygen = green. Scale bar = 2 mm.	99
Figure 7.15: SEM-EDS images of PVC/wax/CaSt ternary blends a and c) oJ100_10; b and d) oJ100_40. Electron image = grey; Chloride = blue; Carbon = red. Calcium = purple. Scale bar = 2mm.	100
Figure 7.16: SEM-EDS images of binary blends a) oJ75_10; b) oJ75_40; c) oJ100_10 and d) oJ100_40 and ternary blends e) oJ75_10; f) oJ75_40; g) oJ100_10 and h) oJ100_40 after screw freezing. Electron image = grey; Chloride = blue; Carbon = red. Calcium = purple. Scalebar = 5 mm.	101
Figure 7.17: General interpretation of a PVC fusion curve.	103
Figure 7.18: Fusion curves of the ternary blends of the J75 series at a) 185 °C and b) 190 °C and the J100 series at c) 185 °C and d) 190 °C.....	106
Figure 7.19: Fusion curves of the binary blends of the J75 series at a) 185 °C and b) 190 °C and the J100 series at c) 185 °C and d) 190 °C.....	107
Figure 7.20: T1 rho SS-NMR proton relaxation curves of the unfused blends a) J75 series and c) J100 series and the melt-pressed blends of the b) J75 series and d) J100 series.	109

List of Tables

Table 2.1: Novel industrial FT waxes.	13
Table 2.2: Waxes from other commercial suppliers.	13
Table 2.3: Blending ratios for proof-of-concept experiments.	16
Table 3.1: HT-SEC results of Wax set 1.	19
Table 3.2: Characteristic absorption bands observed in FTIR spectra of waxes.	20
Table 3.3: D-spacing and crystal size from respective XRD peak signals.	28
Table 3.4: DSC results showing melting endotherm maxima, enthalpy, and percentage crystallinity.	30
Table 3.5: Blend compositions of wax with PVC and CaSt in phr.	36
Table 5.1: PVC formulations used for stage II and III.	50
Table 5.2: HT-SEC results for both polar and nonpolar waxes.	54
Table 6.1: Classification of waxes used.	68
Table 7.1: Oxidised waxes from ozonolysis procedure.	79
Table 7.2: ^{13}C NMR chemical shifts and integrals of all waxes in the hydrocarbon region.	86
Table 7.3: ^{13}C NMR chemical shifts and integrals of all waxes in the carbonyl and alkene regions.	86
Table 7.4: DSC melting results of all wax samples.	88
Table 7.5: DSC crystallization results of all wax samples.	88
Table 7.6: HT-SEC results of all wax samples.	93
Table 7.7: Formulation composition of binary and ternary PVC blends.	102

List of abbreviations

ATR FTIR	attenuated total reflectance – Fourier transform infrared
¹³ C-NMR	carbon thirteen nuclear magnetic resonance
CaSt	calcium stearate
CP-MAS	cross-polarized magic-angle spinning
DSC	differential scanning calorimetry
ESL	ethylene sequence length
ELSD	evaporative light scattering detector
FT	Fischer-Tropsch
FTS	Fischer-Tropsch Synthesis
FRP	fully refined paraffin
HTFT	high temperature Fischer-Tropsch
HT-SEC	high temperature - size exclusion chromatography
HT-SGIC	high temperature - solvent gradient interaction chromatography
LTFT	low temperature Fischer-Tropsch
PAO	poly alpha olefin
PVA	polyvinyl alcohol
PVC	polyvinyl chloride
RWGS	reverse water gas shift
SEM-EDS	scanning electron microscopy – energy dispersive x-ray spectroscopy
SSE	single screw extrusion
TSE	twin screw extrusion
uPVC	unplasticized polyvinyl chloride
VCM	vinyl chloride monomer
XRD	x-ray diffraction

Introduction

Due to the high commercial importance of PVC, it is essential to have a deep understanding of the extrusion process of uPVC. This process consists of three main parts namely the instrumentation, the PVC grade and, the lubrication mechanism with the latter being equally important to a well-functioning system as the former. The lubrication mechanism has been the subject of much speculation and no proposed mechanisms, to our knowledge, have been conclusively proven to be correct. Lubricants are a large group of materials which vary widely in chemical nature and therefore applications. In uPVC production waxes are the most important component in a lubrication system. Within a lubrication system a wide variety of waxes, which can be combined in various ratios, exists. Waxes can be implemented in countless ways to achieve the same result which is to impart sufficient lubrication to ensure that no PVC degradation occurs, and complete PVC fusion is achieved. It is therefore necessary to understand what the determining factors or properties of a wax are that need to be taken into consideration when a PVC formulation is being developed. In this research project, it was therefore necessary to fully characterize lubricants according to their varying properties. Once the waxes were comprehensively analysed it was necessary to track their positions and therefore performance during processing of a PVC formulation. Through combination of the knowledge gained from the wax characterization and the tracking thereof through processing an attempt was made to either improve on currently accepted lubrication mechanism models or to create a new one.

Chapter 1: Background

1.1 Industrial importance

Polyvinyl chloride (PVC) is the second most produced polymer in the world behind polyolefins¹⁻⁵. Due to its many desirable properties such as chemical resistance, non-flammability, ease of modification and low cost of production, PVC is a highly versatile polymer⁶⁻⁸. PVC is widely used in the building industry where the primary applications include water piping and frames for doors and windows^{5,6,9}. Other main consumers of PVC include the packaging and cosmetic industries^{3,6,7}. Unplasticized PVC (uPVC) together with plasticised and chlorinated PVC each contribute a third of the PVC used for piping⁷. Some drawbacks to PVC include its low processability, low thermal stability and brittleness⁶⁻⁸.

1.2 PVC polymerization

PVC is mostly polymerized using a free radical polymerization technique called suspension polymerization. Water insoluble vinyl chloride monomer (VCM) together with an organic peroxide initiator is suspended in a water medium using a suspending agent such as polyvinyl alcohol (PVA). A buffer solution is also used to mitigate the effects of free HCl gas within the system. Within an autoclave at high pressure, mechanical agitation of the mixture is applied. Once the initiating temperature is reached the polymerization begins. Water insoluble PVC polymer precipitates out of the mixture and can then be separated¹⁰⁻¹⁴. Each of the above-mentioned variables play a significant role in the properties of the resulting polymer. The most important property being the so-called K-Value of PVC. A PVC grade with a specific molecular weight exhibits a certain viscosity. These viscosities are related to different K-values. K-values of around ± 67 are used for rigid pipe extrusion and consists of high molecular weight polymer with good mechanical properties. A low K-value of about 55 - 62 would be a lower melt viscosity polymer used generally for injection or blow moulding purposes^{2,9,15,16}.

Emulsion polymerisation is only accountable for about 10% of PVC in use today. This process differs from suspension polymerization by making use of a water-soluble surfactant such as secondary alkyl sulfonates. The stability of the emulsion is ensured by adding more emulsifying agent as the particles grow. Polymerization is stopped by venting off the unreacted VCM. Emulsion grade PVC is usually a much finer grain which is required for certain applications⁹.

Bulk polymerisation can also be used but it is not as popular as suspension or emulsion grade PVC as it results in high heat build-up and viscosities in the absence of water^{9,17}.

1.3 PVC Processing

After the polymerisation of PVC, it must be processed. Processing of PVC is primarily achieved through the extrusion. Extrusion converts individual PVC particles into a PVC melt which can be shaped into any desired product. The main objective of an extruder is to cause the PVC matrix to fuse by applying efficient friction, heat, and pressure the formulation. Initially it was thought that during this process secondary PVC particles (50 - 200 μm) are broken down into smaller primary (0.2 – 1.5 μm) particles. Burgess et al.¹⁷ however, showed that the PVC particles rather undergo compacting, elongation, and densification with little to no breakdown of the particles. Efficient fusion is achieved once the PVC particle surface boundaries disappear and a continuous three dimensional PVC matrix is observed¹⁸. Efficient fusion is a very important parameter in PVC processing and is directly related to the final properties of a PVC product¹⁹. Due to its importance, PVC fusion has been thoroughly studied^{9,20–23}.

PVC extrusion is usually done by twin screw extrusion (TSE) as this method has a high throughput and cost efficiency²⁴. Single screw extrusion (SSE) is used in the piping industry as it only requires a low weight/hour throughput²⁵. TSE consists of two counter rotating screws resulting in a high amount of mixing and shear in a brief time. SSE consists of two parallel plates exerting a net shear on the polymer bed. The inner barrel wall and the screw root, function as the static and the mobile plates, respectively. SSE has the added bonus of having a less complex flow than a TSE making easier for studying the flow behaviour of different additives^{25–27}.

An example of an SSE is shown in Figure 1.1. An SSE consists of three zones. Zone 1 is the feeding zone, where the dry polymer formulation is introduced. The second zone is where pressure and friction increase which results in fusion. In zone three, or the metering zone, fused polymer is transferred to the die.

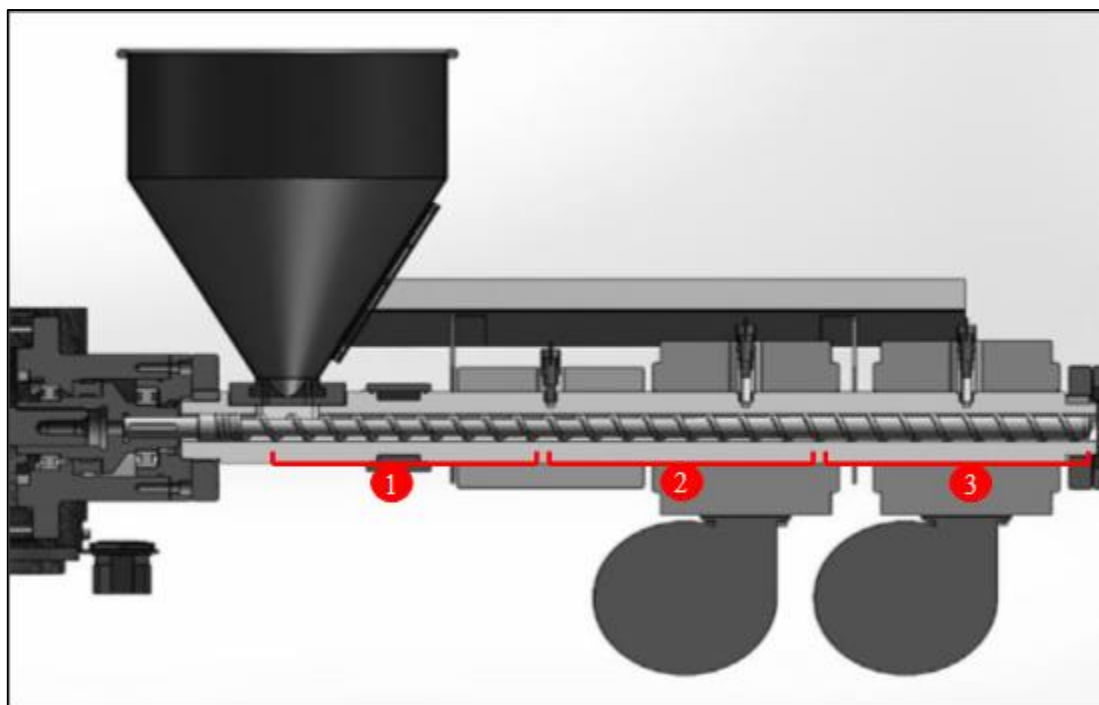


Figure 1.1: Schematic view of a single screw extruder¹⁸ showing the; 1) feeding zone, 2) compression zone and, 3) metering zone.

1.4 PVC Additives

Due to the low heat stability and high melt viscosity of neat PVC, it is dry mixed with various additives before extrusion. These additives perform highly specific functions to aid in processing thereof²⁸. Additives such as heat stabilizers are essential for preventing any degradation of the PVC polymer. This is done by either reacting with liberated hydrogen chloride, eliminating double bonds, interfering with chain propagation or acting as antioxidants^{29,30}. Processing aids are used to improve the melt elasticity as rigid PVC is readily ruptured during melt extrusion^{20,31,32}. Examples of processing aids are copolymers based on methyl or ethyl methacrylate which are highly compatible with PVC⁴. Some performance additives such as impact modifiers, UV stabilizers, colorants, and fillers can also be added during the mixing stage as desired^{6,17}.

uPVC differs from plasticised PVC in that its production omits the use of a plasticizer. Plasticizer lowers the glass transition temperature of the polymer making it more flexible⁹. General purpose plasticizers such as esters from phthalic acid are usually used⁶.

The most important processing additives are the lubricants which reduce friction at different areas of high shear within an extruder. Traditionally lubricants are defined as being either

internal or external. This definition depends on the lubricants' affinity to associate internally with the PVC matrix or externally at the PVC matrix-metal interface.

To evaluate the performance of additives for PVC extrusion various experiments have been conducted. The most important of these experiments was to measure the effect of additives on PVC fusion. Some of these experiments were done by measuring the degree of fusion using differential scanning calorimetry^{20,30}. Torque rheometry is the most popular way to measure PVC fusion. It measures fusion torque, time and temperature, in addition it can also evaluate the stable time of a PVC formulation^{16,20,31}. Mechanical properties relating to fusion have been determined using tensile testing, where tensile strength is related to level of fusion¹. Visual evaluation of the fusion process has also been done by analysing the extrudate using scanning electron microscopy¹⁶. Another interesting method of tracking the fusion process was done using a technique called screw freezing. In this technique the fusion process can be tracked along the extruder screw¹⁷.

1.5 Lubrication

According to Rabinovitch et al.³¹ the use of lubricants is one of the three most important parameters in uPVC processing, despite its very low concentrations within the PVC formulations. The other two parameters are the PVC resin and the processing equipment. Precisely how lubricants perform their function within these formulations has been the subject of much speculation and still has not been proven definitively.

External lubricants are usually classified as having no chemical association with the polymer matrix. They are active at the polymer-metal surface where they promote metal release and therefore delay fusion³³. Internal lubricants are classified as having chemical association with both the polymer matrix as well as the external lubricant. They are said to reduce melt viscosity and act as a fusion promoter¹⁶. All waxes do not follow this trend and some exhibit both internal and external characteristics which is why simply classifying waxes according to these properties are insufficient. Since the mechanism of how the wax interacts with its surroundings seems to be the basis of its classification, elucidating this mechanism is necessary.

1.6 Previous studies on the mechanism of lubrication

Various research groups have attempted to elucidate the role of lubricants during single screw extrusion of uPVC by examining the macroscopic properties of uPVC formulations^{22,24,31,33–35}. Some of these properties included metal-release, effect on melt viscosity, rheological properties, percentage haze, solubility and, changes in glass transition temperature of the PVC. These properties could however not identify the mechanism of lubrication as different authors found varying results when analysing the same waxes. Authors such as Lindner³⁶ and Fredricksen³⁷ concluded contradicting properties for CaSt. Lindner found that CaSt shows mild external properties and also acts as a fusion promotor. Internal lubricants are supposed to decrease melt viscosity, but Fredricksen found that the opposite was true for CaSt. Hartitz et al.³⁸ found that by investigating the fusion properties of a PVC formulation, waxes could be classified according to their fusion time. Hartitz also investigated the combination of waxes in a formulation and found that there exists a synergistic effect between polar and nonpolar waxes. This was a big step for unravelling the lubricant mechanism as it took into account the overall effect of the role of the lubricants. The mechanism however could not yet be explained.

Using transmission electron microscopy (TEM) and scanning electron microscopy (SEM), Rabinovitch et al.³¹ could visually interpret how lubricants interact with the PVC matrix. Thereafter the group proposed a lubrication mechanism wherein internal and external lubricants should rather be classified as surfactants and slip agents. A schematic of this mechanism is shown in Figure 1.2³¹. In this mechanism they have proposed that polar CaSt headgroups associate with the polar PVC and polar slightly oxidized metal surface therefore acting as surfactants. The only other nonpolar region left in the system for nonpolar waxes to associate with is the nonpolar surfactant tails. These association consist of weaker van der Waal's forces and is therefore the region where slippage occurs.

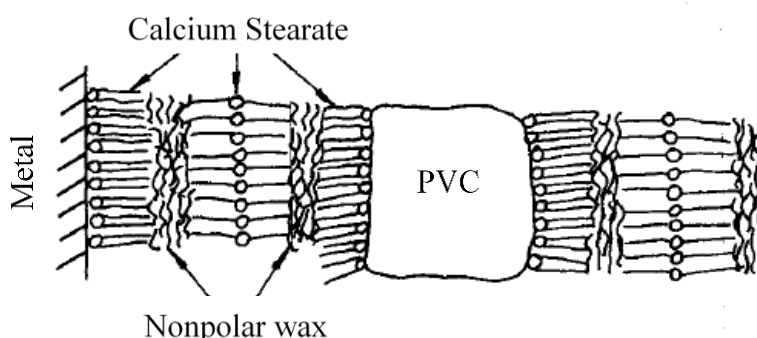


Figure 1.2: Schematic of surfactants and slip agents proposed by Rabinovitch et al.³¹

Summers et al.¹⁶ confirmed the aforementioned mechanism by showing that lubricant failure is due to lubricant inversion from the continuous phase to a discontinuous phase with increasing melt temperatures. This was done using SEM coupled to energy dispersive x-ray spectrometry (SEM-EDS) where the calcium (Ca) element of the calcium stearate could visually be detected after fracturing of fused specimens. In the study conducted by Summers and co-workers, they used the assumption that non-polar waxes were only present in the other nonpolar areas in this system, namely the nonpolar stearate tails. To our knowledge no tangible evidence of these presumptions have been found. This mechanism also does not explain the mechanism of how functional waxes interact within a formulation.

Functional waxes with characteristics of both internal and external lubricants have been the focus of more recent studies due to their effect on minimizing plate-out^{4,5,9,15,39}. Plate-out occurs when additives such as stabilizers migrate out of the PVC matrix with an external lubricant. It was therefore necessary to produce an external lubricant with a slightly higher polarity which would minimize migration³⁹. Examples of such lubricants include amide and ester based waxes¹. It was however found that functional waxes, in addition to minimizing plate-out, exhibit advantageous properties of both internal and external lubricants. Beneficial internal lubrication properties such as shorter fusion times, lower operating pressures and torques are gained as well as comparable gloss finishes to those achieved using external waxes³⁹. These functional waxes also have the bonus of being used in much lower concentrations than when using a conventional internal/external wax combination. Until now, however, all formulations with functional waxes are still stabilized with some sort of Zn/Ca stearate internal lubrication⁴⁰.

The current study was pursued to further investigate the various mechanisms of lubricant interactions with the PVC matrix proposed in previous literature. SEM-EDS was the integral method used to track the individual components within a uPVC formulation during processing. This work gave some insight into the interactions of the individual lubricants with each other as well as the associations with the PVC matrix.

1.7 Types of waxes and their production

Various waxes used in uPVC production can be naturally sourced from the petroleum industry or synthetically manufactured. This study focussed on the most popular waxes used in the

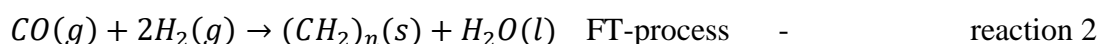
industry today. These include paraffin, alpha olefin, microcrystalline, polyethylene, Fischer-Tropsch and oxidized waxes.

1.7.1 Petroleum derived waxes

Paraffin and microcrystalline waxes are by-products of the petroleum industry. These long chain hydrocarbons vary widely in chain branching, thermal behaviour, molecular weight, and molecular weight distribution. Microcrystalline wax contains more naphthene and branched material than fully refined paraffins which consist mostly of n-alkanes. The presence of these bulky materials in the microcrystalline wax inhibits crystallization which normally results in a less crystalline material than the paraffin wax^{41,42}.

1.7.2 Fisher-Tropsch wax

Due to global warming and the constant pressure to reduce our carbon footprint many companies are using CO₂ conversion into higher hydrocarbons as an alternative. The Fischer-Tropsch synthesis (FTS) process uses a metal catalyst and hydrogen to achieve this conversion. This process can be operated in two temperature modes. The high temperature Fischer-Tropsch (HTFT) mode is used with an iron catalyst and operates at temperatures around 290-360 °C. The low temperature Fischer-Tropsch (LTFT) mode is run with a supported cobalt catalyst at temperatures around 180-260 °C using a fluidised bed reactor⁴³. LTFT is also the process used for generating hydrocarbon waxes. This process also has the added benefit of being selective for generating waxes with a high degree of linearity. A reverse water gas shift reaction (RWGS) is done to convert CO₂ to CO (reaction 1). In the second step (reaction 2) the FT process is followed to produce hydrocarbon chains⁴⁴. A classical step-growth polymerization is followed which contains chain initiation, propagation, and termination steps. Chain initiation occurs when the initial chain monomer is absorbed onto an active site on the catalyst which produces a radical. Chain propagation is followed by nearby monomers attaching to the growing chain. Chain termination occurs when the radical is eliminated, and a chain desorbs from the active site⁴⁵.



Alpha olefin waxes are mainly produced through the oligomerisation of ethylene, thermal cracking of petroleum products or formed during the FTS process⁴⁶. An advantage of synthetically manufacturing these waxes is that a specific carbon number relating to specific properties can be targeted⁴⁷.

1.7.3 Functionalized waxes

Lubricants consisting of polar moieties are traditionally classified as internal lubricants. The degree of polarity/nonpolarity can however be altered, rendering a slightly more polar/nonpolar lubricant. This results in a lubricant with slightly more or less internal/external nature³⁹.

Examples of such functionalized waxes are fatty alcohols and fatty acids. These molecules consist of a nonpolar aliphatic chain which contains polar hydroxyl or carbonyl groups. Combining these functionalities in various ways result in molecules with a wide range of overall polarity. An example of this is distearyl phthalate which is produced from phthalic acid and stearyl alcohol. Distearyl phthalate lowers torque and improves melt flow which are internal and external wax properties, respectively^{4,39}. Other examples include esters from fatty acids and polyols such as stearyl stearate and ethylene glycol distearate. Higher fatty acids such as montanic acid are also very useful as functional waxes but are more expensive as they are either synthesized or extracted from the earth^{6,39}. Fatty acid amides or amide wax such as ethylene bis-stearamide also serves as a functional wax. Metallic soaps are used for their excellent lubricating properties. These components are mostly made using alkaline earth metal such as calcium or magnesium. Calcium stearate is mostly used as internal lubricant in PVC formulations^{4,6,9}.

Oxidized wax can be synthesized by passing an oxygen containing gas through these hydrocarbon waxes at temperatures above the wax's melting point. Using a catalyst such as sodium permanganate accelerates the process⁴⁸. The rate of oxidation is dependent on the temperature of the reaction as well as the amount and type of oxygen containing gas⁴⁹. Using ozone as the oxygenating gas, the degree of oxidation can be precisely controlled, as well as formation of side products can be minimized^{50,51}.

Chapter 2: Method development

The research conducted followed an approach of consequential method development. The thesis is thus set out in a similar fashion, tracking the progress of the research with time. Due to the continual adjustment and addition of new experimental techniques throughout the study, the relevant experimental parameters, techniques and instrumentation are discussed within their respective chapters.

2.1 Outline for method development

Tracking lubricant migration during PVC processing is of some importance when new products are being evaluated against industry standards. In this study a newly developed set of Fischer Tropsch (FT) waxes were analysed to evaluate their performance as external lubricants for PVC. During this assessment, these waxes were compared against a set of commercially available waxes. In such cases it is essential to fully understand the mechanism of lubricant migration within an unplasticized polyvinyl chloride (uPVC) formulation during extrusion. A method for tracking lubricants within a uPVC system during extrusion has, to our knowledge, not been reported in literature. It was therefore one of our aims to develop such a method.

Lubricants are generally classified according to the site at which they associate within a certain formulation during the extrusion process³¹. This site is also where a lubricant performs its function. A lubricant's function is to reduce friction at places of high shear, such as metal-polymer interfaces between the extruder and extrudate³³. Exactly at which sites and how these lubricants migrate towards these sites was the main aim for the development of this method.

To track the migration of the lubricants it was necessary to establish a physical starting, middle and end site of each component within a given polymer formulation. It was decided to assign these sites to the three stages on an extruder namely the feeding zone (stage 1), compression zone (stage 2) and the metering zone (stage 3). It needs to be pointed out that stages 1 and 2 interactions were studied outside of the extruder, but that it was expected for these compounds to be representative of what would be found in the extruder.

Stage 1 was described as a component's site 1, where all the different components were still physically distinguishable from each other. At stage 1 the components have only been high speed mixed. This process only imparts low amounts of shear and heat, which are not sufficient to induce chemical interactions between the individual components. At site one therefore, each of the components can be classified as randomly scattered. At this point all the components

still exist in a chemically or physically unmodified form. It was therefore decided to fully characterize the individual components according to their physical, chemical, and thermal nature. This step could serve as platform for any conclusions drawn in the subsequent stages.

To investigate the effect of molecular size on a given additive's migration pattern, high temperature size exclusion chromatography (HT-SEC) was used to probe the molecular weight of the lubricants. ATR-FTIR was done to examine the chemical nature of the waxes by identifying functional groups. This was done to investigate any chemical interactions that the wax might have towards any other component such as PVC, calcium stearate (CaSt) or at the oxidised metal interface. Chain linearity and branching was probed using ^{13}C nuclear magnetic resonance (^{13}C -NMR) spectroscopy. Using ^{13}C cross polarized magic angle spinning (CP-MAS) and ^1H Wideline NMR experiments the rigidity of the waxes were examined. Oxygenate functionalities could also be investigated using this technique. Melting behaviour of the waxes was studied by differential scanning calorimetry (DSC). DSC was also used to investigate some association interactions between the components, by following shifts in the glass transition temperatures.

Stage 2 was also done outside of the extruder as sampling from within the extruder could not be achieved. Stage 2 or the compression zone in the extruder is the region where heat and friction start to increase slightly. At this point all the components except for PVC starts to melt and become mobile. Both chemical and physical interactions could occur at this stage. Stage 2 was simulated by using a process called hot-melt mixing. All the components were mixed at a high rpm and elevated temperature ($165\text{ }^{\circ}\text{C}$) in a beaker. This temperature was chosen as it was above the melting points of the wax ($\leq 120\text{ }^{\circ}\text{C}$) and the CaSt ($\pm 155\text{ }^{\circ}\text{C}$). After blending, the samples were taken for scanning electron microscopy coupled with energy dispersive x-ray spectroscopy (SEM-EDS) analysis to gain insight into the migration of the mobile components and to physically determine the sites (site 2) of all the individual components. These results could provide clarity on the second site of tracking before reaching the PVC fusion stage. Once fusion occurred the PVC matrix formed a solid polymer bed and effectively “froze” all the components in place which stopped them from migrating any further. Once frozen, the components were at site two.

Stage 3 was chosen as the third and final site of all the components. Due to challenges sampling from the extruder during this stage, sampling took place at the die where the fused sample exited the extruder. Extrudates had a rod like shape which was cross sectioned by microtoming

and subsequently sent for resin embedding and polishing. After polishing, samples were gold coated and analysed by SEM-EDS.

The customized technique allowed for the individual components to be tracked throughout the mixing and fusion stages. Clear differences were seen in the migration behaviour of the different components. The effect of CaSt addition and external lubricant polarity was investigated. Clear differences in behaviour were observed indicating that the technique was effective at tracking the migration as well as revealing some interesting association interactions between the various blend components.

2.2 Stage 1 (Wax set 1)

The aim was to investigate any physical or chemical interactions that might occur between different waxes and PVC. Attributes of waxes that could influence the interactions include chain length, chain branching, chemical composition, and molecular weight distribution. Another important consideration was to investigate the interactions between waxes and other formulation ingredients such as the CaSt.

In the first stage of this project, it was essential to characterize a set of waxes according to their chemical and physical nature. This provided a deeper understanding into the various mechanisms that are at play in this extremely complicated system. A fundamental knowledge of the chemical and physical properties for the range of waxes was obtained through various analytical techniques. These techniques included: HT-SEC; FTIR; ^{13}C -NMR; XRD and DSC.

Table 2.1 represents a range of newly developed FT. This sample set was chosen specifically to compare these new FT waxes (Category 1) to other commercial counterpart waxes (Category 2) for use as external lubricants. Waxes from category 2 were derived from various technologies resulting in waxes with different chemical, physical and morphological characteristics.

Table 2.1: Novel industrial FT waxes.

Category 1		
Manufacturer	Grade	Code
Juniper	FT	W52
	FT	J100
	FT	J75

Table 2.2: Waxes from other commercial suppliers.

Category 2		
Manufacturer	Grade	Code
Commercial supplier	Paraffin	FRP 58/60
Marcus oil Company	PE	Marcus 300
Chevron Phillips	Alpha olefin	PAO
Sonneborn	Microcrystalline wax	Microwax
Sarpri	Oxidised wax	Ceranol 28L56
Sarpri	Oxidised wax	Ceranol 40L90

2.3 Experimental: Stage 1

Neat materials were characterized according to their molecular size, chemical composition, chain linearity and branching, and thermal behaviour using the following techniques. Samples were characterized as is, with no prior modification.

2.3.1 High temperature – size exclusion chromatography (HT-SEC)

Determination of the molecular weights and molecular weight dispersity was carried out on a PL220 high temperature chromatography instrument (Polymer laboratories, Varian, Church Stretton, Shropshire, England) coupled to a differential refractive index (RI) detector. Polyethylene standards were used for calibration. Samples (4 mg) were dissolved in 1, 2, 4 – trichlorobenzene (TCB) with 0.025% butyl-hydroxy-toluene (BHT) stabilizer. The mobile phase had a flow rate of 1 mL/min. The stationary phase consisted of three 300 × 7.5 mm² PLgel Olexis columns (Agilent Technologies, UK) together with a 50 × 7.5 mm² PLgel Olexis guard column. Sample volumes of 200 µL were analysed at 150 °C.

2.3.2 Attenuated total reflectance – Fourier transform infrared spectroscopy (ATR-FTIR)

Analyses were conducted on a Thermo Scientific Nicolet iS10 FTIR spectrometer with a diamond crystal. Scans were performed at a resolution of 4 cm⁻¹ and 64 scans were taken. OMNIC (version 9) processing software was used for data analysis.

2.3.3 ¹³C Nuclear magnetic resonance (¹³C-NMR)

¹³C-Nuclear magnetic resonance (¹³C-NMR) spectra were acquired on a Varian^{Unity} INOVA 600 MHz liquid state NMR Spectrometer at 120 °C. All samples (70 – 75 mg) were dissolved in 0.6 mL deuterated tetrachloroethane (d-TCE). A 90° pulse angle with acquisition time of 0.87 s and relaxation delay of 15 s was used. The average number of scans was 4000. ¹³C chemical shifts were referenced to the backbone CH₂ peak at 30 ppm and analysed on MNova software. Detailed structural information on the waxes could be deduced from this technique.

2.3.4 Solid-state NMR (SS-NMR)

Solid-state NMR spectra were acquired using a Varian VNMRS 500 MHz two-channel spectrometer using 6 mm zirconia rotors and a 6 mm ChemagneticsTM T3 HX MAS probe. The ¹³C cross-polarization (CP-MAS) spectra were recorded at 25 °C with proton decoupling, a 3.5 μs 90° pulse and a recycle delay of 5s. Magic-angle-spinning (MAS) was done at 5 kHz and adamantane was used as an external chemical shift standard where the downfield peak was referenced to 38.3 ppm. The power parameters were optimised for the Hartmann-Hahn match. The contact time for cross-polarization was 1 ms. Proton (¹H) wideline experiments were done using the same probe in static mode. All samples were analysed in an equivalent manner for comparison purposes.

2.3.4 Differential scanning calorimetry (DSC)

Endothermic melting and exothermic crystallization behaviour of the samples were analysed by using a TA instruments Q100 differential scanning calorimeter, calibrated with indium metal according to standard procedures. A three-step cycle was implemented wherein each sample (4 mg) was heated from room temperature to 200 °C in the first cycle at a heating rate of 10 °C·min⁻¹, this was done to remove any thermal history of the samples. Samples were kept

isothermally at 200 °C for 3 minutes, after which they were cooled to 25 °C at 10 °C·min⁻¹. During the ultimate step, the temperature was kept isothermally at 25 °C for 3 minutes and then heated to 200 °C. Only data obtained from the second heating cycle was processed for all the thermal analysis calculations. The DSC measurements were conducted in an inert nitrogen atmosphere at a purge gas flow rate of 20 ml·min⁻¹. Data was analysed using TA universal analysis software.

2.3.5 X-ray Diffraction (XRD)

X-ray diffraction data was collected using a Bruker D2 PHASER diffractometer equipped with a Lynxeye 1D detector and Ni-filtered Cu K α radiation ($\lambda = 1.5418 \text{ \AA}$; 30 kV, 10 mA generator parameters; restricted by a 1.0 mm divergence slit and a 2.5 Soller collimator). Samples were loaded onto a zero-background holder and patterns were recorded in the 2θ range from 5°–35° with a step size of 0.02° and step time of 1s. Wax samples were melted on a Teflon sheet and placed on a hot-plate. Thereafter, the samples were removed from the hot-plate and allowed to cool down to room temperature. The solid crystallized samples were then analysed as is. All experiments were done at ambient conditions. The data was analysed using OriginPro v. 8.5 software. All crystalline peaks were de-convoluted, separated from the amorphous halo and integrated.

2.4 Experimental: Stage 2

After the individual components were characterized the next step was to gauge whether there are any association interactions between the components through addition of heat and agitation. Binary and ternary mixtures were hot-melt blended by overhead stirring with a Heidolph RZR series mixer (2100 rpm) at 165 °C for 15 minutes. This temperature was chosen to ensure all the lubricants were above their melting temperatures. Blend ratios are listed in Table 2.3. Thereafter the samples were microscopically inspected using a scanning electron microscope. The dry powders were fixed onto aluminium stubs and taken for SEM-EDS analysis. Initially, as a proof of concept, only some of the components were investigated (Table 2.3). The PVC was sourced from Shintech (SE-950) and calcium stearate from Chemson.

Table 2.3: Blending ratios for proof-of-concept experiments.

Sample	Amounts (phr)			
	PVC	CaSt*	J75	Ceranol 40L90
a	100	-	-	-
b	100	10 and 5*	-	-
c	100	-	10	-
d	100	10 and 5*	10	-
e	100	-	-	10

2.4.1 Scanning electron microscopy Energy dispersive x-ray spectrometry (SEM-EDS)

The samples were analysed using a Zeiss EVO scanning electron microscope. Prior to imaging, the samples were mounted on aluminium stubs with double sided carbon tape. The samples were coated with a thin (~10 nm) layer of gold, using an Edwards S150A gold sputter coater. A Zeiss 5-diode back scattered electron (BSE) detector (Zeiss NTS BSD) and Zeiss Smart SEM software were used to generate BSE images. The samples were chemically quantified by semiquantitative energy dispersive x-ray spectrometry (EDS) using an Oxford Instruments® X-Max 20 mm² detector and Oxford Aztec software. Beam conditions during the quantitative analysis and backscattered electron image analysis on the Zeiss EVO were 20 kV accelerating voltage, 8 nA probe current, with a working distance of 8.5 mm and a beam current of 5 nA. The counting time was 10 seconds live-time.

2.5 Experimental: Stage 3

For stage 3 the amount of calcium stearate was reduced to 5 phr to avoid gas build-up inside the extruder. Blending ratios are listed in Table 2.3 and denoted by an asterisk(*). Samples were high speed mixed with an overhead stirrer for 15 minutes at 25 °C, thereafter mixtures were extruded. Extrusion was done on a Brabender Plasticorder PLE 651 extruder with the single screw barrel attachment (L/D = 26.5:1). The barrel was preheated on three of the four sections. Section one, the feed section, was heated to 145 °C. The compression section was heated to 155 °C and the metering section was heated to 190 °C. The die area which can also be heated was removed and replaced with a short die (L/D = 5/1).

Removing this section (thus also removing the breaker plate which causes turbulent flow) caused molten polymer to maintain its directional flow. At this stage, the PVC has fused, and no further lubricant migration should occur. Sampling at this interval allowed for a direct interpretation of how the molten polymer matrix and the additives were interacting during directional flow. This technique is further explained in the following sections.

Approximately 9 mm diameter cross sections of the extruded material were then embedded in epoxy resin and cured in an oven at 40 °C for 24 hours. Thereafter the embedded samples were polished with 9 µm (10 min), 3 µm (15 min) and 1 µm (15 min) grit polishing discs on a rotational polisher until a uniformly polished area could be observed through a light microscope. The samples were taken for SEM-EDS analysis as is.

Chapter 3: Method development: Results and discussion

3.1 Stage 1 (Wax set 1)

3.1.1 High temperature size exclusion chromatography (HT-SEC)

First, the waxes were categorized according to their hydrodynamic volume (H_v). Hydrodynamic volume relates to the space a molecule occupies when in solution and therefore their relative molecular weight⁵². As can be seen in Table 3.1, large differences in both the molecular weight and molecular weight distributions were observed. Molecular weight ranged from Ceranox 40L90 being the lowest with a M_n of 267 g/mol to J100 having the highest M_n of 618 g/mol. The molecular weight distribution or dispersity (\bar{D}) is calculated by dividing weight average molecular weight (M_w) by the number average molecular weight (M_n). \bar{D} is therefore an indication of how uniform the molecular weight distribution is. J75 and FRP exhibited the most uniform molecular weight distributions whereas the oxidised waxes exhibited the broadest distributions. As will be discussed in the DSC section, the group with \bar{D} values of 1.1 - 1.2 also lies in the lower melting range and the waxes having \bar{D} values of 1.3 - 1.7 melted at higher temperatures. A visual representation of the SEC chromatograms can be seen in Figure 3.1.

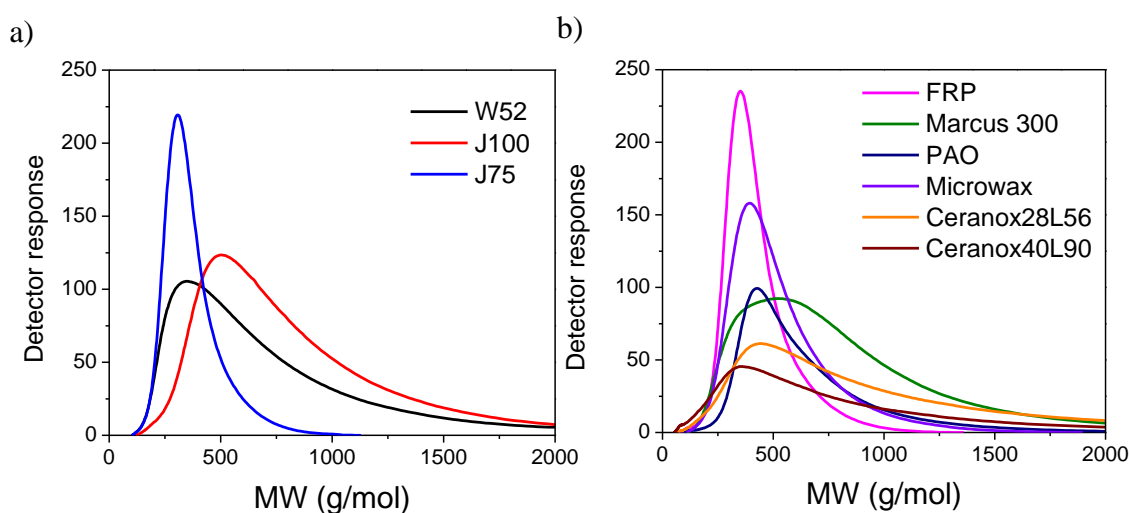


Figure 3.1: HT-SEC chromatograms of waxes in a) category 1 and b) category 2.

Table 3.1: HT-SEC results of Wax set 1.

Wax	M_p^1 (g/mol)	M_n^2 (g/mol)	M_w^3 (g/mol)	\bar{D}^4
W52	351	358	475	1.3
J100	505	489	618	1.3
J75	307	298	326	1.1
FRP	351	337	375	1.1
Marcus300	522	420	560	1.3
PAO	429	430	508	1.2
Microwax	394	377	434	1.2
Ceranol 28L56	443	382	587	1.5
Ceranol 40L90	354	267	442	1.7

3.1.2 Attenuated total reflection Fourier transform infrared spectroscopy (ATR-FTIR)

Chemical characterization of the waxes was done by attenuated total reflection Fourier transform infrared spectroscopy (ATR-FTIR). ATR-FTIR is one of the most versatile and effective means of characterizing molecules according to their chemical composition. ATR-FTIR was used to establish the dominating or varying functional groups. All the major absorption bands relating to a classical spectrum of polyethylene wax was accounted for. Subtle differences could be observed highlighting some of the observable variances in the molecular arrangement of the polymeric chains. Table 3.2 lists some of the characteristic absorption bands observed in spectra of waxes^{53–56}.

¹ Peak molecular weight

² Number average molecular weight

³ Weight average molecular weight

⁴ Polydispersity

Table 3.2: Characteristic absorption bands observed in FTIR spectra of waxes.

Wavenumber (cm ⁻¹)	Type of deformation (Intensity ⁵)
3450	O-H Stretch (m)
2959	asymmetric stretching CH ₃ (w)
2920	asymmetric stretching CH ₂ (vs)
2846	symmetric stretching CH ₂ (s)
1776	Symmetrical C=O stretch of Lactones (m)
1734	symmetrical C=O stretch of Ester group (s)
1716	symmetrical C=O stretch of Carboxylic acid (s)
1640	C=C stretching (w)
1474	CH ₂ bending (s)
1460	CH ₂ bending (s)
1411	R1R2 C=O long chain saturated Ketones (w)
1377	CH ₃ symmetric bending (w)
1366 and 1351	Wagging deformation (m)
1306	Twisting deformation(w)
1176	Wagging deformation (vw)
990	Bending RCH=CH ₂
910	Bending RCH=CH ₂
890	CH ₃ rocking (vw)
730	CH ₂ rocking (m)
720	CH ₂ rocking (s)

First, we examined the methylene and methyl stretching region (2700-3000cm⁻¹). From Figure 3.2 there were no significant differences in the CH₂ asymmetric-stretching (2920 cm⁻¹) and the symmetric-stretching (2846 cm⁻¹) bands of the various waxes. However, subtle differences were visible at the CH₃ stretching (2959 cm⁻¹) with a greater intensity observed for J75, FRP. These three waxes also exhibited a small band around 2870 cm⁻¹, relating to a symmetric CH₃ stretching vibration. These absorption bands might indicate greater end group concentration due to lower molecular weights or the presence of branches along the wax backbone.

⁵ Intensity scale: very weak (vw), weak (w), medium (m), strong (s), very strong (vs).

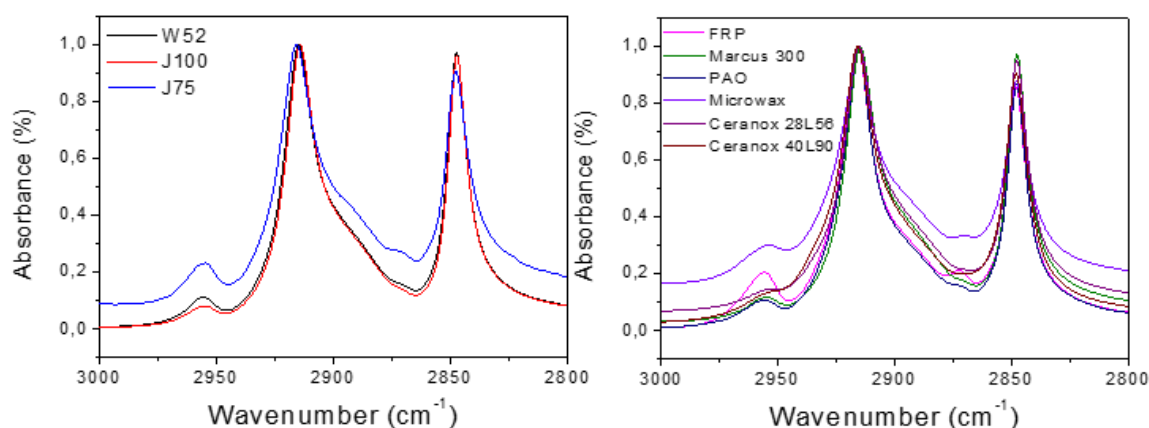


Figure 3.2: FTIR absorbance range of methylene (CH_2) and methyl (CH_3) stretching regions.

Characteristic methylene scissoring and rocking bands were observed at $1420 - 1480 \text{ cm}^{-1}$ and at $720 - 730 \text{ cm}^{-1}$, respectively. This area can assist in distinguishing between semicrystalline and amorphous material. Semicrystalline materials exhibit two bands in this area whereas amorphous materials show one broad band as reported by Hagemann et al.⁵⁵ when they examined the IR spectra of slow cooled and quench cooled polyethylene samples. These literature representations are illustrated in Figure 3.3. All wax samples in the study showed distinct splitting of both the scissoring and rocking absorbance bands as seen in Figure 3.4, indicating the semicrystalline nature of the waxes and the presence of orthorhombic crystalline packing.

Figure 3.5 shows the three fingerprint areas expected for a typical hydrocarbon wax sample (a) and a high-density polyethylene polymer (b). Notice that in the wax spectrum a band at 2960 cm^{-1} is visible due to methyl stretching vibrations. This band is absent for the polymer sample due to its much longer molecular backbone and thus significantly decreasing the methyl signals relative to the methylene backbone carbon signals. The main contributors of these methyl bands are the methyl groups at the ends of the main wax chain and the branched chain ends (if any branches present).

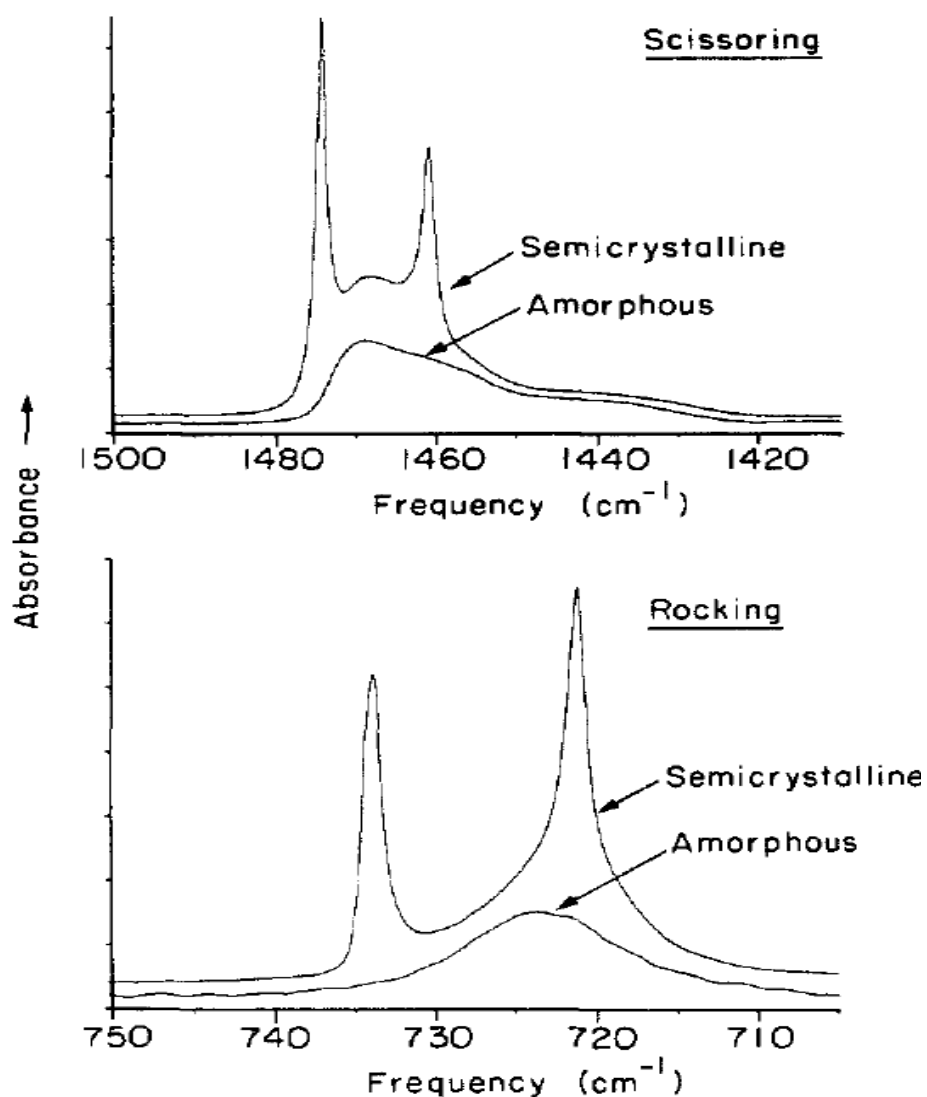


Figure 3.3: Methylene scissoring and rocking vibrations of slow cooled and quench cooled polyethylenes⁵⁵.

Evidence of oxidation (Figure 3.6) in both Ceranox waxes were clearly visible by the presence of strong carbonyl (C=O) stretching bands in the region 1800-1700 cm⁻¹ due to carboxylic acid (1716 cm⁻¹) (also confirmed by O-H stretching around 3450 cm⁻¹) and ester (1734 cm⁻¹) moieties. Carbonyl intensities were much stronger for the 40L90 wax implying a higher degree of oxidation. PAO showed a band at 1645cm⁻¹ indicative of alkene (C=C) unsaturated stretching vibrations. These bands were facilitated by alkene C-H bending bands at 910 and 990 cm⁻¹. It is therefore the only unsaturated hydrocarbon in this study.

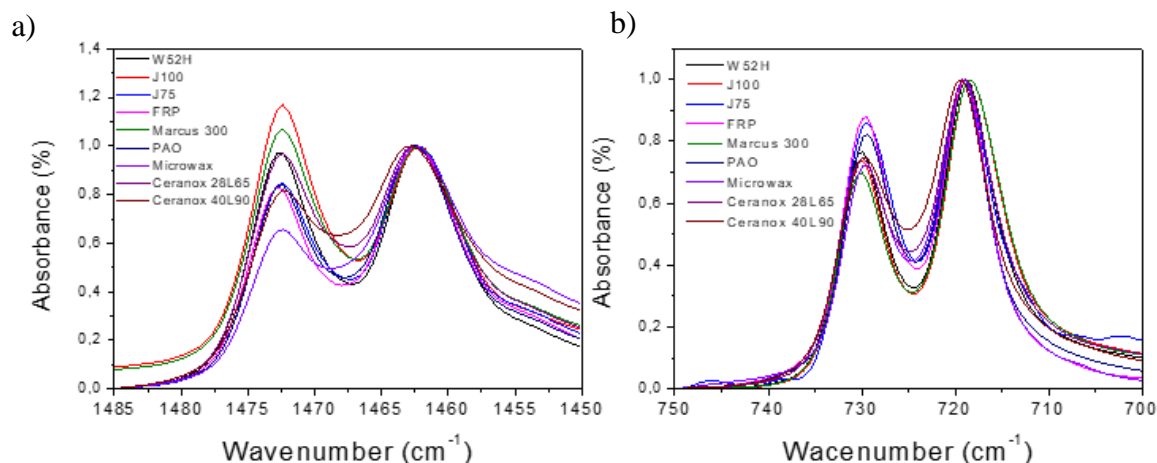


Figure 3.4: Normalized methylene a) scissoring and b) rocking bands.

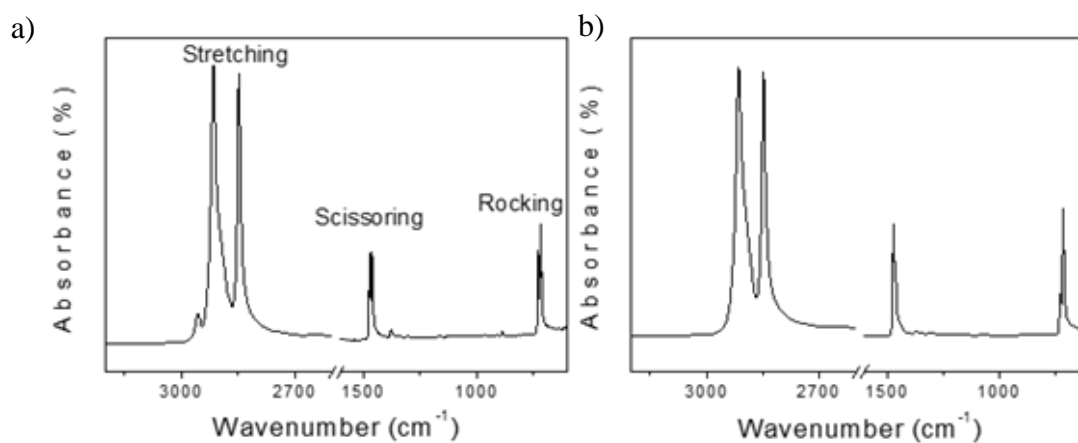


Figure 3.5 ATR-FTIR spectra of a) A typical hydrocarbon wax sample and b) A high density polyethylene polymer.

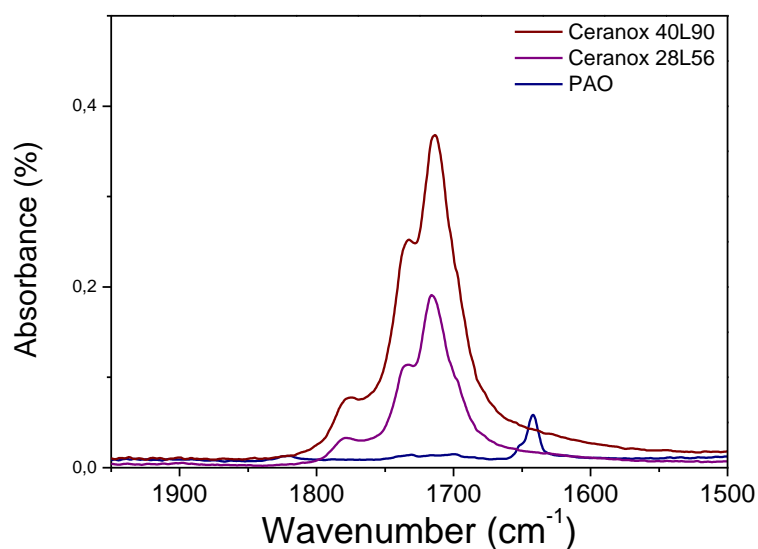


Figure 3.6: ATR-FTIR carbonyl (C=O) stretching and alkene (C=C) stretching vibrations.

3.1.3 ^{13}C Nuclear magnetic resonance spectroscopy (^{13}C NMR)

^{13}C NMR was used to determine the chain linearity and branching of the waxes but also to correlate chemical composition with FTIR analyses. Figure 3.7a shows all the highly linear waxes. These spectra had strong methylene backbone signals at 30.0 ppm accompanied by carbon signals at 14.2, 22.9, 32.2 and 29.6 ppm, associated with the 1s, 2s, 3s and 4s chain end carbons, respectively. Apart from these signals the spectra were clean indicative of linear hydrocarbon molecular chains. Together with the chain end signals, spectra in Figure 3.7b also showed some additional peaks arising from short chain branching along the molecular backbone. These peaks arising from α , β and γ carbons adjacent to butyl branches were observed at 37.6; 27.5 and 30.4 ppm, respectively. In the case of PAO wax, peaks associated with unsaturated alkene moieties were visible at 114 and 139 ppm, correlating with the FTIR findings. Figure 3.7c illustrates the NMR spectra for the two oxidized waxes and both showed distinct peaks at around 43 ppm arising from carbons situated in the alpha (α) position to a carbonyl moiety confirming the presence of oxygenate species in these two waxes. Apart from these peaks multiple other peaks were visible compared to the rest of the wax spectra, indicating the complex nature of the oxidized samples. In terms of chemical composition identification, NMR data correlate well with results obtained from FTIR.

3.1.4 Solid-state NMR (SS-NMR)

Solid-state ^{13}C cross polarized – magic angle spinning (CP-MAS) NMR was used to probe the chemical composition as well as the morphology of the waxes at room temperature (25 °C). Due to the cross-polarization dynamics involved, the rigid domains are sensitive to this method. In Figure 3.8 a pronounced methylene backbone signal associated with the rigid crystal structure can be seen at around 32.5 ppm. The shoulder at this peak seen for the first four samples (Ceranox 40L90, PAO, Microwax, and Ceranox 28L56) is due to methylene backbone situated in amorphous regions. These results correlated well to the results from the ^1H Wideline experiment (Figure 3.9), which was used to probe the rigidity of the waxes. From the width of a ^1H Wideline spectrum we can deduce the amount of sample in a rigid, intermediate or mobile state. The bottom, middle, and top half of the signal represents the rigid, intermediate, mobile states, respectively. Similar to the results seen from Figure 3.9, the first four waxes (Ceranox 40L90, PAO, Microwax, and Ceranox 28L56) exhibit the least amount of rigid material.

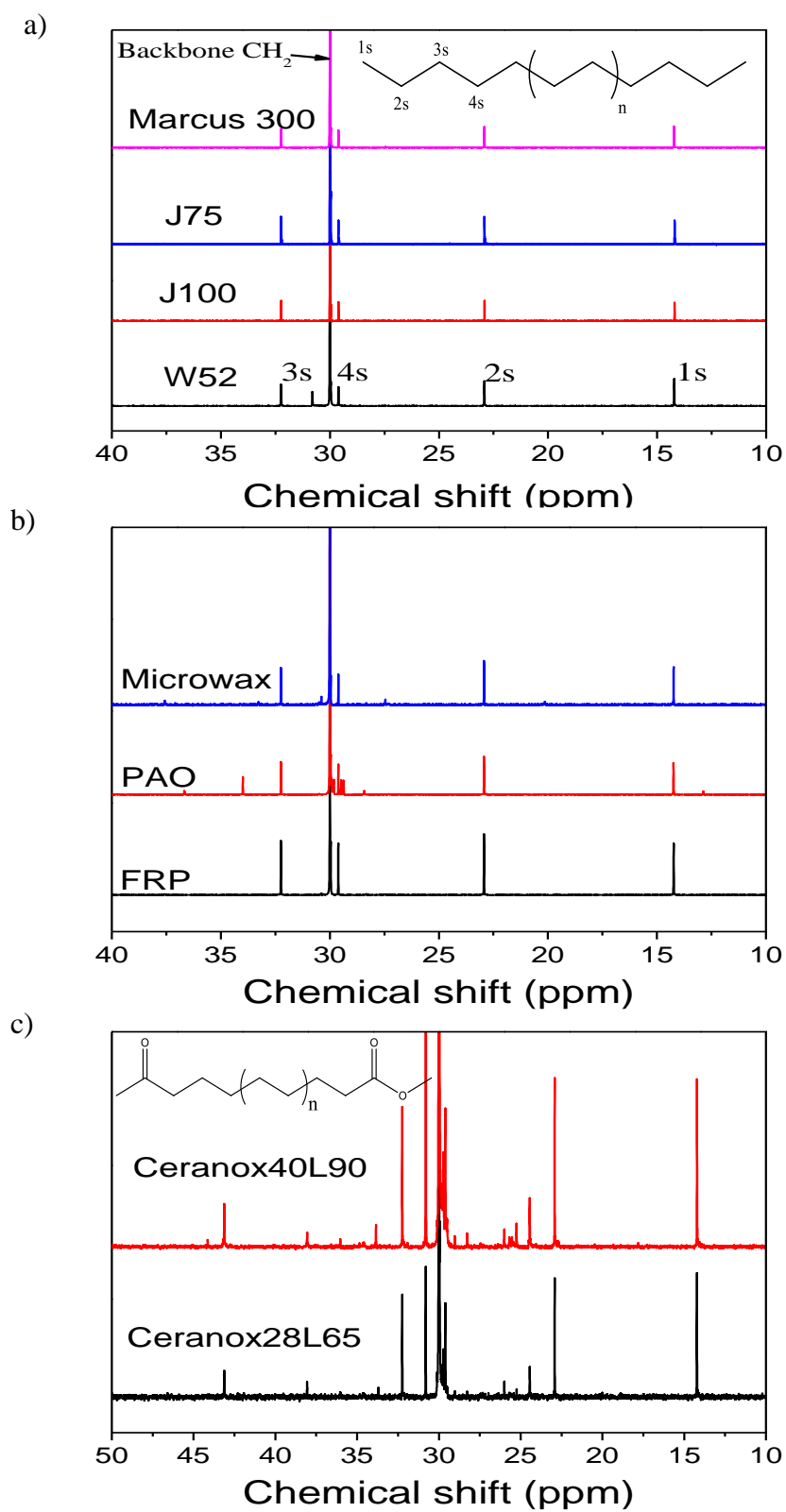


Figure 3.7: ^{13}C -NMR spectra of a) highly linear, b) branched and unsaturated, and c) oxidised waxes.

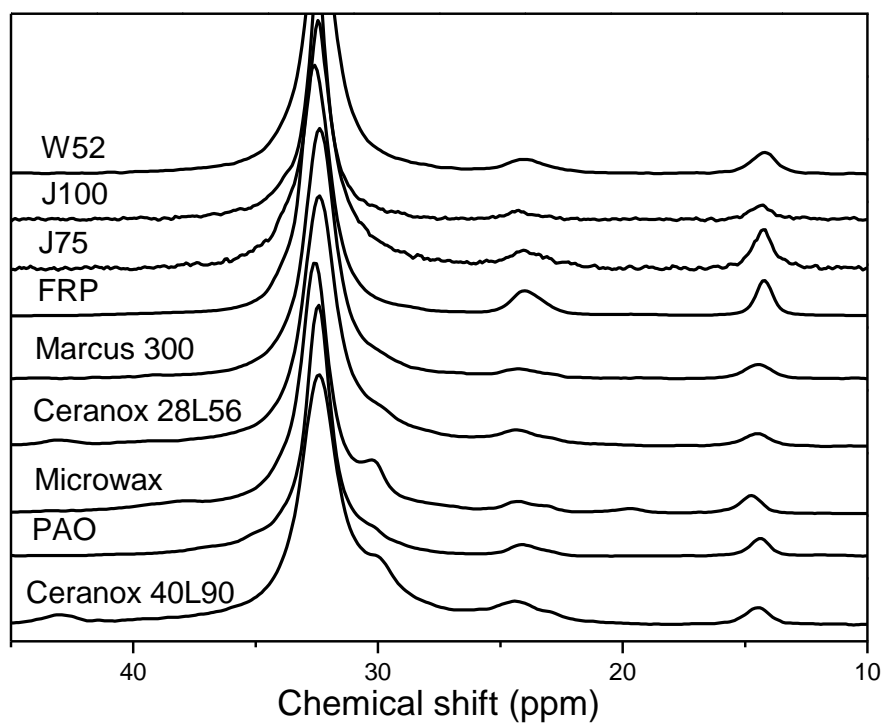


Figure 3.8: ^{13}C CP-MAS NMR spectra of Wax set 1.

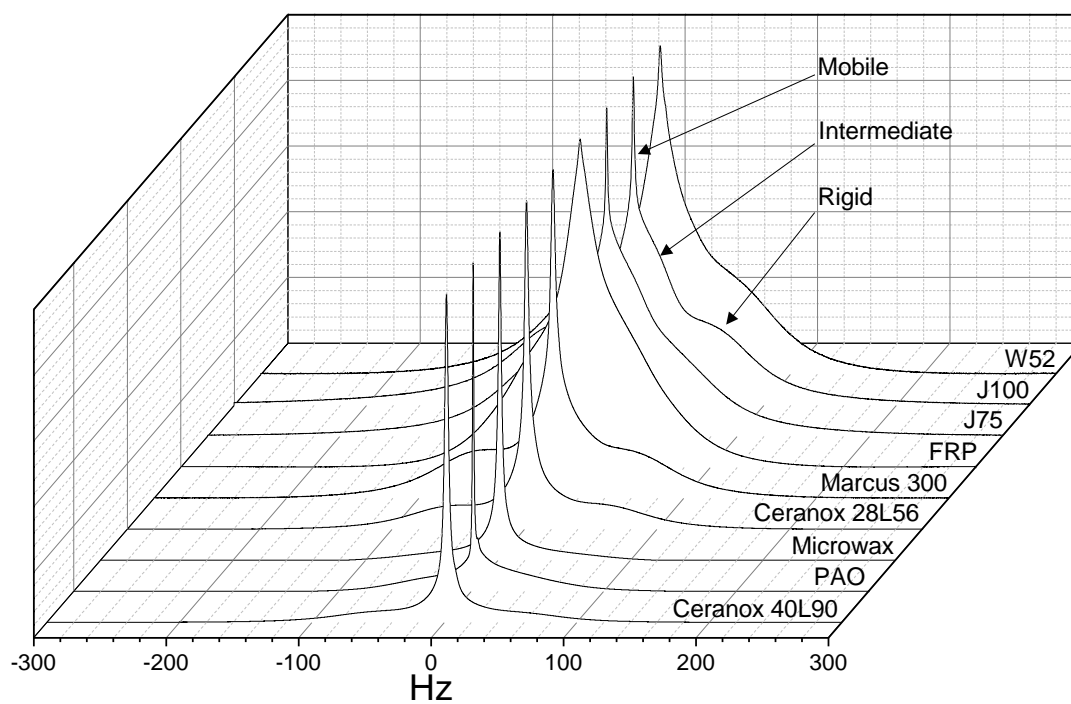


Figure 3.9: ^1H Wideline spectra of Wax set 1.

3.1.5 X-Ray diffraction (XRD)

X-Ray diffraction (XRD) allowed for the crystallite size (L) and d-spacing (d) within the waxes to be deduced. Crystallite size was calculated using the Scherrer equation given below.

$$B(2\theta) = \frac{K\lambda}{L\cos\theta} \quad \text{Equation 3}$$

Where L is the volume average of the crystal size, B is the full width at half maximum at position 2θ , K is a constant ($K = 0.94$) which depended on the function used to fit the peak and λ was the operational wavelength. D-spacing indicates the average distance of the same crystal faces between two adjacent crystals. The D-spacing was obtained using Bragg's law substituted for the dimensions of an orthorhombic unit cell. An example of an XRD spectra generated for one of the waxes is shown in Figure 3.10. All the waxes showed similar d-spacings. However, the crystal sizes differed to a certain degree. From work done by Salazar et al.⁵⁷ it is known that chain branching can increase the unit cell of a crystal. It therefore also increases the overall crystal volume or size. The XRD results are summarized in Table 3.3 and Figure 3.11 shows the crystal size distributions. W52, J100 and the two oxidized samples showed smaller average crystal size ($\leq 0.4 \text{ \AA}$). Crystal size for J75, FRP, PAO and microwax on the other hand were slightly larger. The crystal sizes arising from planes 110 and 200 were similar except for FRP which had a very large crystal size parameter when calculated from the 200 plane. FRP is also the only sample which exhibited a 3rd peak in between the 110 and 200 peaks. The paraffin wax therefore had a completely different crystal structure to the rest of the waxes.

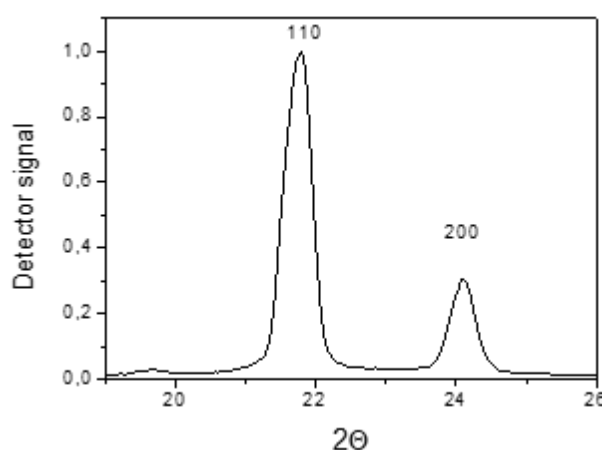


Figure 3.10: A typical XRD diffractogram obtained for the waxes (W52 sample illustrated).

Table 3.3: D-spacing and crystal size from respective XRD peak signals.

	Peak 1			Peak 2		
	2θ	d (nm)	L (\AA)	2θ	d (nm)	L (\AA)
W52	21.789	0.408	0.316	24.093	0.369	0.367
J100	21.789	0.408	0.404	24.123	0.369	0.337
J75	21.638	0.410	0.432	23.972	0.370	0.437
FRP	21.456	0.414	0.477	23.820	0.373	0.773
Marcus300	21.798	0.407	0.319	24.138	0.368	0.310
PAO	21.547	0.412	0.495	23.850	0.373	0.492
Microwax	21.698	0.409	0.461	24.032	0.370	0.434
Ceranolx 28L56	21.738	0.409	0.328	24.011	0.370	0.304
Ceranolx 40L90	21.698	0.410	0.324	23.880	0.370	0.318

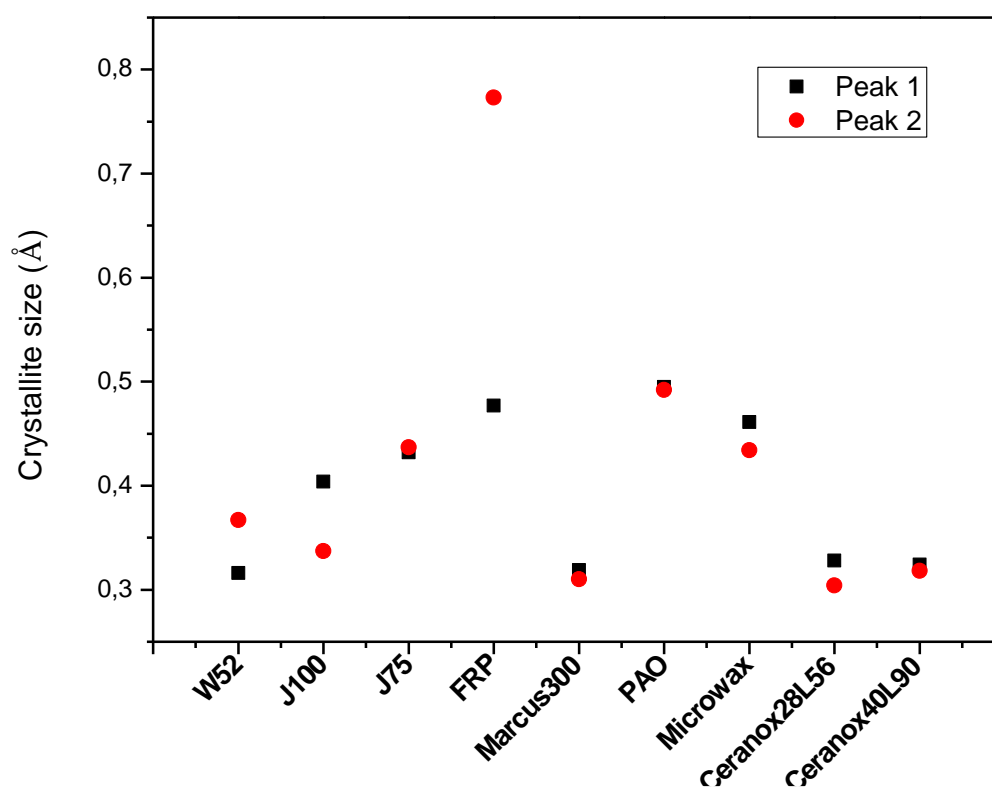


Figure 3.11: Crystallite sizes of waxes calculated from each crystal plane.

3.1.6 Differential scanning calorimetry (DSC)

Differential scanning calorimetry (DSC) allowed for separation of the waxes into two thermal groups. The first group (Figure 3.12a) displayed melting peak maxima below 85 °C and the second group (Figure 3.12b) displayed more endothermic melting events above this temperature. This temperature is significant as it is also the glass transition temperature (T_g) of PVC (Figure 3.13). Samples J75, FRP and PAO showed sharp, well-defined peaks and all the other waxes showed broad multimodal melting distributions. It is evident that W52 is the “parent” material of J100 and J75 and it clearly spans over the entire range of these two waxes. Endothermic peak temperatures and peak broadness from DSC is in good agreement with the trends seen in molecular weight and molecular weight distributions from HT-SEC with group 1 having the lower molecular weights and narrower molecular weight distributions when compared to group 2. The lower melting waxes, except for Ceranox 40L90, had larger crystal sizes. The higher melting waxes mostly evidenced smaller crystal sizes. Crystallinity was however independent of crystal size as could be seen from the two Ceranox waxes which had similar crystal sizes but different crystallinities. Ceranox 40L90 showed a lower crystallinity which might be due to the higher degree of oxidation as seen from the FTIR results. W52 had the highest degree of crystallinity (95.3%). FRP, J100 and PAO had crystallinities higher than 80%. Marcus 300 and Ceranox 28L56 had crystallinities around 70%. J75 was 60.5% crystallized. Microwax and Ceranox 40L90 had the lowest degree of crystallinity with values below 50%.

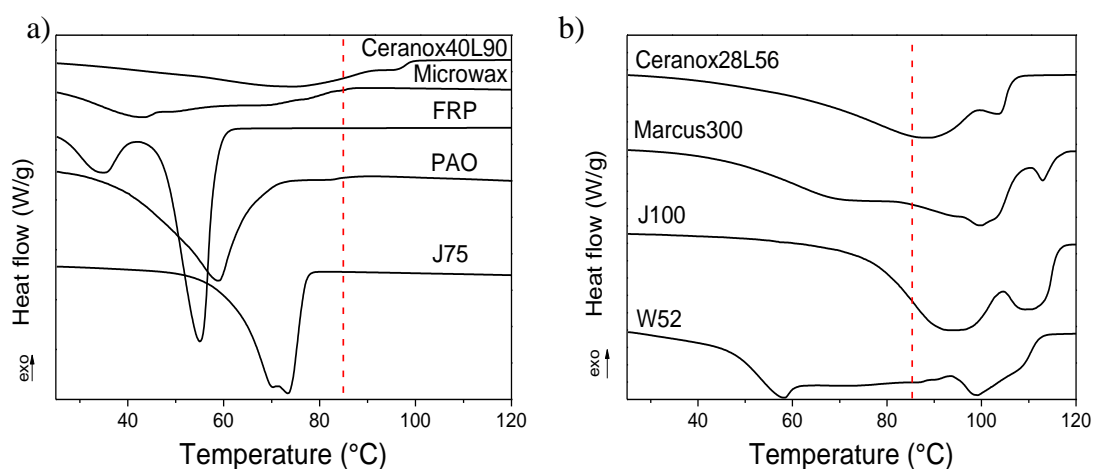


Figure 3.12: DSC melting endotherms of a) lower melting waxes (group 1) and b) higher melting waxes (group 2).

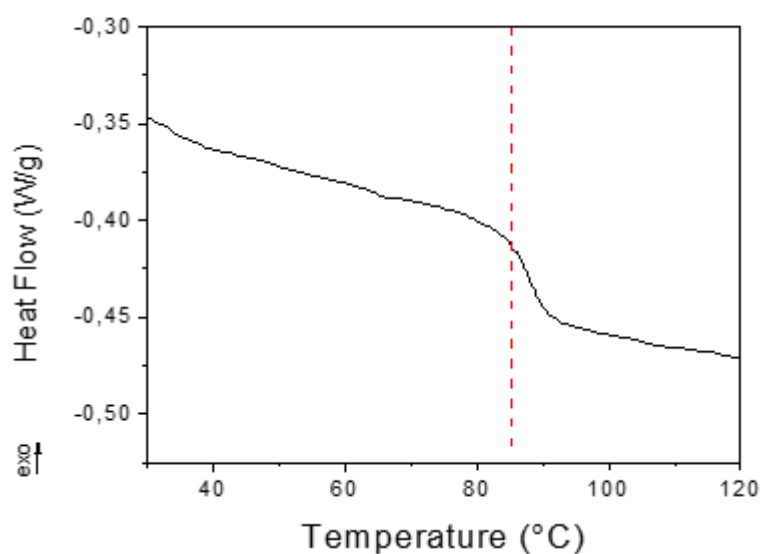


Figure 3.13: DSC thermogram of neat PVC showing its glass transition event.

Table 3.4: DSC results showing melting endotherm maxima, enthalpy, and percentage crystallinity.

	Onset of melting endotherm (°C)	Endotherm maxima (°C)	Melt Enthalpy (J/g)	Crystallinity ⁶ (%)
W52	44.7	58.2	279.2	95.3
J100	75.1	94.4	236.2	80.6
J75	61.6	73.4	177.3	60.5
FRP	55.0	55.1	263.5	89.9
Marcus300	53.8	100	211.9	72.3
PAO	41.6	58.9	241.6	82.5
Microwax	23.6	42.2	135.0	46.1
Ceranolx 28L56	52.1	89.2	210.6	71.9
Ceranolx 40L90	32.5	73.1	141.1	48.2

⁶ Standard heat of 100 % crystalline PE used was 293 (J/g).⁷⁵

3.1.7 Concluding remarks for stage 1 of the method development

A good knowledge and insight into the physical and chemical characteristics of the wax samples were gained in stage 1. All the waxes were fully characterized. Wax set 1 resembled a range of waxes with varying properties. Examining such a wide variety of waxes was necessary for establishing boundary conditions of the experimental technique. The next step was to move on to preliminary testing of stage 2.

3.2 Results and discussion of stage 2

Preliminary testing for stage 2 was done by selecting only a small set of additive combinations to determine if any differences in behaviour can be determined by the technique.

3.2.1 Scanning electron microscopy (SEM)

First it was essential to image a neat PVC particle which would allow a topographical image of the unchanged PVC particle surface. From this image any subsequent changes in the particle's morphology could be clearly deduced. The particle's surface (Figure 3.14a) showed a rough morphology with deep, unoccupied crevices. Figure 3.14b shows the calcium stearate occupying these crevices, indicating some physical or chemical association, and resulting in an all-round smooth surface morphology. J75 also occupied the crevices, but to a lesser extent than CaSt. The nonpolar hydrocarbon wax mostly occupied the rough crevices resulting in "pooling" in these spaces whereas the CaSt resulted in more all-round particle coverage. Interestingly, Figure 3.14d showed complete coverage and a smooth surface of the entire PVC particle. In Figure 3.14e, however the crevices were not filled, and differences compared to the neat PVC particle could be observed.

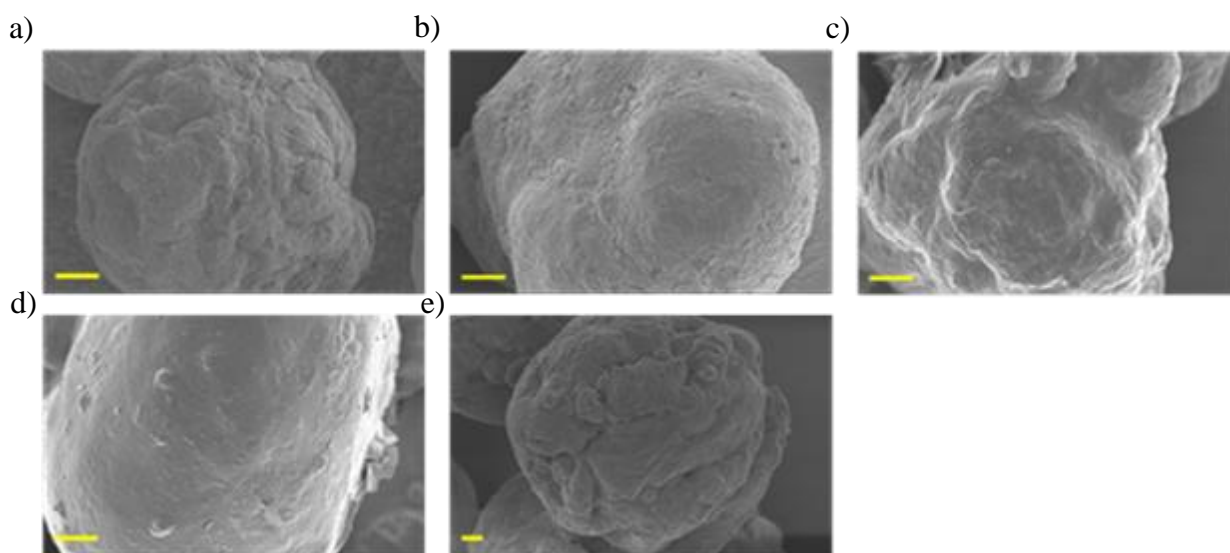


Figure 3.14: SEM electron images of a) PVC, b) PVC : CaSt, c) PVC : J75, d) PVC : CaSt : J75, e) PVC : Ceranox 40L90. Scalebar = 20 μm .

3.2.2 Scanning electron microscopy energy dispersive X-ray spectroscopy (SEM-EDS)

Even though some morphological deductions could be made from the electron images, in some cases it was still unclear as to which components were responsible for the particle coverage and morphological changes for example as seen in Figure 3.14d. As seen in this figure, the particle could preferentially be covered by either the wax, CaSt or both. It was therefore decided to use SEM coupled with energy dispersive x-ray spectroscopy (SEM-EDS) to elucidate the particle coverage through detection of individual elemental analysis throughout the images. This would allow for insight into the affinity and distribution of the various components across the PVC particles.

SEM-EDS images are shown in Figure 3.15. Signals arising from the various elements were assigned a different colour for ease of identification: Chlorine (blue), Carbon (red), Calcium = (purple) and Oxygen (green). In Figure 3.15a, a clear and uninterrupted blue chlorine signal of a neat PVC particle could be seen. Its corresponding carbon signal in red was not as strong. Both signals (Cl and C) were however also evenly spread throughout the particle as both were contributed from PVC. A strong red signal from carbon tape on which the samples were mounted, could be seen next to the particle, and should not be misinterpreted as signals from any of the blend components. In Figure 3.15b the chlorine signals were interrupted in certain regions across the particle and these appeared as darker spots on the surface. These regions overlapped with high intensity carbon signals and furthermore also corresponded to higher calcium signals. It was therefore concluded that the obstruction of chlorine signals was due to

the presence of calcium stearate internal lubricant on the surface of the PVC particles. It was however not yet clear on whether this was due to physical or chemical interactions. Figure 3.15c also showed an interference in the chlorine signal within the particle's crevices. These interruptions corresponded with high intensity carbon signals which indicated that the J75 wax got trapped in the crevices after mixing. This interruption of chloride signal was less than the amount of interruption from sample b, which indicated some additional PVC affinity of the partially polar CaSt when compared to the nonpolar wax. In the ternary blend (Figure 3.15d) it was seen that not only the crevices were occupied but a large part of the particle surface area was also occupied. The blue Cl signal was distinctly lowered. This indicates that CaSt might have facilitated some degree of association between PVC and the nonpolar J75 wax. Carbon and Calcium signals were both strong across most of the particle surface implying a more homogeneous distribution of internal and external lubricants compared to their binary blend counterparts. Figure 3.15e showed a less intense chlorine signal compared to Figure 3.15a indicating the presence of the polar wax on the particle surface. This deduction in Cl signal was substantiated by a stronger carbon signal in 3.15e compared to 3.15a, as well as strong oxygen signals from the polar oxygenated wax on the particle. From these SEM-EDS results, some clear deductions could be made from this method. It was therefore decided to continue stage 3 with this sample set.

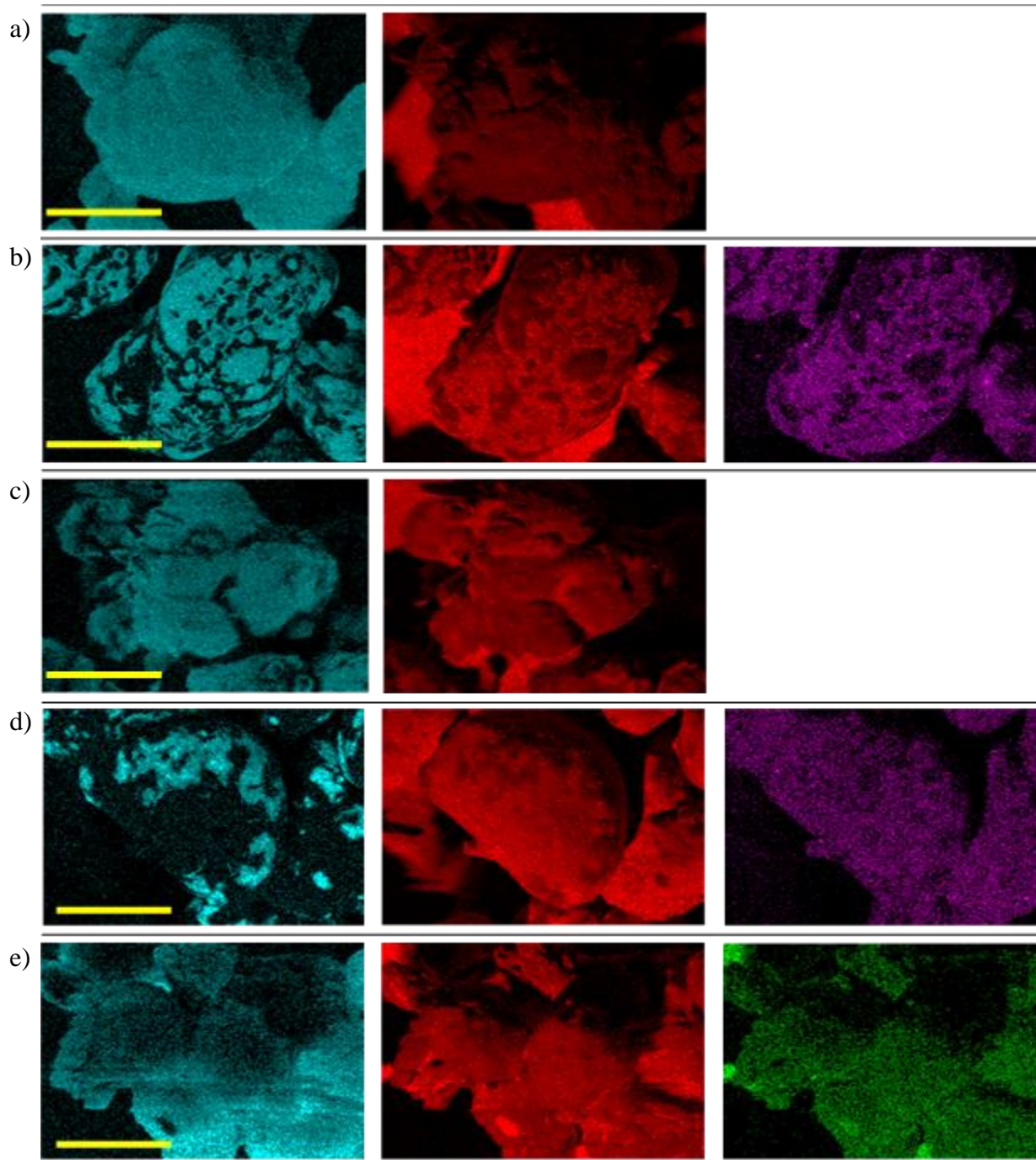


Figure 3.15: SEM-EDS images of PVC blends. a) PVC, b) PVC : CaSt, c) PVC : J75, d) PVC : CaSt : J75, e) PVC : Ceranox 40L90. (Scalebar = 100 μm , Chlorine = blue, Carbon = red, Calcium = purple, Oxygen = green)

3.2.3 Association interactions using DSC

To gauge if there were any inherent association interactions between any of the components during stage 2, a DSC experiment was proposed. Association interactions could be measured by means of the degree of miscibility between the components. A range of experiments was

set up to track the various melting endotherms of the lubricants as well as the glass transition temperature (T_g) of PVC. Miscibility was indicated by a convergence or shift in melting endotherm of a substance⁵⁸. In the case of PVC there was no endotherm. Miscibility could however be tracked by monitoring changes in the glass transition temperature⁷.

To investigate the association interaction of PVC and Calcium stearate (CaSt) various ratios of CaSt (0.5; 1; 10 phr) was subjected to a DSC experiment using 3 temperature cycles. The first heating cycle was set to 160 °C. Once this temperature was reached, samples were held isothermally at 160 °C for 15 minutes. In the second cycle the sample could cool down back to room temperature (25 °C). As the sample was heated again to 160 °C the third cycle was recorded (Figure 3.16). No effect on the T_g of PVC was observed indicating that there was no interaction between these two species.

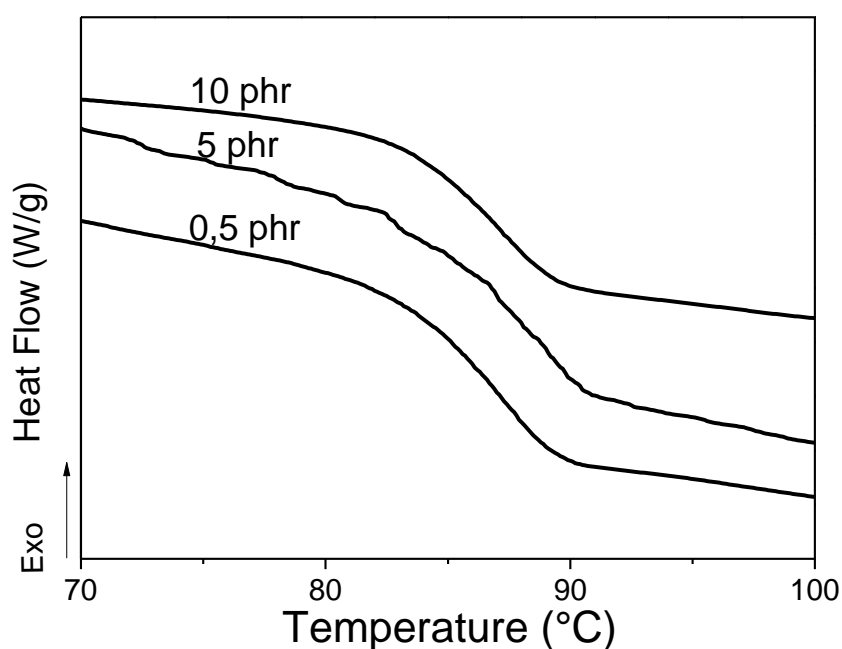


Figure 3.16: T_g of PVC with varying concentration of CaSt.

Table 3.5 lists some blends that were also assessed to investigate the interactions of wax with PVC and CaSt. A standard three temperature heating cycle was followed with a temperature range of 0 - 140 °C. Neat wax was analysed as the first sample. This was compared to a binary blend of wax with CaSt, a binary blend of wax with PVC and finally a ternary blend containing all three components. Figure 3.17 illustrates the thermogram overlays. No effect was seen on the T_g of PVC in either of the blends. The J75 melting peak does show a slight shift towards a

higher melting temperature which is due to some association between the two species. It was noticed that a peak associated with CaSt at 127 °C disappeared upon the second heating cycle (Figure 3.18). This peak was associated with the loss of water in Calcium stearate monohydrate, an effect noticed by Vold et al.⁵⁹.

Table 3.5: Blend compositions of wax with PVC and CaSt in phr.

Blend	Wax	PVC	CaSt
1	100		
2	50		50
3	10	100	
4	10	100	10

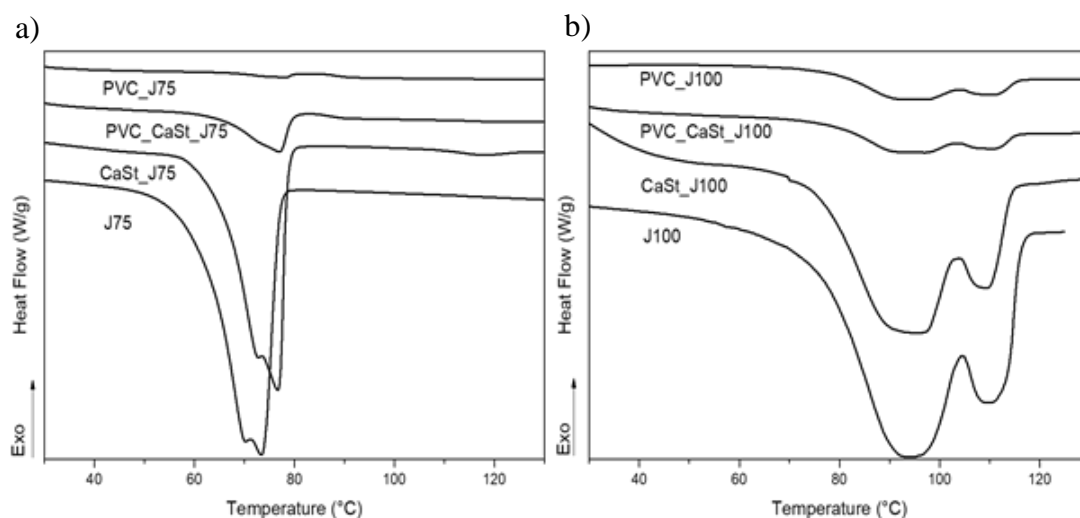


Figure 3.17: DSC melting endotherm overlays, a) J75 series and b) J100 series.

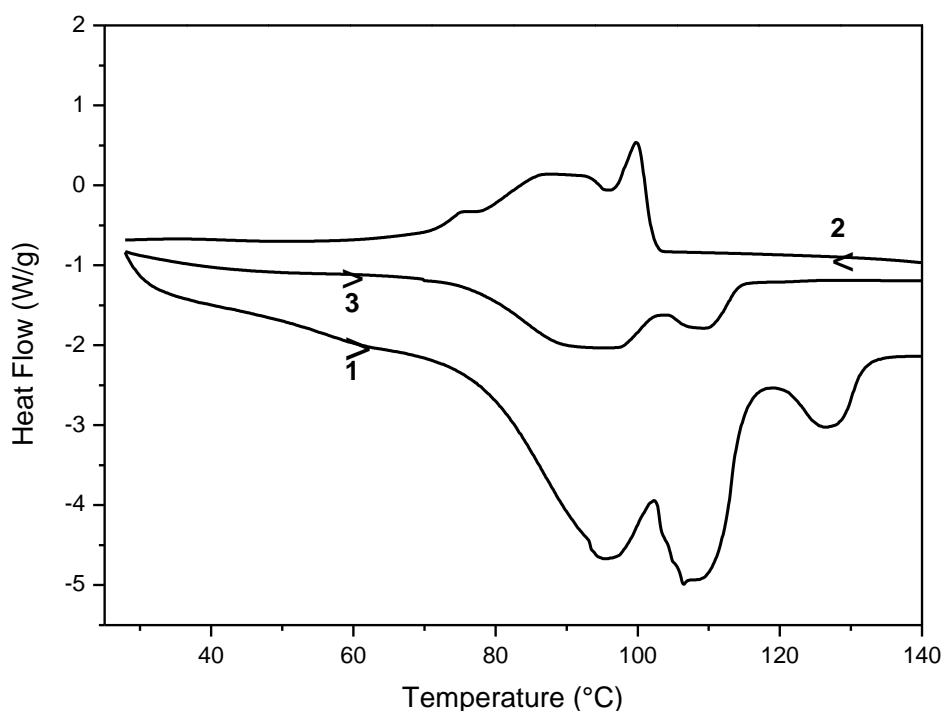


Figure 3.18: A typical DSC cycle of J100 showing the disappearance of CaSt monohydrate peak at 127 °C.

3.2.4 Concluding remarks for stage 2 of the method development

SEM-EDS results from stage 2 showed promising results as all of the constituents could be tracked using their specific element signals. The next step was to see if these components could be tracked in stage 3. The extent of the association interactions could not be quantified using DSC.

3.3 Results and discussion of stage 3

An example of an extruded PVC rod and cross section are shown in Figure 3.19. Figure 3.20 shows the carbon signals of part of a cross section for the different samples and Figure 3.20b shows the corresponding chlorine signal of Figure 3.20a. From the neat PVC sample (Figures 3.20a and b) a spiral like morphology could be observed. This was due to the polymer matrix folding onto itself in a spiral like fashion as the material moved towards the extruder die opening. A similar morphology was seen throughout the sample set. Two regions were identified in this system. The first was a nonpolar region (carbon signal in red) associated with hydrocarbon chains of the lubricants as well as a minor contribution of the polyethylene

cleaning agent used during the cleaning process between successive experimental runs and hence the red signals in Figure 3.20a. Second was the polar region (chlorine signal in blue) due to the PVC. By monitoring the signals of either one of these regions we could establish the distribution of lubricant within the system. When comparing the carbon signals of neat PVC with the other blends a clear difference could be seen. The blends with lubricant present showed much more interference of the polar PVC section as seen by the more continuous distribution of red carbon signals.



Figure 3.19: Example of an extruded rod and cross section imbedded in an epoxy resin.

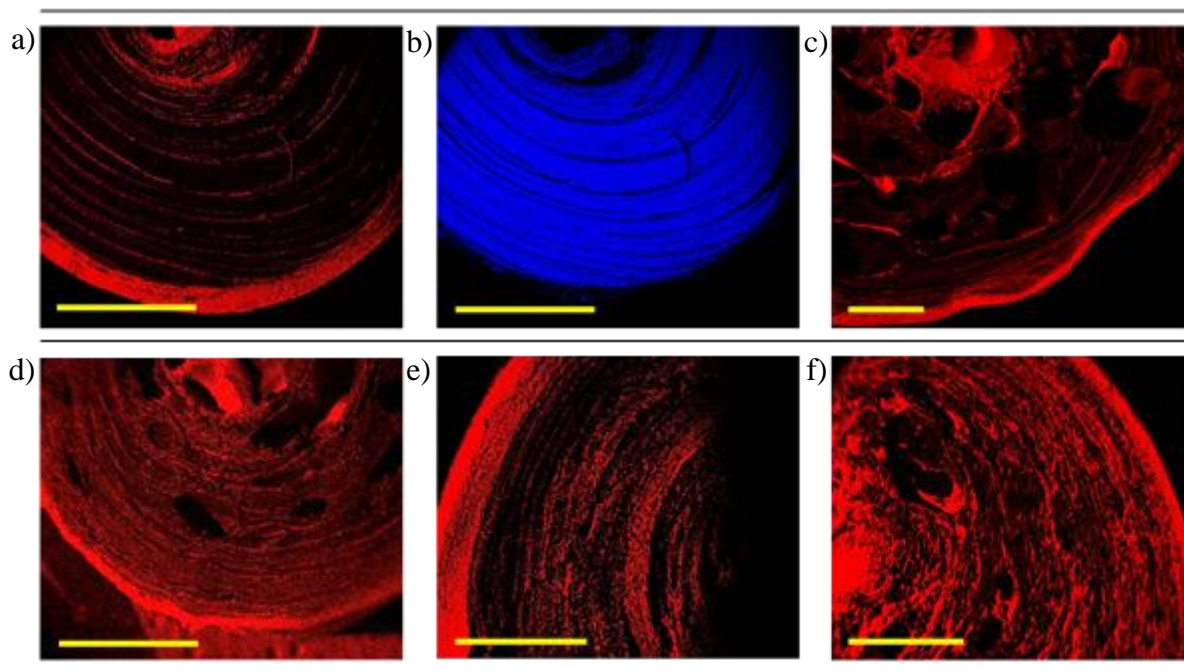


Figure 3.20: SEM-EDS images of rods from blends a) PVC (carbon signal), b) PVC (chlorine signal) c) PVC : CaSt, d) PVC : J75, e) PVC : CaSt : J75, f) PVC : Ceranox 40L90. (Scalebar = 2 mm, Chlorine = blue, Carbon = red)

3.3.1 Concluding remarks for stage 3 of the method development

In applying this method, the PVC could be fused while simultaneously tracking the final position of the components. This method showed promising results and was therefore applied to the complete set of waxes from category 1 and 2 in Stage 1 and discussed in the following Chapter 4.

Chapter 4: Method application

Some promising results were found from the method development process. It was therefore decided to apply the method to the entire range of waxes that were set out in the method development section. This range of waxes varied widely in thermal behaviour, chain mobility and molecular architecture. The following chapter was set up to see if it was possible to differentiate between the functioning of different these commercial waxes.

4.1 Binary blends

Binary blends consisting of only PVC and wax were investigated to determine if there were any inherent association interactions before the addition of the third component.

4.1.1 Stage 2

Experiment one involved the preparation and analyses of only binary blends of PVC : Wax (100 : 10 phr) in the absence of the CaSt. Figure 4.1 shows SEM-EDS images of binary blends during stage 2. Waxes were labelled as a) W52; b) J100; c) J75; d) Marcus 300; e) FRP; f) PAO; g) Microwax; h) Ceranox 28L56 and i) Ceranox 40L90. Electron micrograph images (Figure 4.1A, grey) did not show any significant differences in PVC particle surface morphology after melt-mixing with the various waxes. Samples a - d and g showed strong chloride signals (Figure 4.1B) with decreased carbon signal intensities (Figure 4.1C). However, samples e, f, h and i showed some hindrance of the chloride signals, as observed by darker regions on the PVC particle surfaces and this was accompanied by high intensity carbon signals. The higher intensity carbon signals indicate the presence of some wax on the particle surface and partial coverage of the PVC particles. This was an interesting finding as all four of these waxes had different microstructures. Sample (e) was a predominantly linear wax, sample (f) contained unsaturated alkene moieties and samples (h) and (i) were oxidized to different degrees. Some association could be observed, but no conclusion could be drawn as to why there was association. Although samples (a), (b), (c) and (g) did not cover vast areas of the PVC particles, higher intensity carbon signals were visible in the uneven crevices of the particles, indicating that physical “trapping” or “pooling” of these waxes occurred rather than chemical associations.

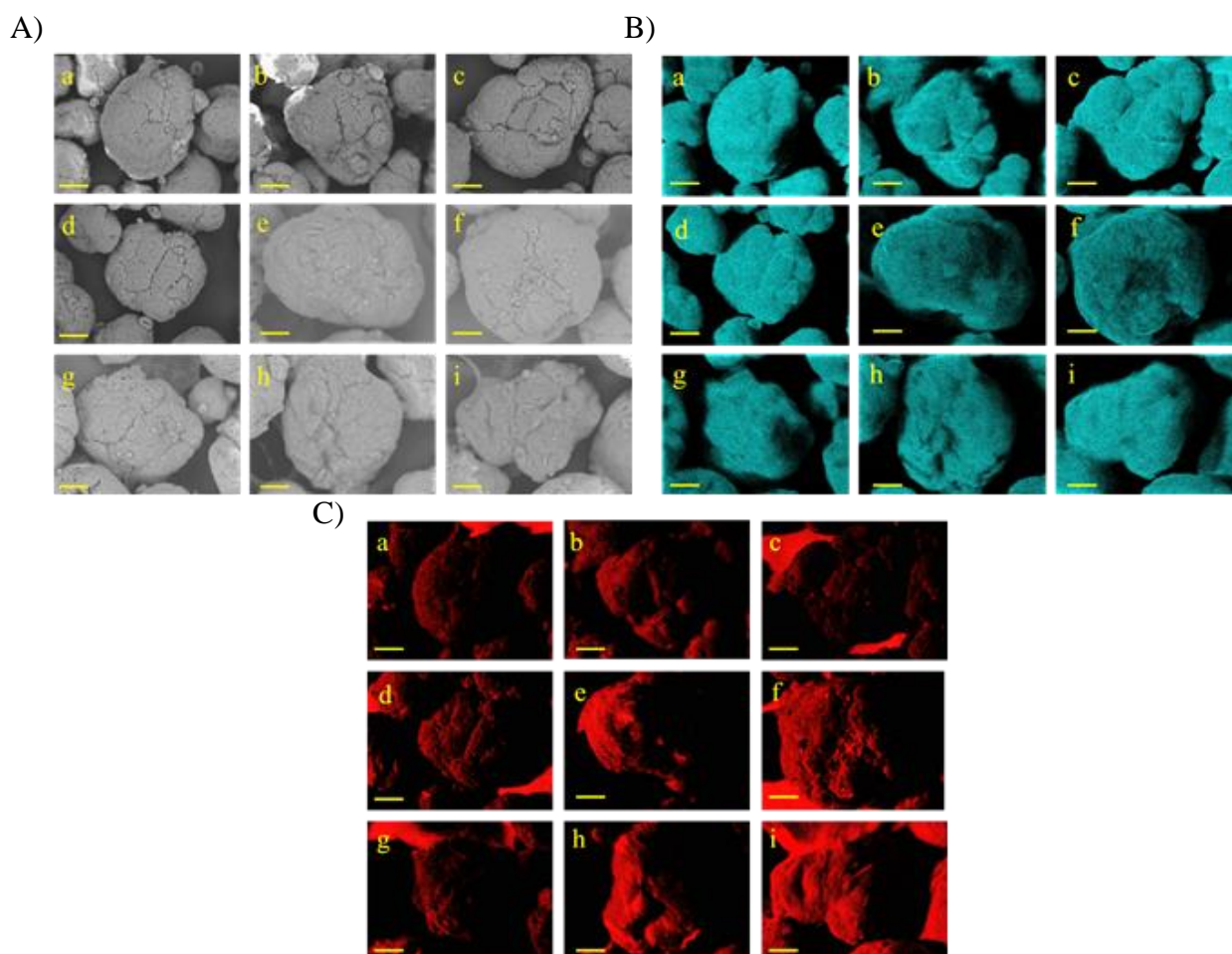


Figure 4.1: SEM-EDS images of binary PVC : Wax blends during Stage 2: a) W52; b) J100; c) J75; d) Marcus 300; e) FRP; f) PAO; g) Microwax; h) Ceranox 28L56; i) Ceranox 40L90. Electron image = grey (A). Chloride = blue (B); Carbon = red (C). Scalebar = 20 μ m.

4.1.2 Stage 3

Samples were extruded to observe lubricant migration during stage 3. Figure 4.2 shows SEM-EDS images of the whole sample set. Throughout the full set a very heterogeneous dispersion of chloride signals was observed. Overlays of the electron image, chloride signals and carbon clearly illustrate some phase separated behaviour for the hydrocarbon waxes (a – g). More significant differences in chloride and carbon signals were observed for these set of waxes. More overlap between the PVC and wax signals were observed for the binary blends containing the two polar waxes. In sample (a), the chloride signals were scattered and showed some individual particles, indicating that the PVC did not fuse properly. No conclusion could be drawn as to whether there was any association when using waxes (e), (f), (h) and (i), which showed enhanced particle coverage in stage 2, to whether it had any effect on the migration in stage 3. In stage 3 the wax was randomly scattered with no preferential association interactions governing the migration pattern.

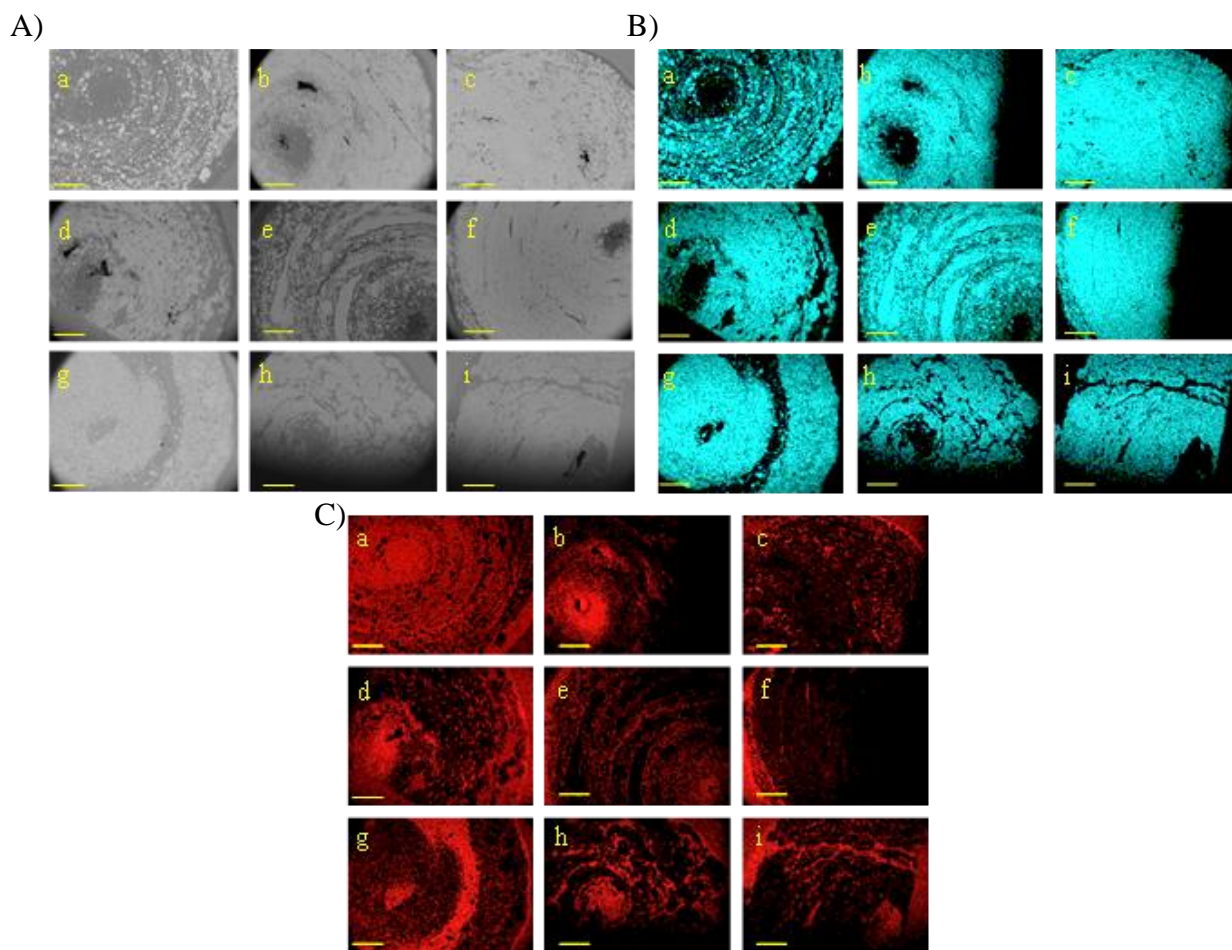


Figure 4.2: SEM-EDS images of binary PVC:Wax blends during Stage 3. a) W52; b) J100; c) J75; d) Marcus 300; e) FRP; f) PAO; g) Microwax; h) Ceranox 28L56; i) Ceranox 40L90. Electron image = grey (A). Chloride = blue (B); Carbon = red (C). Scalebar = 2mm.

4.2 Ternary blends

Experiment 2 was done to observe the effect of adding the internal lubricant, calcium stearate (CaSt), to the binary blend.

4.2.1 Stage 2

Ternary blends consisting of PVC (100 phr), wax (5 phr) and CaSt (5 phr) were prepared by high-speed mixing at elevated temperatures above the melting point of the wax and CaSt components, and thereafter analysed. SEM-EDS electron images and elemental maps are shown in Figure 4.3. Compared to the electron images of the binary blends (Figure 4.1), a distinct difference in wax inclusion could be seen on the particle surfaces. In the ternary blends, PVC particles were clumped together, and the lubricants appeared as dark grey spots on and between the particles. These dark spots directly correlated to a hindered chloride signal seen in

Figure 4.3B. EDS elemental images further confirmed that these dark grey spots could be attributed to both the wax and CaSt as seen by the correlative increase in signal intensities in both the carbon and calcium spectra (Figures 4.3C and 4.3D). It was therefore concluded that addition of CaSt increased the association of wax to PVC. A notable difference that was also observed was the difference in CaSt association towards polar and nonpolar waxes. For the nonpolar waxes, CaSt increased the particle coverage and distribution throughout the particle surface. However, for the polar waxes the wax seemed to accumulate more within the particle crevices than on the particle surface. These behaviours were clearly observed by the carbon and calcium signals where the nonpolar blends (a – g) showed high elemental intensities across particle surfaces whereas the polar blends (h and i) showed decreased surface intensities and higher intensities in-between particle and particle crevices.

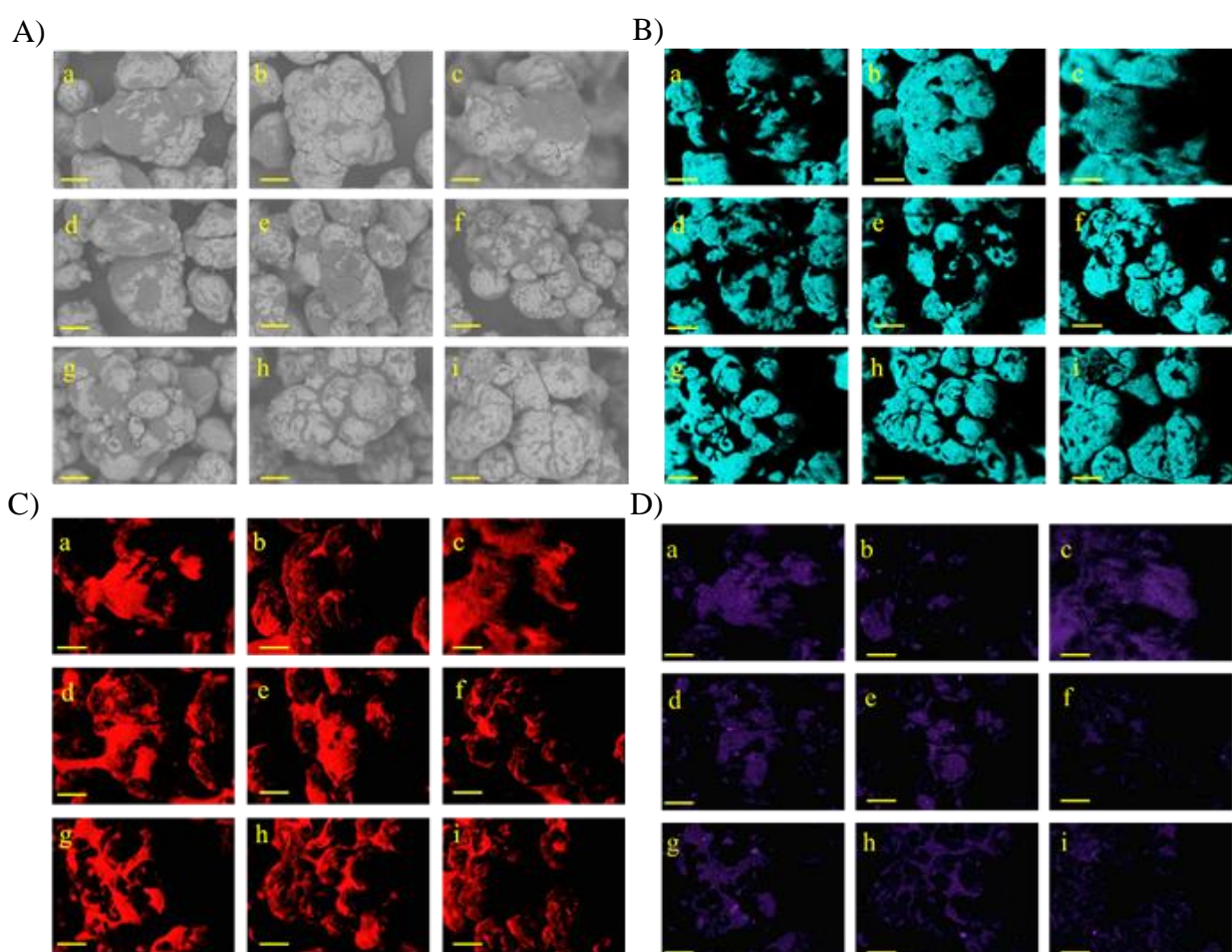


Figure 4.3: SEM-EDS images of ternary PVC : CaSt : Wax blends during Stage 2. a) W52; b) J100; c) J75; d) Marcus 300; e) FRP; f) PAO; g) Microwax; h) Ceranox 28L56; i) Ceranox 40L90. Electron image = grey (A). Chloride = blue (B); Carbon = red (C); Calcium = purple. Scalebar = 2 mm.

4.2.2 Stage 3

In stage 3 of the ternary blends (Figure 4.4) a much different behaviour was observed on the migration pattern than compared to the binary blends (Figure 4.2). Wax distribution was more uniform with the chloride and carbon signals being homogeneously spread throughout the entire cross-sectional area of the extrudate. One exception to this pattern was the oxidized waxes which showed a heterogeneous phase separated distribution in the ternary blend as opposed to a homogeneous spread in its binary blends. Combined data from binary and ternary blends through the two different stages (2 and 3), indicates that the CaSt facilitated associations of the nonpolar waxes with PVC whereas the polar waxes/PVC associations appeared to be hindered in the presence of CaSt. Affinity of internal and external lubricants for each other might have been stronger than that of lubricant/PVC affinities resulting in less particle coverage for the polar ternary blends.

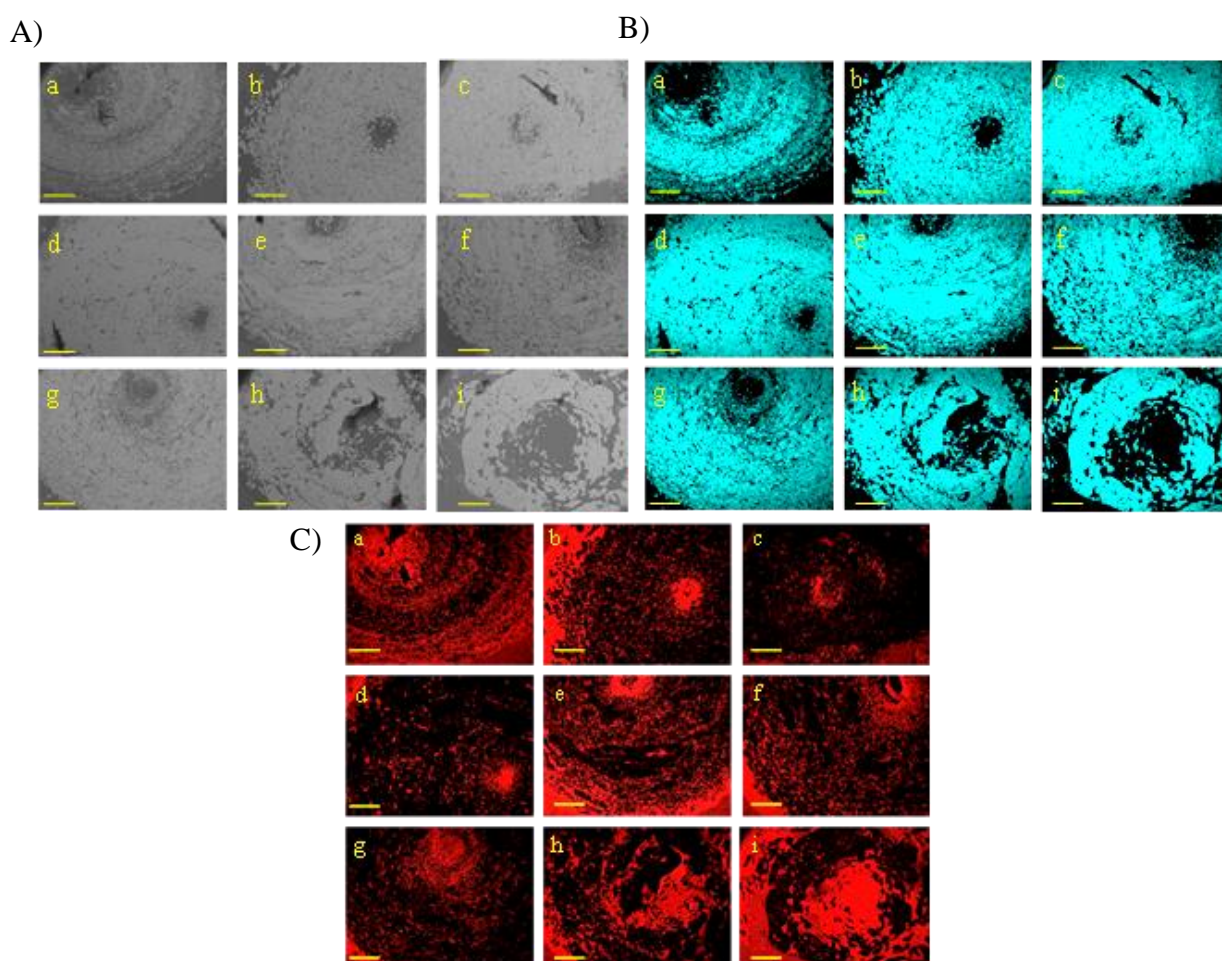


Figure 4.4: SEM-EDS images of ternary PVC : CaSt : Wax blends during Stage 3. a) W52; b) J100; c) J75; d) Marcus 300; e) FRP; f) PAO; g) Microwax; h) Ceranox 28L56; i) Ceranox 40L90. Electron image = grey (A). Chloride = blue (B); Carbon = red (C); Calcium = purple (D). Scalebar = 2mm.

4.3 Concluding remarks to Chapter 4

A distinct difference in behaviour could be seen when comparing polar to nonpolar waxes with and without CaSt. A deeper discussion into these findings were given in a research paper published by our research group titled, “Tracking lubricants during single screw extrusion of uPVC”. In this peer reviewed manuscript (Chapter 5) the in-house developed method is discussed as well as the differences in association interactions between polar and nonpolar waxes in binary and ternary systems.

Chapter 5: Peer-reviewed manuscript published in Polymer Testing journal

The following manuscript is based on the findings of the method development section.

Tracking lubricants during single screw extrusion of uPVC.

J.L. Barnard, D.D. Robertson, A.J. van Reenen

*Department of Chemistry and Polymer Science, University of Stellenbosch, Private Bag X1,
7602 Matieland, South Africa*

Corresponding Author: A.J. van Reenen. e-mail: ajvr@sun.ac.za

Abstract

Lubrication is one of the most important parameters in unplasticized polyvinyl chloride (uPVC) processing apart from the PVC resin and processing equipment. Lubricants are used in specific ratios to ensure effective fusion of PVC particles. The exact mechanism on how these lubricants interact is not yet fully understood. A widely accepted theory is the interaction mechanism proposed by Rabinovitch et al. where lubricants are said to function as surfactants and slip agents. In this study a method for tracking lubricants, by simulating the extrusion process within a single screw extruder, was proposed. A three-stage fusion simulation consisted of the feeding zone (stage 1), the compression zone (stage 2) and the metering zone (stage 3). The association interactions between the individual components of a typical uPVC formulation were followed throughout the three stages. External polar and nonpolar lubricants in combination with an internal lubricant was studied. Lubricants were successfully tracked using scanning electron microscopy coupled with energy dispersive spectroscopy (SEM-EDS). In conclusion it was found that the use of an internal lubricant promotes dispersion of external lubrication towards PVC. It was also found that there is a competition between the internal lubricant and polar external lubricant.

Keywords: Single screw extrusion, uPVC, lubricant, migration, SEM-EDS, fusion

5.1 Introduction

Polyvinyl chloride (PVC) is the second most produced polymer in the world behind polyolefins^{2-4,9,60}. PVC is widely used in the building industry where the primary applications include water piping and frames for doors and windows^{3,60-63}. Other main consumers of PVC include the packaging and cosmetic industries³. Unplasticized PVC (uPVC) together with plasticised and chlorinated PVC each contribute a third of the PVC used for piping globally⁶⁴. Production of uPVC piping is impossible without the use of various additives such as lubricants, processing aids and heat stabilizers.

According to Rabinovitch et al.³¹ the use of lubricants is one of the three most important parameters in uPVC processing, despite its very low concentrations within the PVC formulations. The other two parameters are the PVC resin and the processing equipment. Precisely how lubricants perform their function within these formulations has been the subject of much speculation and still has not been proven definitively.

Lubricants are classified as either external or internal. External lubricants are classified as having no chemical association with the polymer matrix. They are active at the polymer metal surface where they promote metal release and therefore delay fusion³³. Internal lubricants are classified as having chemical association with both the polymer matrix as well as the external lubricant. They are said to reduce melt viscosity and act as fusion promoter¹⁶.

Fusion occurs when efficient friction, heat and pressure is applied to a PVC formulation. Primary PVC particles are broken down during this process allowing diffusion and entanglement of PVC chains. PVC particle surface boundaries disappear and a continuous three dimensional PVC matrix is created⁶⁵. Efficient fusion is a very important parameter in PVC processing and is directly related to the final properties of a PVC product¹⁹.

With regards to the processing of uPVC, various research groups have attempted to elucidate the role of lubricants during extrusion^{24,31,33,35,66,67}. Rabinovitch et al. investigated the lubrication mechanism by examining macroscopic properties of uPVC formulations. These measured parameters included metal release, fusion time, fusion temperature, percentage haze, changes in glass transition temperature of the PVC and rheological properties. Using transmission electron microscopy (TEM) and scanning electron microscopy (SEM), Rabinovitch et al. visually interpreted how lubricants interact with the PVC matrix. Thereafter

a mechanism of how internal and external lubricants should be classified as surfactants and slip agents, was proposed.

Summers et al.¹⁶ confirmed the aforementioned mechanism by showing that lubricant failure is due to lubricant inversion from the continuous phase to a discontinuous phase with increasing melt temperatures. This was done using SEM coupled to energy dispersive x-ray spectrometry (SEM-EDS) where the Calcium (Ca) element of the Calcium stearate could visually be detected after fracturing of fused specimens. In that study Summers and co-workers used the assumption that non-polar waxes were only present in the other nonpolar areas in this system, namely the nonpolar stearate tails.

Functional waxes with characteristics of both internal and external lubricants have been the focus of more recent studies due to their effect on minimizing plate-out^{4,9,39,60,68}. Plate-out occurs when additives such as stabilizers migrate out of the PVC matrix with an external lubricant. It was therefore necessary to produce an external lubricant with a slightly higher polarity which would minimize migration³⁹. Examples of such lubricants include Amide and Ester based waxes⁹. It was however found that functional waxes, in addition to minimizing plate-out, exhibit advantageous properties of both internal and external lubricants. Beneficial internal lubrication properties such as shorter fusion times, lower operating pressures and torques are gained as well as comparable gloss finishes to those achieved using external waxes³⁹. These functional waxes also have the bonus of being used in much lower concentrations than when using a conventional internal/external wax combination. Until now, however, all formulations with functional waxes are still stabilized with some sort of Zn/Ca stearate internal lubrication⁴⁰.

The current study was pursued to further investigate the various mechanisms of lubricant interactions with the PVC matrix proposed in previous literature. SEM-EDS was the integral method used to track the individual components within a uPVC formulation during processing. This work gave some insight into the interactions of the individual lubricants with each other as well as the associations with the PVC matrix. A nonpolar and polar external lubricant system in combination with a Calcium stearate internal lubricant was studied.

5.2 Materials and methods

5.2.1 Materials

To investigate the mechanism at hand we selected a suitable PVC resin commercially available from Shintech (SE-950). Calcium Stearate from Chemson was selected as internal lubricant. A linear hydrocarbon wax was used as external lubricant (nonpolar). It was also decided to look at an oxidized hydrocarbon wax (polar) to investigate the effect it had on lubrication. Additives were included in excess amounts to ensure their observation during spectroscopic analysis (Table 1).

5.2.2 Technique

A strategy was devised to track lubricant migration using a spectroscopic technique. SEM-EDS was the principle technique of choice. It was used to visually track every component in the formula. Each component had a unique element that distinguished it from the others. For PVC, this element was chloride (Cl), for calcium stearate it was the calcium (Ca), for the hydrocarbon it was the carbon (C) and for oxidised wax it was the oxygen (O).

Tracking of these individual components was done by determining their physical positions visually at three different stages. The stages were chosen to simulate the extrusion process. Stage I was the neat characterisation of the individual components i.e. position 1. Stage II was the process of mixing at elevated temperatures i.e. position 2. Stage III simulated the fusion process i.e. the final position of migration.

5.3 Experimental

5.3.1 Sample preparation for all three stages:

5.3.1.1 Stage I

Samples were characterized as is with no prior modification.

5.3.1.2 Stage II

Binary and ternary mixtures were hot melt blended by overhead stirring at 165 °C for 15 minutes. This temperature was chosen to ensure all the components were above their melting temperatures. Mixtures and their components are listed in Table 5.1.

Table 5.1: PVC formulations used for stage II and III

Sample	Amounts (phr)			
	PVC	CaSt*	Nonpolar	Polar
a	100	-	-	-
b	100	10 and 5	-	-
c	100	-	10	-
d	100	-	-	10
e	100	10 and 5	10	-
f	100	10 and 5	-	10

*Internal lubricant was lowered to 5 phr for stage III to minimise gas build-up within the extruder.

5.3.1.3 Stage III

For stage III, the amount of calcium stearate was reduced to 5 phr to avoid gas build-up inside the extruder (Table 5.1*). Samples were high speed mixed with an overhead stirrer for 15 minutes, thereafter mixtures were subsequently extruded. Extrusion was done on a Brabender Plasticorder PLE 651 extruder with the single screw barrel attachment (L/D = 26.5:1). The barrel was preheated on three of the four sections. Section one, the feed section, was heated to 145 °C. The compression section was heated to 155 °C and the metering section was heated to 190 °C. The die area which can also be heated was removed and replaced with a short die (L/D = 5/1). Removing this section (thus also removing the breaker plate which causes turbulent flow) caused molten polymer to maintain its directional flow. Sampling at this interval allowed for a direct interpretation of how the molten polymer matrix and the additives were interacting during directional flow. This technique is further explained in the following sections.

Approximately 9 mm diameter cross sections of the extruded material were then embedded in epoxy resin and cured in an oven at 40 °C for 24 hours. Thereafter the embedded samples were polished with 9 µm (10 min), 3 µm (15 min) and 1 µm (15 min) grit polishing discs on a rotational polisher until a uniformly polished area could be observed through a light microscope.

5.3.2 Sample characterization techniques

Stage I

Neat materials were characterized according to their molecular size, chemical composition, chain linearity and branching, and thermal behaviour using the following techniques.

5.3.2.1 High temperature – size exclusion chromatography (HT-SEC)

Determination of the molecular weights and molecular weight dispersity was carried out on a PL220 high temperature chromatography instrument (Polymer laboratories, Varian, Church Stretton, Shropshire, England) coupled to a differential refractive index (RI) detector. Polyethylene standards were used for calibration. Samples (4 mg) were dissolved in 1, 2, 4 – trichlorobenzene (TCB) with 0.025% butyl-hydroxy-toluene (BHT) stabilizer. The mobile phase had a flow rate of 1 mL/min. The stationary phase consisted of three $300 \times 7.5 \text{ mm}^2$ PLgel Olexis columns (Agilent Technologies, UK) together with a $50 \times 7.5 \text{ mm}^2$ PLgel Olexis guard column. Sample volumes of 200 μL were analysed at 150 °C.

5.3.2.2 Attenuated total reflectance – Fourier transform infrared spectroscopy (ATR-FTIR)

Analyses were conducted on a Thermo Scientific Nicolet iS10 FTIR spectrometer with a diamond crystal. Scans were performed at a resolution of 4 cm^{-1} and 64 scans were taken. OMNIC (version 9) processing software was used for data analysis.

5.3.2.3 ^{13}C Nuclear magnetic resonance (^{13}C -NMR)

^{13}C -Nuclear magnetic resonance (^{13}C -NMR) spectra were acquired on a Varian^{Unity} INOVA 600 MHz liquid state NMR Spectrometer at 120 °C. A 90° pulse angle with acquisition time of 0.87 s and relaxation delay of 15 s was used. Detailed structural information on the waxes could be deduced from this technique.

5.3.2.4 Differential scanning calorimetry (DSC)

Endothermic melting and exothermic crystallization behaviour of the samples were analysed by using a TA instruments Q100 differential scanning calorimeter, calibrated with indium metal according to standard procedures. A three-step cycle was implemented wherein each sample (4 mg) was heated from room temperature to 200 °C in the first cycle at a heating rate of $10 \text{ }^\circ\text{C}\cdot\text{min}^{-1}$, this was done to remove any thermal history of the samples. Samples were kept isothermally at 200 °C for 3 minutes, after which they were cooled to 25 °C at $10 \text{ }^\circ\text{C}\cdot\text{min}^{-1}$. During the last step, the temperature was kept isothermally at 25 °C for 3 minutes and then heated to 200 °C. Only data obtained from the second heating cycle was processed for all the thermal analysis calculations. The DSC measurements were conducted in an inert nitrogen atmosphere at a purge gas flow rate of $20 \text{ ml}\cdot\text{min}^{-1}$. Data was analysed using TA universal analysis software.

Stage II and III

After undergoing their respective processes these samples were analysed using scanning electron microscopy coupled to energy dispersive X-ray spectrometry.

5.3.2.5 Scanning electron microscopy – Energy dispersive x-ray spectrometry (SEM-EDS)

The samples were analysed using a Zeiss EVO scanning electron microscope. Prior to imaging, the samples were mounted on aluminium stubs with double sided carbon tape. The samples were coated with a thin (~10 nm thick) layer of gold, using an Edwards S150A gold sputter coater. A Zeiss 5-diode back scattered electron (BSE) detector (Zeiss NTS BSD) and Zeiss Smart SEM software were used to generate BSE images. The samples were chemically quantified by semi-quantitative energy dispersive x-ray spectrometry (EDS) using an Oxford Instruments® X-Max 20 mm² detector and Oxford Aztec software. Beam conditions during the quantitative analysis and backscattered electron image analysis on the Zeiss EVO were 20 kV accelerating voltage, 8 nA probe current, with a working distance of 8.5 mm and a beam current of 5 nA. The counting time was 10 seconds live-time.

5.4 Results and discussion

Stage I

DSC melting endotherms and crystallization exotherms are illustrated in Figures 5.1a and 5.1b, respectively. Both waxes exhibit melting peak maxima around 75 °C and crystallization peak maxima around 65 °C. The waxes also exhibit bimodal thermal transitions indicating at least two different crystalline domains⁶⁹. The main differences between the thermograms of the two lubricating waxes are the temperature ranges over which the thermal events occur. These thermal events occur over a wider temperature range for the polar wax, resulting in broader melting and crystallization distributions, whereas the nonpolar wax exhibited more homogeneous thermal profiles. This points towards differences in crystallite size distributions and chain length distribution in the two waxes. The nonpolar wax therefore has a more uniform crystal size and chain length distribution compared to that of the polar wax. The latter was further investigated using HT-SEC.

From the HT-SEC data (Table 5.2) it could be concluded that both waxes have similar molecular sizes (hydrodynamic volumes), $M_n \approx 300$ g/mol. However, the molecular weight distribution or molecular weight dispersity (\bar{D}) for the nonpolar wax was noticeably lower compared to the polar counterpart. These results were in good correlation with the conclusions

drawn from the DSC data, with a larger molecular weight dispersity resulting in broader thermal transition distribution for the polar wax.

Chemical composition was investigated by ATR-FTIR. Figure 5.2 shows the ATR-FTIR spectra of both waxes. Both spectra showed distinct methyl and methylene stretching as well as methylene bending vibrations around 2900 cm^{-1} , 1460 cm^{-1} and 720 cm^{-1} , respectively. These vibrational bands are indicative of a predominantly hydrocarbon-based backbone structure. The polar oxidised sample however clearly showed signs of oxygenated moieties evident by the presence of bands at 3480 cm^{-1} , 1720 cm^{-1} and 1170 cm^{-1} attributed to O-H, C=O and C-O stretching vibrations.

Molecular chain linearity of the waxes was probed by ^{13}C -NMR. Spectra are illustrated in Figure 5.3. The spectra of the nonpolar wax were characteristic of a highly linear hydrocarbon with only signals arising from the chain end carbons (1s, 2s, 3s and 4s) and backbone methylene carbons. The extra signals observed in the spectra of the polar wax were due to carbons in the vicinity of oxygenated moieties along the molecular backbone (e.g. peaks at 43 ppm and 24 ppm represents the carbons in α and β position to carbonyl groups). No clear evidence of chain branching was detected. From NMR and FTIR it could be concluded that both wax samples were predominantly linear with the major difference being the presence of polar oxygenate moieties within the polar wax sample.

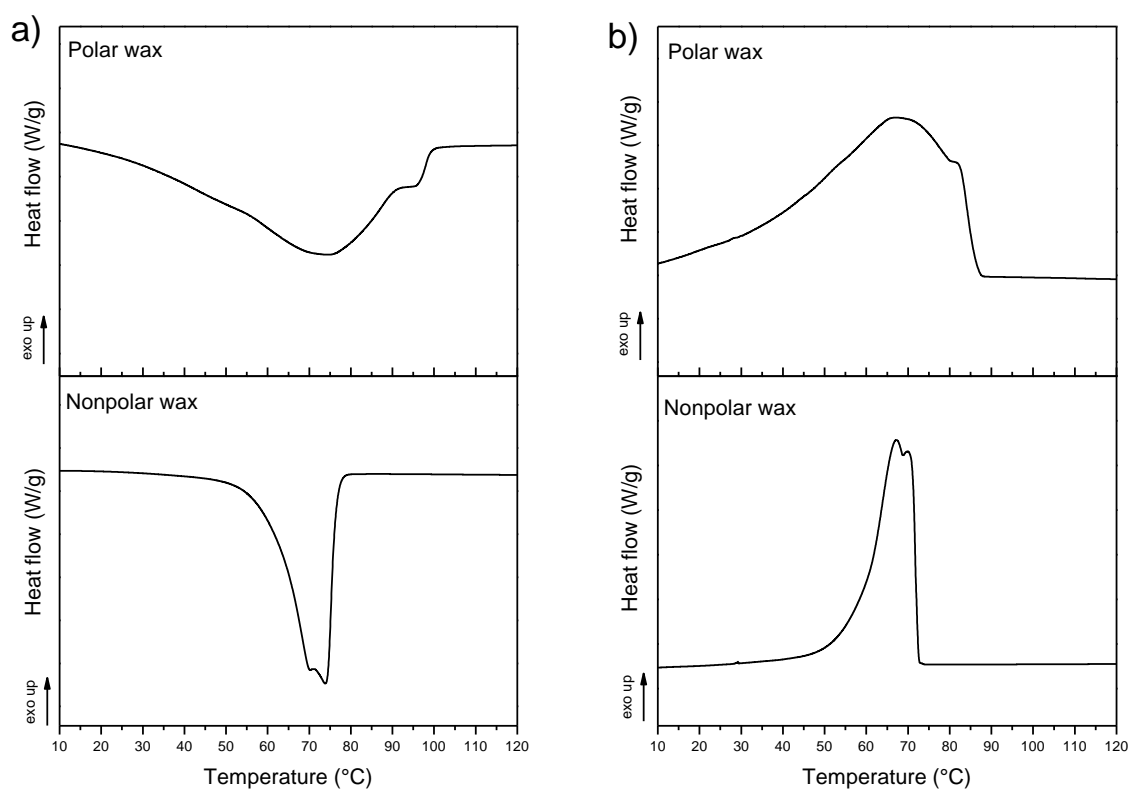


Figure 5.1: DSC thermograms for polar and nonpolar waxes, a) melting endotherms and b) crystallization exotherms

Table 5.2: HT-SEC results for both polar and nonpolar waxes.

Wax type	M_n (g/mol)	M_w (g/mol)	M_p (g/mol)	\bar{D}
Nonpolar wax	298	326	307	1.2
Polar wax	267	442	354	1.7

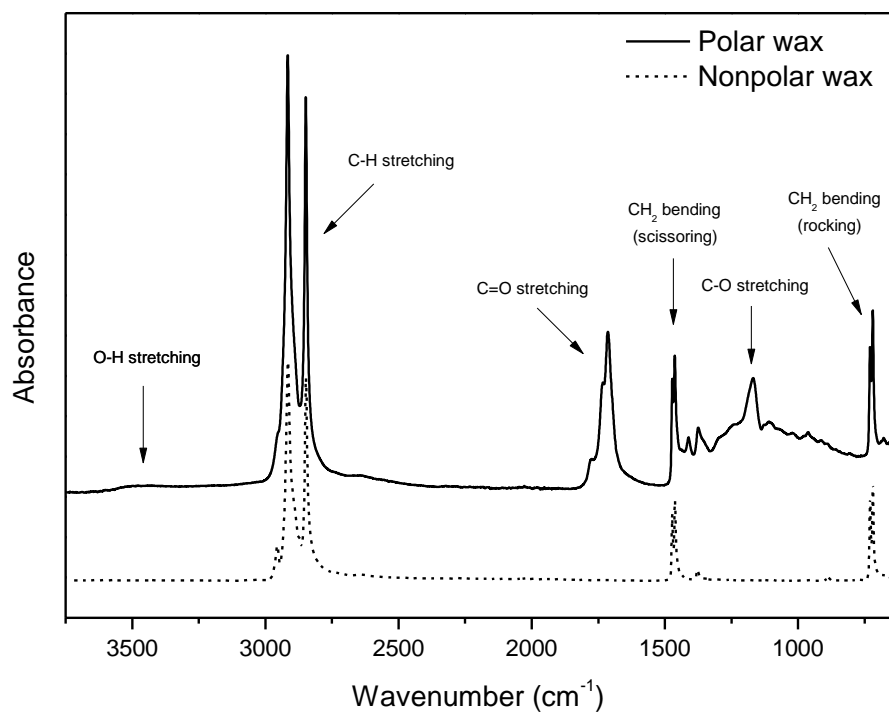


Figure 5.2: ATR-FTIR spectra for both waxes.

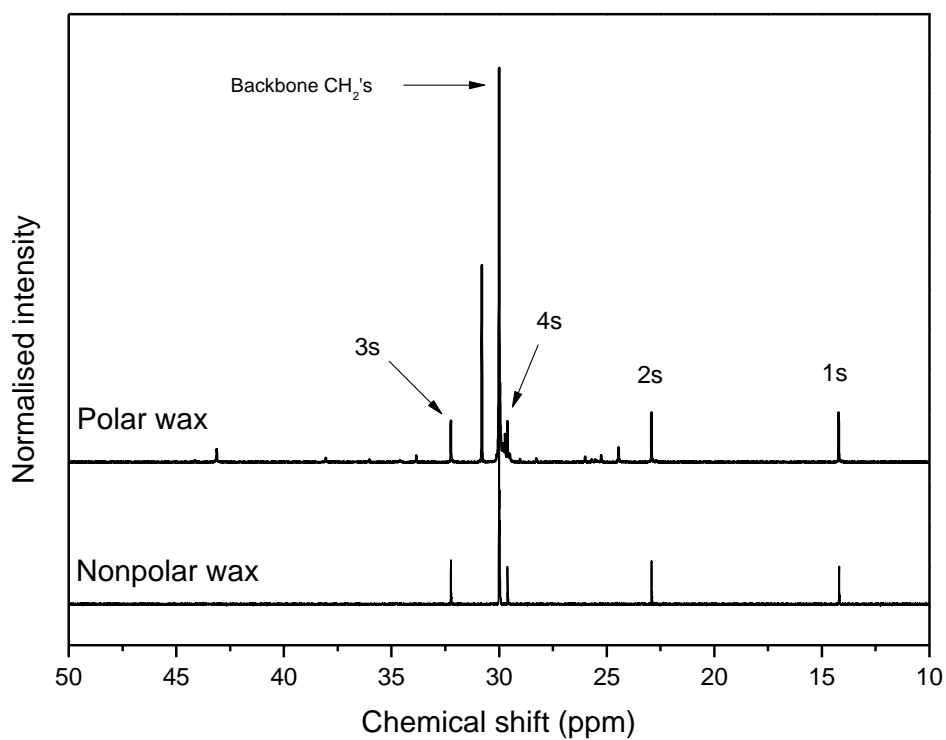


Figure 5.3: ¹³C-NMR spectra for both waxes.

Stage II

Figure 5.4 illustrates the electron images and SEM-EDS signals of the neat PVC particles and blended PVC particles after high-speed melt mixing with internal and external lubricants. The neat PVC particle surface was uneven and showed visible crevices. These crevices contribute to the sample's porosity¹³. A strong uninterrupted chloride (Cl) signal was observed from SEM-SED measurements which corresponds perfectly with the electron image of the neat PVC particle. Addition of the CaSt as internal lubricant clearly decreased the Cl signals implying the partial coverage of the PVC particles with CaSt. It shows crevices being occupied by the internal lubricant which might indicate physical or chemical association between polymer and internal lubricant. This is clearly visible in Figure 5.4b where the blue chloride signals are interrupted. The carbon signals are also intensified due to the presence of the aliphatic carbon chain of the stearate moiety in the CaSt molecule. Furthermore, the presence of the internal lubricant on the PVC was confirmed by the characteristic SEM-EDS oxygen (O) and calcium (Ca) signals. Physical association between lubricant and PVC could possibly occur due to the crevices allowing entrapment of lubricant molecules or possible chemical association could be facilitated through the polar groups of the stearate moiety of the CaSt with the PVC.

Clear differences could be seen with addition of the two respective waxes. The nonpolar wax tended to accumulate within the uneven crevices of the PVC particles, whereas the polar wax tended to cover a larger area across the smooth surface of the particles. This is visually represented by Figure 5.4c where the Cl signals are similar to the neat PVC profile, apart from the darker regions within the crevices due to nonpolar wax accumulations. A more uniform decrease in Cl signals can be seen in Figure 5.4d due covering of the particle by the more polar wax. Higher carbon signal intensities and uniform oxygen signals further confirmed the enhanced coating of the PVC particle with the more polar external lubricant. This could be indicative of a greater affinity of the polar external lubricant for PVC compared to the nonpolar counterpart.

Figures 4e and 4f represents the ternary blends where the PVC was mixed with both the external and internal lubricants. A distinct decrease in Cl signal intensity together with a stronger carbon signal was observed in Figure 5.4e when compared to its binary counterpart in Figure 5.4c. The lubricant coverage is also visible from the electron image. The carbon signals are also strongly associated with the calcium signals, indicating possible interaction between the internal and external lubricants. Homogeneous carbon, oxygen, and calcium signals across the PVC surface point towards the compatibilization of nonpolar external lubricant with the

PVC particles through addition of the internal CaSt lubricant. These enhanced associations are most probably facilitated through nonpolar interactions between the aliphatic stearate tails of CaSt with the aliphatic chains of the nonpolar lubricant, and through polar interactions between the polar stearate heads with the polar PVC surface. Particle coverage for the ternary blend containing nonpolar wax appeared to be greater and more homogeneous compared to the binary PVC/nonpolar wax blend.

Conversely, the particle coverage of the ternary blend containing the polar external lubricant were not as homogeneous across the PVC surface. From the electron image in Figure 5.4f the lubricants appeared to accumulate in the crevices. This phenomenon could be due to competition between the polar groups of the internal lubricant and the polar wax. The internal lubricant did not promote the particle coverage as in the case of the nonpolar ternary blend and was confirmed by the lower signals for C/O/Ca on the particle surfaces. It should be noted at this stage that images 4b and 4f show similar association behaviour towards the PVC particles.

At this point it could be concluded that the internal lubricant facilitated associations and particle coverage when the nonpolar wax was used. However, when the polar wax and internal lubricant was used the particle coverage was somehow hindered. When using the polar lubricant in the absence of the CaSt, a much better uniform particle coverage was observed. The next step was to put the blends through an extrusion cycle and study distribution and migration of these lubricants within the different formulations.

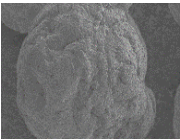
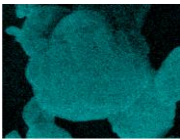
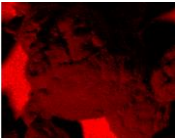
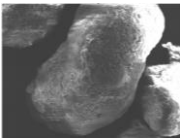
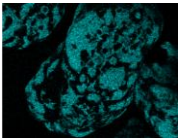
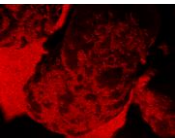
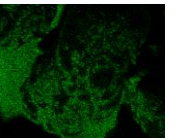
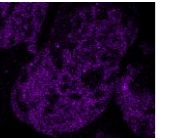
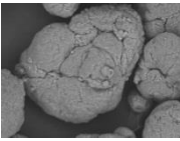
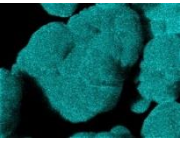
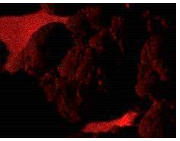
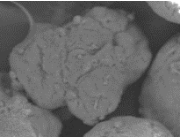
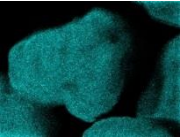

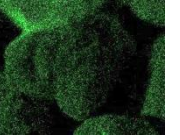
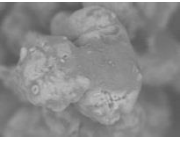
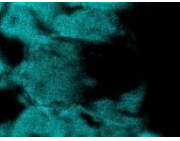
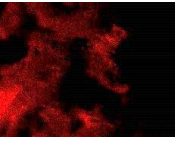

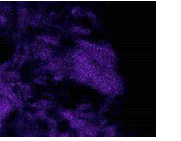
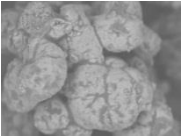
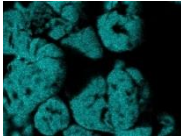
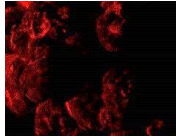

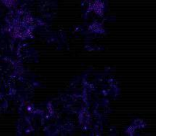
Stage II		Element ($k\alpha$)			
Sample	Electron Image	Cl	C	O	Ca
a					
b					
c					
d					
e					
f					

Figure 5.4: SEM electron images and SEM-EDS elemental signal maps for neat PVC and PVC/Lubricant blends: a) neat PVC; b) PVC/CaSt; c) PVC/nonpolar wax; d) PVC/polar wax; e) PVC/CaSt/nonpolar wax; f) PVC/CaSt/polar wax.

Stage III

The extruded blends (stage III), illustrated by Figure 5.5, showed the development of some interesting morphologies. As the polymer mixture exits the extruder, the sample seems to fold onto itself, resulting in a spiral morphology. This provided an indication of what is really happening within the barrel and has not as yet been reported to a great extent.

Figure 5.5a illustrates dominant Cl signals (EDS signal) due to the neat PVC composition as well as a smooth homogeneous morphology as seen from the electron image. The carbon signal observed towards the middle of the sample arises from residual polyethylene cleaning agent used to purge the barrel in-between batches.

In Figure 5.5b an enhanced spiralling effect can be observed. The morphology was also highly phase separated with distinct polar (Cl) and nonpolar wax (C) regions. This is an indication of poor association between the internal lubricant and the PVC within this binary blend.

Interestingly, when analysing the binary blends which only consist of the external lubricants and PVC (Figures 5c and 5d), homogeneous distributions of the Cl and C signals were observed. In the presence of the oxidised polar lubricant, the oxygen signals were also homogeneously spread throughout the sample. Visual observations from Figures 5b to 5d clearly points towards differences in associations of the external and internal lubricants towards the PVC.

When comparing the two ternary blends in Figures 5e and 5f, completely different morphologies were observed. In the presence of nonpolar wax, a smooth uniform morphology was seen with homogenous distribution of all elemental signals. In this case it is possible that the nonpolar lubricant functioned as a compatibilizer and promoted improved distribution of the internal lubricant and far less phase separation is visible compare to Figure 5.5b. However, in the presence of polar wax, the ternary blend showed a phase separated morphology worse than its binary PVC : CaSt and PVC : polar wax counterparts. This observation was consistent with the differences in coverage of the PVC particles illustrated and discussed previously in Figure 5.4. It can thus be concluded that some degree of competition in the affinity for the PVC exist between the internal lubricant and the polar external lubricant when used together and hence the clear phase separated morphology.

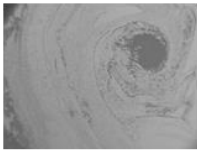
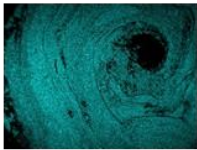
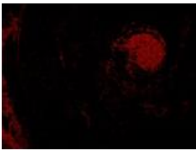

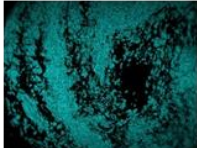
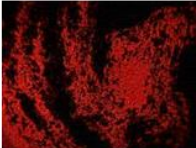


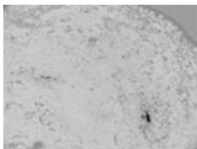
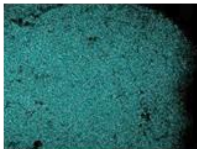
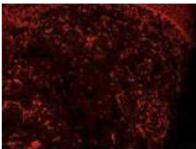
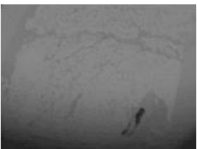
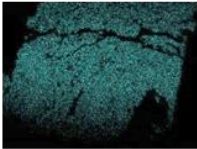
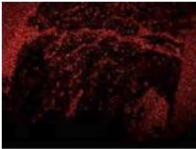


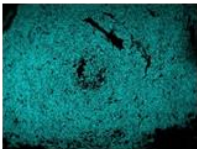
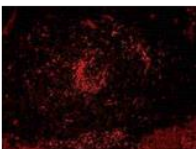
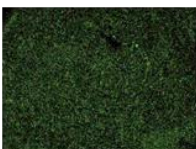

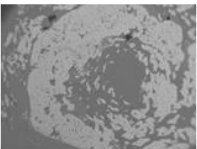
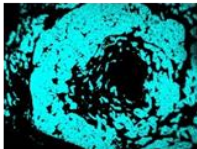
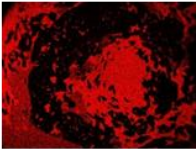


Stage III		Element ($k\alpha$)			
Sample	Electron Image	Cl	C	O	Ca
a					
b					
c					
d					
e					
f					

Figure 5.5: SEM electron images and SEM-EDS elemental signal maps for neat PVC and PVC/Lubricant blends: a) neat PVC; b) PVC/CaSt; c) PVC/nonpolar wax; d) PVC/ polar wax; e) PVC/CaSt/nonpolar wax; f) PVC/CaSt/polar wax.

5.5 Conclusion

Three stages of lubricant migration during PVC processing were investigated. In stage 1 the materials were characterized according to size, chemical composition, chain linearity/branching and thermal behaviour.

Stage 2 was set up to represent the compression section on a typical single screw extruder. Here, insight into how the individual components would associate be it chemically or physically, were obtained. It was seen that nonpolar waxes had no affinity for PVC on its own and oxidised wax exhibited some association. Addition of calcium stearate to the system facilitated association of nonpolar wax to the PVC and less so for polar wax. The polar wax showed a competition effect and seemed to associate with CaSt than PVC.

Stage 3 represented PVC fusion during the metering stage on the extruder. Two phases were identified during this stage namely a polar PVC phase and a nonpolar hydrocarbon phase. Focus was placed on the polar PVC areas and how well the lubricants were dispersed within it. The polar wax had a better dispersion in the PVC matrix compared to the nonpolar wax. Upon addition of CaSt the nonpolar wax had a similar distribution pattern to its binary blend within the PVC matrix. Addition of both CaSt and polar wax to the formulation resulted in a completely phase separated distribution.

In accordance with the surfactant/slip-agent theory, the internal and external lubricants showed a definite affinity for each other. The nonpolar wax did not associate with PVC by itself but only in the presence of CaSt, proving that the nonpolar wax only associates with the nonpolar aliphatic tails of CaSt. No evidence was found to suggest the CaSt creates a boundary layer on the metal–polymer or in between the PVC–wax interface. We suggest further on-line monitoring of the migration event.

Acknowledgments:

The authors would like to thank the staff of the SEM unit at Stellenbosch University central analytical facilities with assistance in conducting SEM-EDS analyses.

This research did not receive any specific grant from funding agencies in the public, commercial, or not-for-profit sectors.

Chapter 6: Method improvement

In the first method that was developed there were two issues regarding sample collection during stage 3. One was the residual cleaning agent which caused contamination resulting in signal interference during SEM-EDS analyses, and the second was that no in-extruder sampling could take place. Further development and method adjustments showed indications that these problems could be overcome using a technique called “screw freezing”.

6.1 Applying the screw freezing technique

Screw freezing is traditionally done by stopping the extruder screw during extrusion. Cold gas is then passed through the instrument to effectively freeze the melting process that is taking place on the screw. The screw is then subsequently pulled out of the extruder barrel with the sample remaining in the screw flights. Due to the poor heat stability properties of PVC, the screw has to be removed from the barrel, while the heating elements are still active, using a hydraulic press. Pulling the screw exposes the development of the polymer melting process during each screw flight. The sample can then be removed from the screw and analysed. Various analytical techniques can be implemented at this stage to investigate the process.

In the case of PVC, screw freezing has been used to study the fusion process using light and fluorescent microscopy. Burgess et al.¹⁷ used this technique to show that fusion occurs along the extruder screw as the PVC particles undergo compacting, elongation, and densification. Figure 6.1 shows the PVC particles undergoing fusion. In the fluorescent images the additives appear as bright spots surrounding the darker PVC particles.

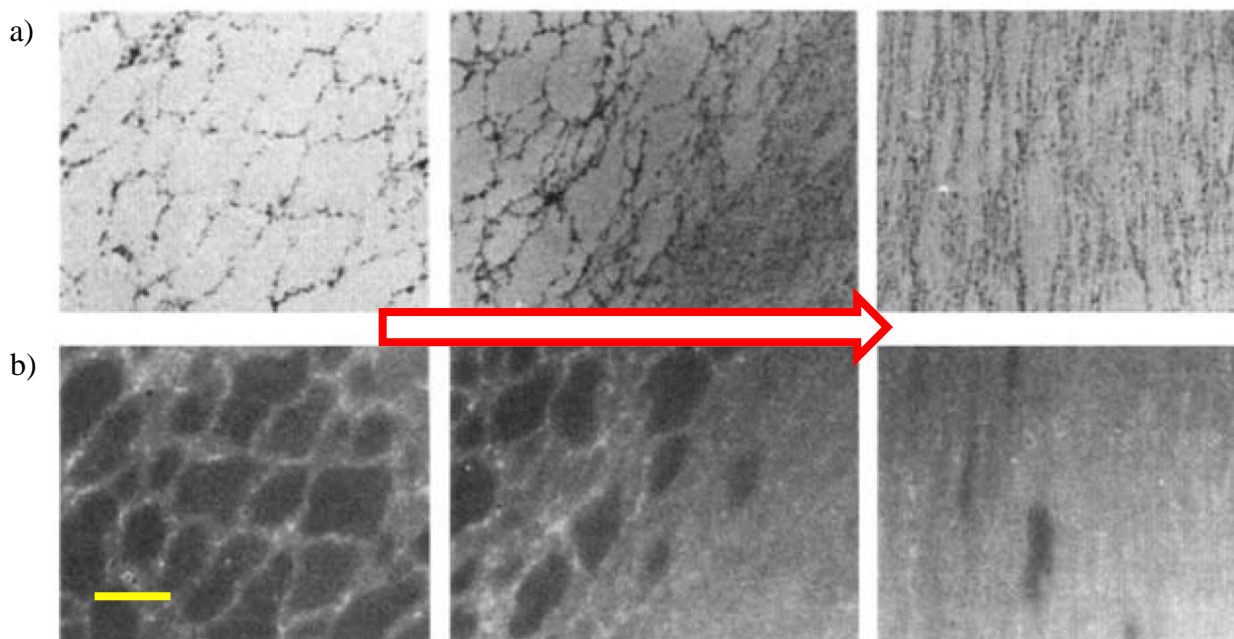


Figure 6.1: Burgess et al. ¹⁷ showing identical fields of view for a) light microscope images, b) fluorescent microscope images along the extruder screw. Arrow = extrusion direction. Scalebar = 100 μm .

In this study the formulations were high speed mixed and extruded in the same way as described in Chapter 4. After some sample exited the die and efficient extrusion had been established, the screw rotation was stopped. The machine was turned off and the screw manually removed. After removing the screw, the sample was allowed to cool down to room temperature. Pulling the screw from the extruder barrel revealed all the material spread along the extruder screw and still occupying the screw flights (Figure 6.2). A screw freezing test method was conducted on a ternary PVC formulation consisting of PVC with J75 wax (10 phr) and CaSt (5 phr).

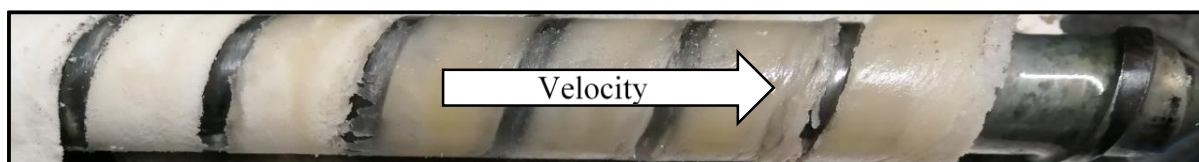
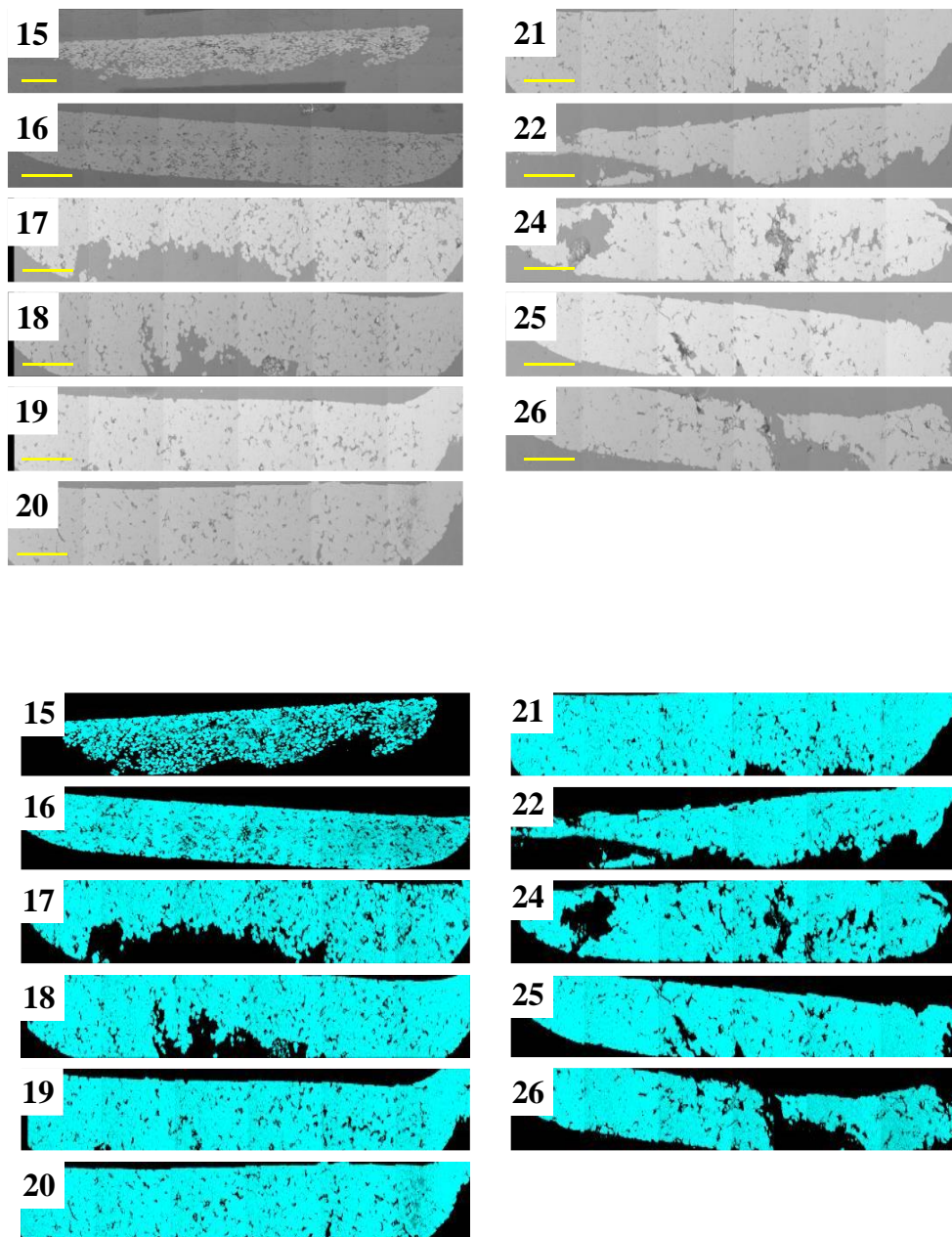


Figure 6.2: Section of a pulled screw filled with PVC formulation. Polymer flow is shown in the direction of the velocity arrow.

Sample within the screw flights were cut off and removed. A side view of these cut-offs was analysed using SEM-EDS (Figure 6.3). This allowed for an effective on-line measurement of how the components interacted during extrusion. Figure 6.2 shows SEM-EDS images of the J75 ternary blend screw freeze experiment. Samples were numbered from flight 15 to 26. From the blue chloride signal, progression of the fusion process could be seen. In flight 15, individual PVC particles were observed. From flight 16-26, a progressively denser blue signal became apparent. It indicates the disappearance of individual particles accompanied by growing regions of fused PVC. Flight 26 had the highest amount of fused PVC and was therefore used as reference flight for stage 3 during screw freezing experiments. Carbon signals could also be seen randomly dispersed throughout each flight. Figure 6.4 shows electron images of stage 2 for the extrusion experiment (Figure 6.4a) and for the screw freezing method (Figure 6.4b). Wax dispersion (dark grey) from high-speed melt mixed blends during stage 2 of the extrusion experiment exhibited scatter patterns which were conclusive with scatter patterns seen from observations during stage 2 of the screw freezing experiment. It was therefore concluded that the stage 2 experiment was efficient in representing what occurred in the barrel. Calcium signal was more difficult to observe but did however coincide with the wax signal as could be seen from flight 24. The entire flight did not fuse, and the decision was made to alter the blend ratio of PVC : Wax : CaSt to 100 : 5 : 5 phr. This new formulation ratio induced sufficient fusion and was used throughout the rest of the study and the screw freezing method was expanded to the complete set of waxes. It was however found that higher melting waxes (waxes that melted above the T_g of PVC) from section 1 did not fuse. It is also known that higher melting waxes have substantially longer fusion times. It was decided that long fusion times were not practically viable for our setup during the study. Higher melting waxes were therefore excluded from the experiments that followed.



Note: Figure 6.3 caption on next page.

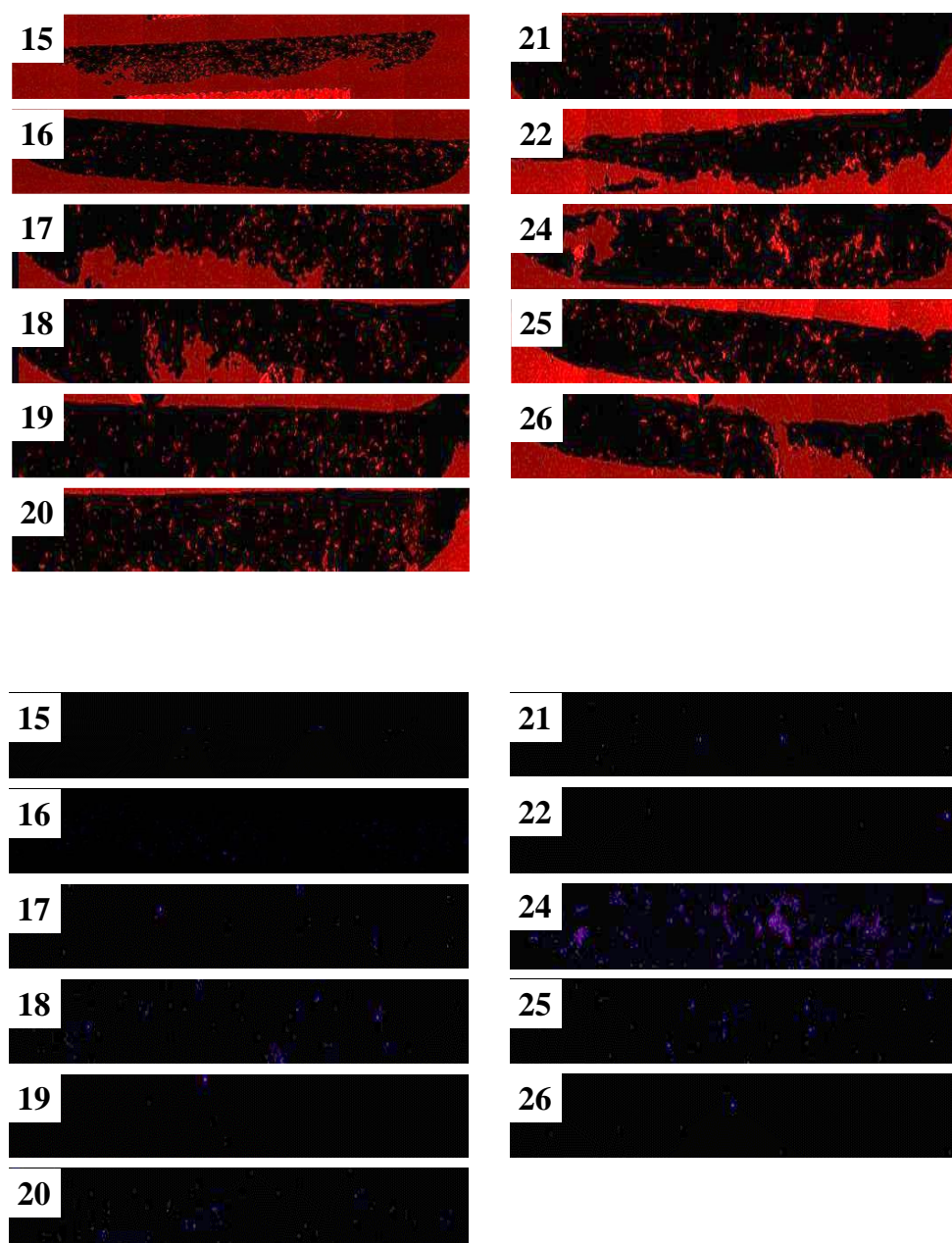


Figure 6.3: SEM-EDS images of screw freezing technique. Sample = PVC : CaSt : J75 (100 : 5 : 10). Electron image = Grey; Chloride = Blue; Carbon = red. Calcium = purple. Scalebar = 2 mm.

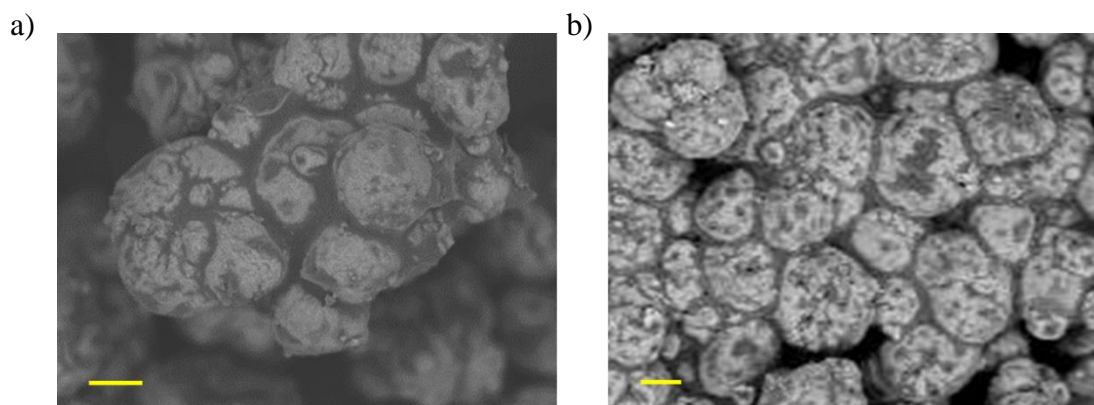


Figure 6.4: Electron images of PVC particles during stage 2 for the a) extrusion method and b) screw freezing method. PVC = light grey; Wax = dark grey. Scalebar = 20 μm .

Stage 3 could now be characterized in an on-line manner. In addition to gaining an on-line technique, contributions of the cleaning agent were no longer visible as the screw could now be manually cleaned by hand after every run.

6.2 Selection of Wax set 2

From the manuscript (Chapter 5) various trends could be established. These trends mostly related towards differences in polar and nonpolar waxes. A second set of samples were selected to further investigate the effects of different chemical composition and microstructures on wax migration. Two sets of waxes with different polarities and microstructures were chosen. A set of nonpolar as well as a set of polar waxes were selected and subjected to the new modified screw freezing method. In the nonpolar set, two linear waxes were selected with the one being a fully refined crude-oil derived paraffin (FRP) wax and the second was obtained from the Fischer-Tropsch (FT) process. A crude-oil derived microcrystalline wax (Microwax) with methyl chain branching and an unsaturated polyalpha olefin (PAO) wax was also included in the nonpolar hydrocarbon wax set. The polar wax category consisted of two polyethylene waxes, one being an oxidized high-density polyethylene wax and the other a low-density polyethylene wax. Two FT waxes with different degrees of oxidation were also included. All waxes are listed in Table 6.1.

Table 6.1: Classification of waxes used.

	Nonpolar		Polar
Linear	FRP 58/60 (FRP)	Oxidized PE	Honeywell AC316A (oHDPE)
	J75 (FT)		Honeywell AC629A (oLDPE)
Branched	W445 (Microwax)	Oxidized FT	Sasol A28 (oFT28)
Unsaturated	PAO C30+ (PAO)		Ceranol 40L90 (oFT40)

6.3 Results and discussion of stage 1 (Wax set 2)

6.3.1 HT-SEC

Wax molecular weights and the heterogeneity thereof were determined by HT-SEC. Nonpolar waxes (Figure 6.5a) were all similar in molecular weight and molecular weight distribution with the two linear waxes (FRP and FT) showing slightly smaller averages compared to Microwax and PAO. Chromatograms of the polar waxes were spread over a wider molecular size range (Log (Mw)) with the two polyethylene waxes showing much broader profiles compared to the oxidized FT counterparts indicating the higher molecular weight heterogeneity within the PE waxes. Overall, the nonpolar waxes had lower polydispersities than the polar waxes and hence were more homogeneous with respect to molecular weight.

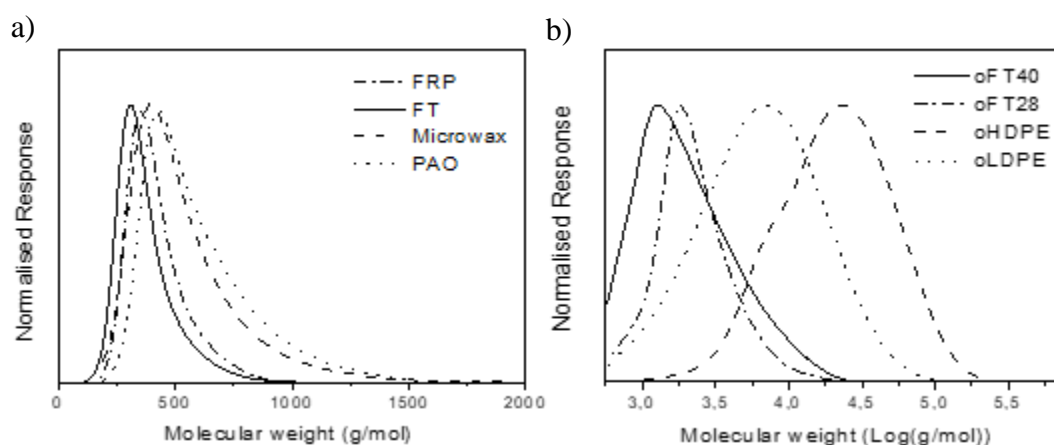


Figure 6.5: HT-SEC results of a) nonpolar and b) polar waxes.

6.3.2 Attenuated total reflectance – Fourier transform infrared spectroscopy (ATR-FTIR)

Chemical composition of the waxes was studied by FTIR. Spectra are shown in Figure 6.6. Nonpolar waxes were similar in chemical nature and showed profiles evident of hydrocarbon backbones. FRP and FT had a large methyl peak at 2959 cm^{-1} (Figure 6.6a). From the HT-SEC data it was seen that FRP and FT had the lowest molecular weights, and therefore their methyl to methylene signal ratio was higher (more chain ends per sample). Vibrational contributions of the chain ends are larger for shorter molecular backbones and hence the larger methyl bands for FRP and FT. PAO also showed unsaturation around the 1640 cm^{-1} area, indicative of alkene moieties. Polar waxes also exhibited similar spectral profiles within their group (Figure 6.6b) with the presence of carbonyl bands differentiating them from the nonpolar wax spectra. In the case of oxidized waxes, the carbonyl stretching region around $1776 - 1716\text{ cm}^{-1}$ was of main concern (Figure 6.6c). This region consists of carbonyls from chemical groups such as carboxylic acids (1715 cm^{-1}), esters (1734 cm^{-1}) and lactones (1776 cm^{-1}). When comparing the signal height ratios of carboxylic acid to methylene (2920 cm^{-1}) bands, a fairly good correlation was obtained to the acid number reported by the wax suppliers. FT40 had the strongest carbonyl signal at about 39% of its methylene peak absorbance and also had the highest acid number of 40 mg KOH/g. oFT28 had an acid number of 28 mg KOH/g and resulted in the second strongest carboxylic acid signal of about 25% of the signal intensity of its methylene band. oHDPE and oLDPE waxes had acid numbers of 16 mg KOH/g and 15 mg KOH/g and percentage absorbance values of ± 11 and 12% respectively.

6.3.3 Differential scanning calorimetry (DSC)

DSC thermograms of the waxes are shown in Figure 6.7 with the glass transition temperature (T_g) of PVC indicated by the dotted line at $85\text{ }^{\circ}\text{C}$. All the nonpolar waxes (Figure 6.7a) melted below the T_g of PVC. This was an essential observation as it was observed that the higher melting nonpolar waxes (as mentioned earlier) significantly delayed fusion. Although the polar waxes (Figure 6.7b) all had higher melting temperatures when compared to the nonpolar waxes, efficient fusion could still be achieved as will be discussed later. Nonpolar waxes also showed sharper endotherms in general except for the branched Microwax which had a broad melting endotherm. Overall, the polar waxes had higher melting temperatures mainly due to the larger molecular weight as seen previously by HT-SEC. Polar waxes also had broad melting endotherms correlating to the broad molecular weight distributions, except for oHDPE which

showed a relatively sharp peak. oHDPE was the highest melting wax as was expected from a HDPE derived wax.

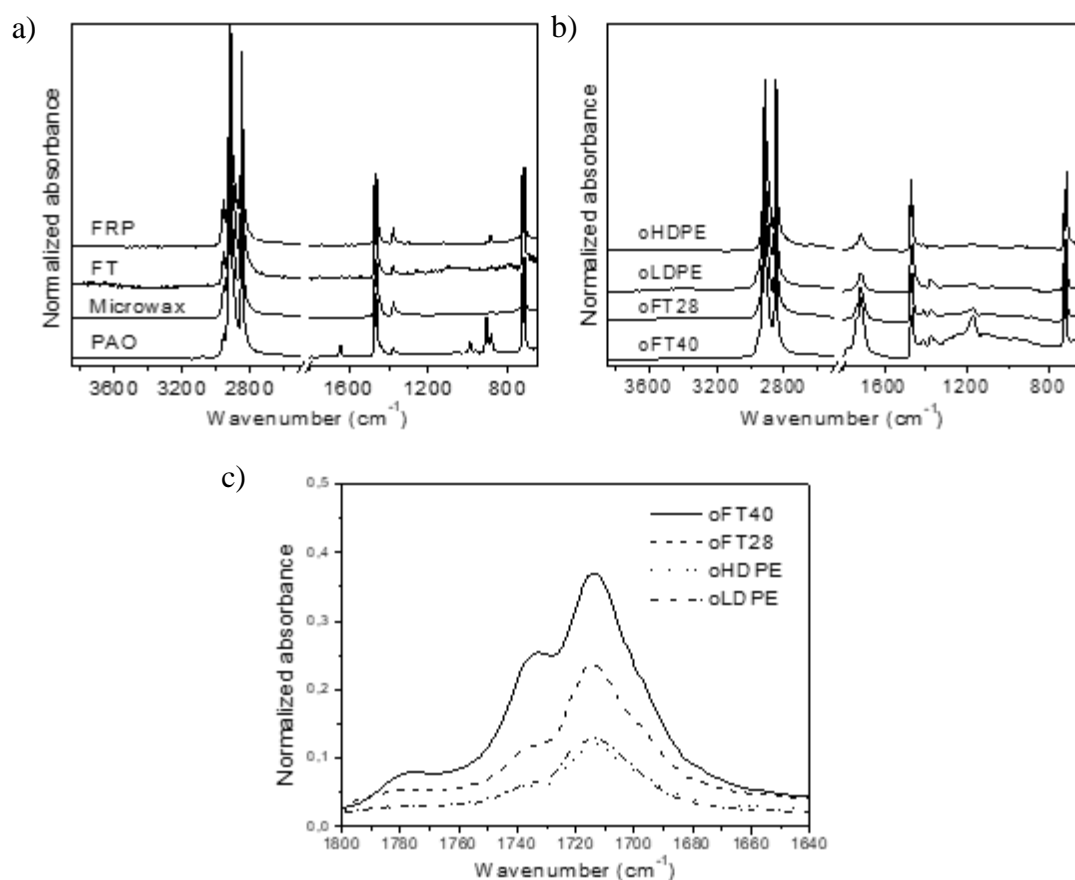


Figure 6.6: ATR-FTIR spectra of a) nonpolar; b) polar and c) carbonyl absorbance of polar waxes.

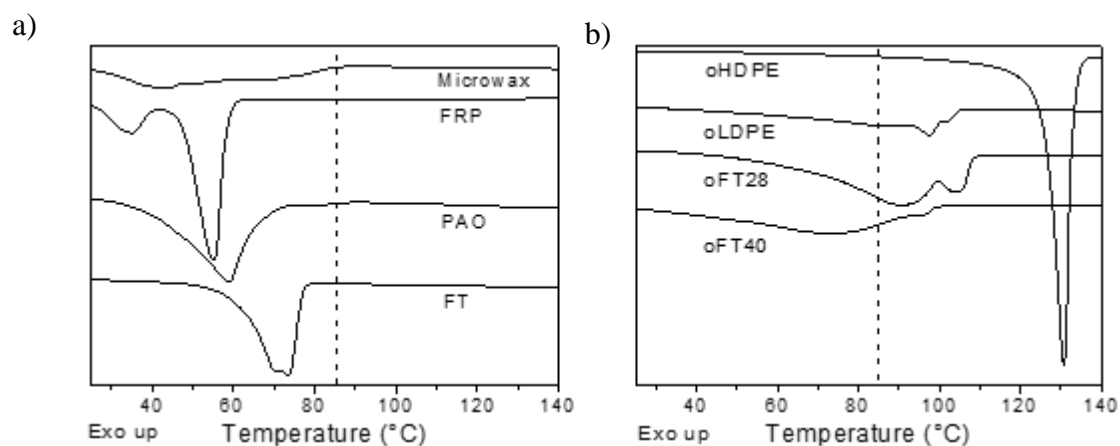


Figure 6.7: DSC thermograms of a) nonpolar and b) polar waxes.

6.3.4 ^{13}C Nuclear magnetic resonance (^{13}C -NMR)

Molecular chain linearity was evaluated using ^{13}C -NMR spectroscopy. FRP and FT exhibited a high degree of linearity as a strong backbone methylene signal (30 ppm) together with chain-end carbon signals 1S, 2S, 3S and 4S at respectively 14.2, 22.9, 32.2 and 29.6 ppm, could be observed. Ratios in signal intensities of chain-end carbons to backbone carbon were similar within the nonpolar wax set indicating that the average molecular chain lengths were within similar ranges, correlating to HT-SEC data. Besides these characteristic linear hydrocarbon wax signals, Microwax and PAO exhibited some additional carbon signals. These signals arose from chain irregularities such as methyl branching and alkene olefin unsaturation respectively (Figure 6.8a). oHDPE was an exceptionally large molecule (Figure 6.5b) which is why the 1-4s carbon signals were very small. The 1-4s signals became more visible with the smaller oLDPE wax. Additionally, oLDPE also exhibited some degree of branching. oFT40 also showed lower intensity 1-4s signals as it was slightly smaller than oFT28 (Figure 6.4b). In comparing the two oxidized FT waxes, oFT40 showed a higher degree of branching when compared to oFT28 wax. This could be attributed to the presence of more oxygenate moieties in oFT40 as seen in Figure 6.6c.

6.4 Results and discussion of stage 2 (Wax set 2)

Binary and ternary blends of all the waxes were prepared by high-speed mixing at an elevated temperature (above the melting point of the waxes), as discussed previously in the method development chapter. Binary blend ratios of PVC : wax was 100 : 5 phr, whereas ternary blends ratios of PVC : CaSt : wax was 100 : 5 : 5 phr. Figure 6.9 shows SEM-EDS results of binary blends prepared with nonpolar waxes. It could be seen from these images that there were no inherent associations of wax to the PVC. The absence of definite red carbon signals on the surface of the PVC particles indicates that the nonpolar waxes had little to no affinity for the PVC particles. Sharp red signals observed in between particles were because of the carbon tape used as adhesive substrate during SEM analyses.

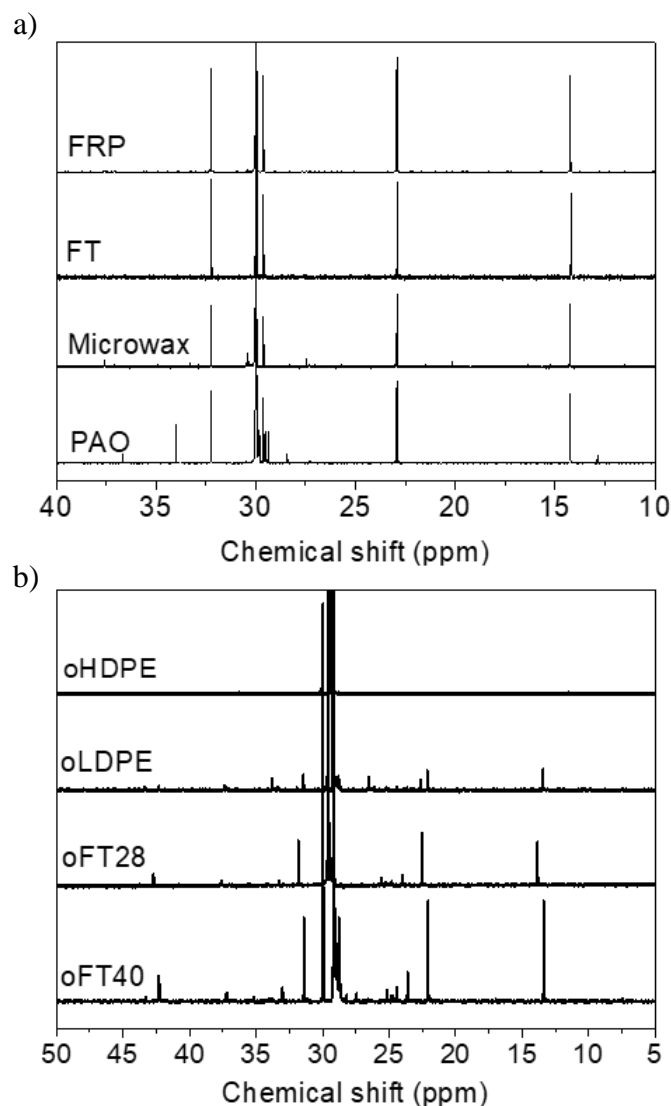


Figure 6.8: Solution ^{13}C -NMR Spectra of a) nonpolar waxes and b) polar waxes.

Figure 6.10 shows images of the ternary blends of the nonpolar waxes. A clear increase in particle coverage could be seen after the addition of CaSt. Red carbon signals could be observed on PVC particles indicating that the CaSt facilitated the affinity of the nonpolar waxes towards the PVC. Overlapping red wax carbon signals and purple CaSt calcium signals imply that the internal and external lubricants were in proximity of each other. CaSt could potentially function as a compatibilizer between the polar PVC particle and the nonpolar waxes. No distinct differences could be observed in the degree of particle coverage between the various nonpolar wax blends.

Interestingly, noticeable traces of wax were present on the PVC particle surfaces when analysing the binary blends formulated with the polar lubricants. Images are shown in Figure 6.11 and the red signals indicate larger areas of particle coverage and hence higher affinity of the polar waxes towards PVC, as compared to the nonpolar counterparts. More particle coverage was seen for the oHDPE wax than for oLDPE or the oxidized FT waxes which was an interesting result as oHDPE was the largest molecule with the lowest degree of oxidation. This might have been an indication of molecular weight playing a greater role in facilitating association rather than the presence of oxygenate moieties. Ternary blends (Figure 6.12) show an increase in association after addition of CaSt throughout the polar wax set. It was clear by the increased carbon signal intensities. Like for the nonpolar set, wax, and CaSt signals overlapped. Thus, from stage 2 it was concluded that CaSt facilitated associations between wax and PVC to a similar extent regardless of the chemical nature or microstructure of the wax.

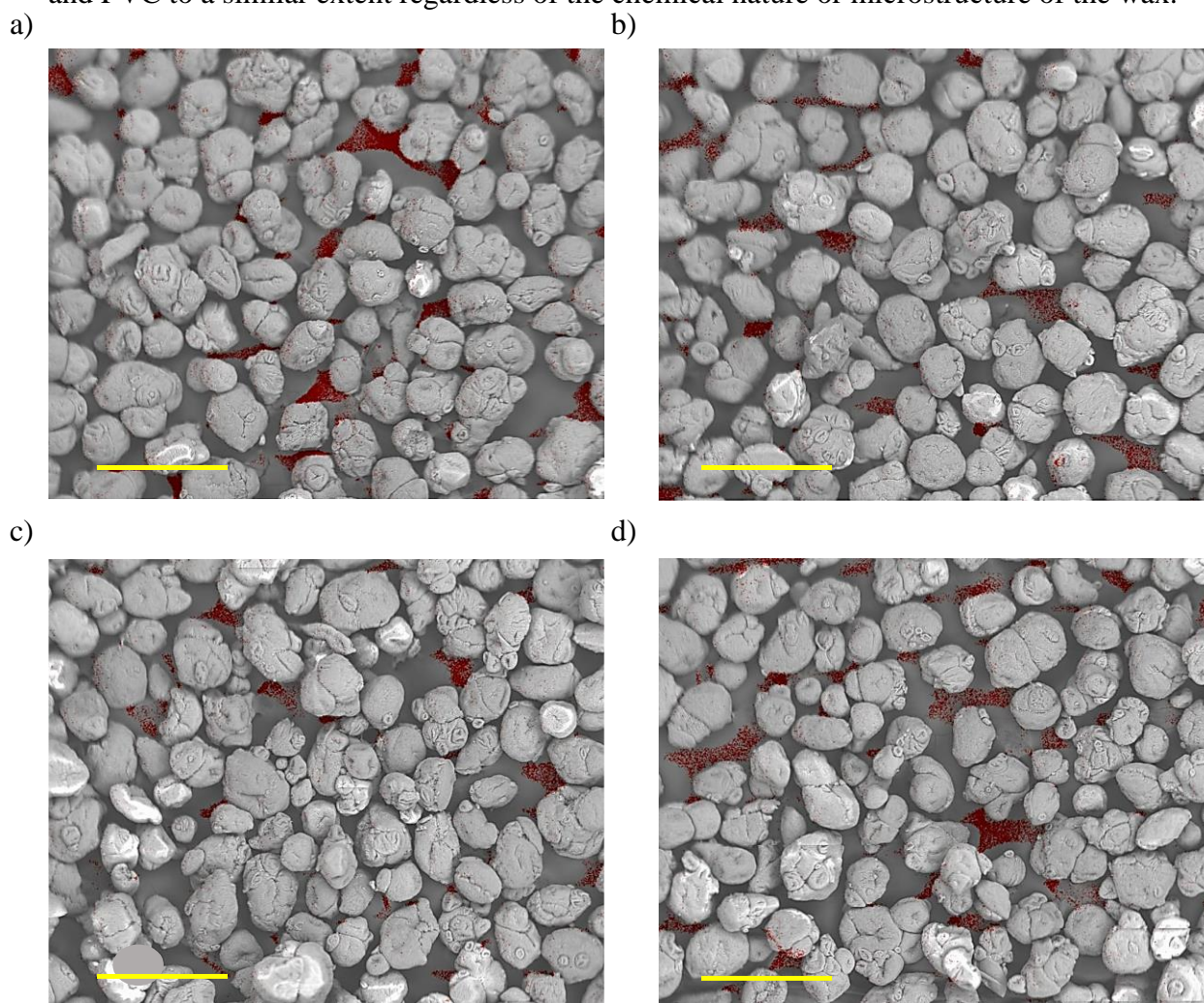


Figure 6.9: SEM-EDS images of binary blends of nonpolar waxes. a) FRP; b) FT; c) Microwax; d) PAO. Carbon = red. Scalebar = 400 μm .

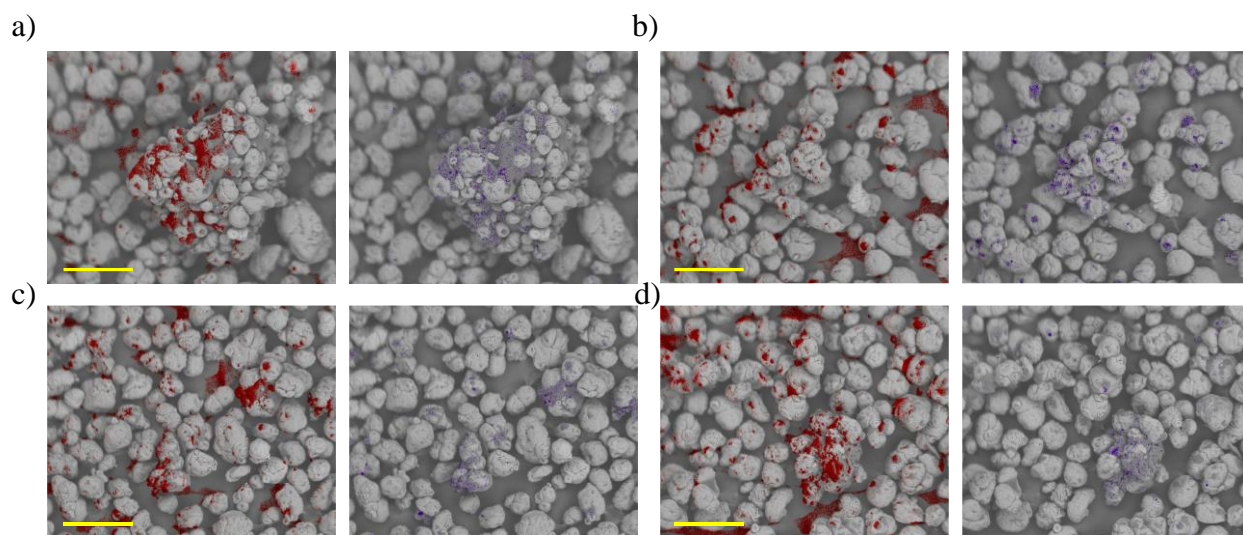


Figure 6.10: SEM-EDS images of ternary blends of nonpolar waxes. a) FRP; b) FT; c) Microwax; d) PAO. Carbon = red. Calcium = purple. Scalebar = 400 μm

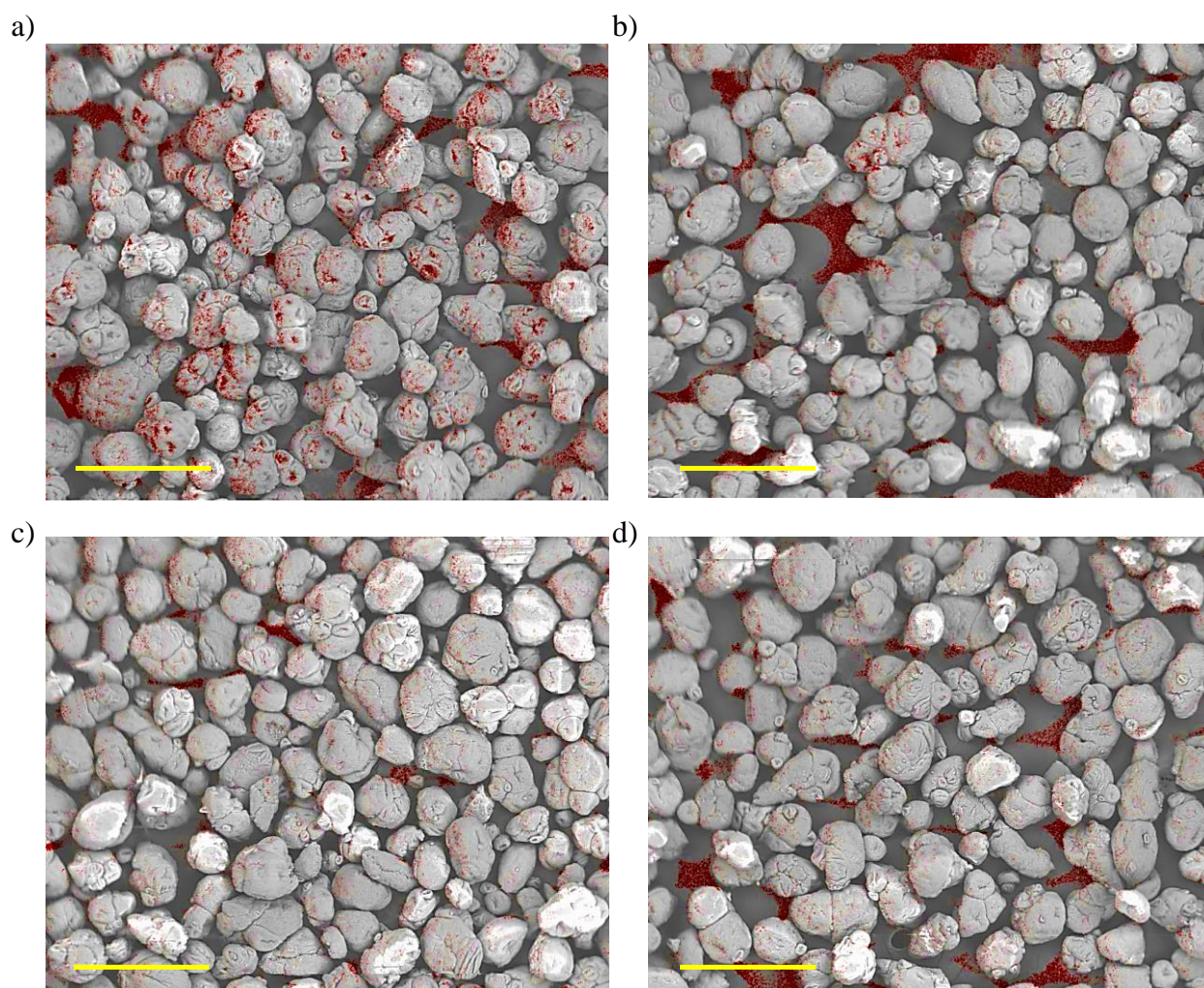


Figure 6.11: SEM-EDS images of binary blends of polar waxes. a) oHDPE; b) oLDPE; c) oFT28; d) oFT40. Carbon = red. Scalebar = 400 μm .

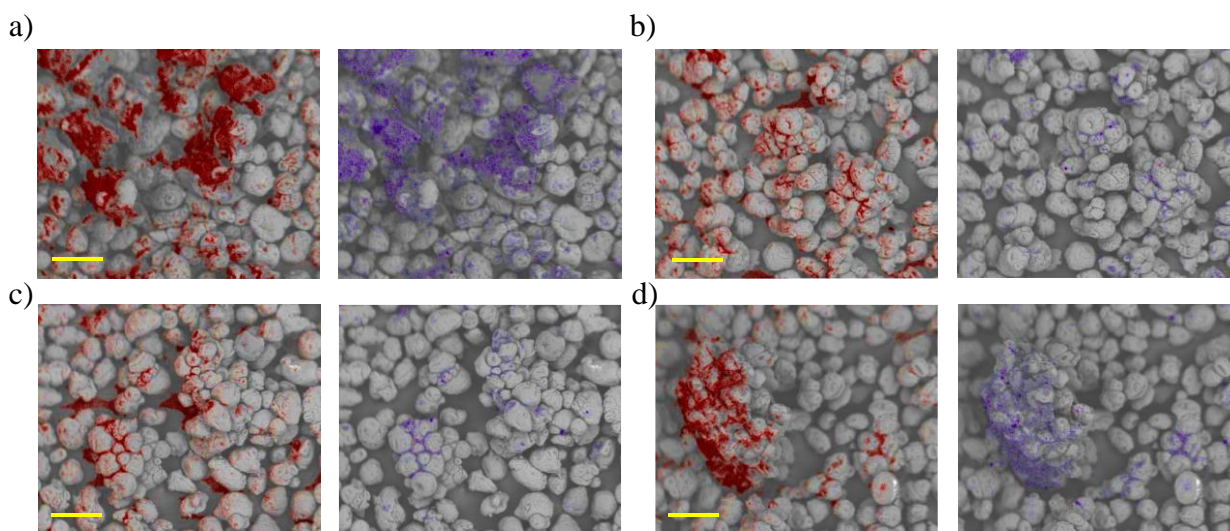


Figure 6.12: SEM-EDS images of ternary blends of polar waxes. a) oHDPE; b) oLDPE; c) Sasol A28; d) Ceranox 40L90. Carbon = red. Calcium = purple. Scalebar = 400 μ m.

6.5 Results and discussion of stage 3 (Wax set 2)

Figure 6.13 illustrates the cross-sectioned images of binary and ternary blended material retrieved from flight 26 of the extruder screw for the nonpolar waxes. SEM-EDS results of the binary blends are shown on the left with a carbon and chloride signal overlay map (Figures 6.13a-d). On the right the corresponding ternary blends are shown with an overlay of chloride and calcium signal (Figures 6.13e-h). Carbon signal was not shown for the ternary blends as it could be confused with carbon signal from the epoxy-based resin in which samples were imbedded. As it was shown during stage 2 that wax and CaSt associates, only the calcium signal was shown as a representative for both wax and CaSt components. An example of overlapping calcium and carbon signal is shown in Figure 6.14. Due to the solid blue signal throughout the sample set and a non-granular appearance it was observed that complete fusion was achieved at this screw flight along the extrusion barrel for every extrusion. Throughout the binary blends there was no interference with the chloride signals. It was therefore concluded that all the wax most likely migrated outward towards the extruder's metal interface. Ternary blends however showed some interesting results. Within the FRP and PAO blends evidence of some wax was present in the fused sample and resulted in some interference of the blue chloride regions. Calcium signals appeared to be concentrated more towards the metal interface than towards the centre of the PVC matrix, as seen by the darker spots in Figure 6.13e and 6.13h. FT and Microwax showed very little to no wax inclusion and was therefore deemed to have completely migrated outwards.

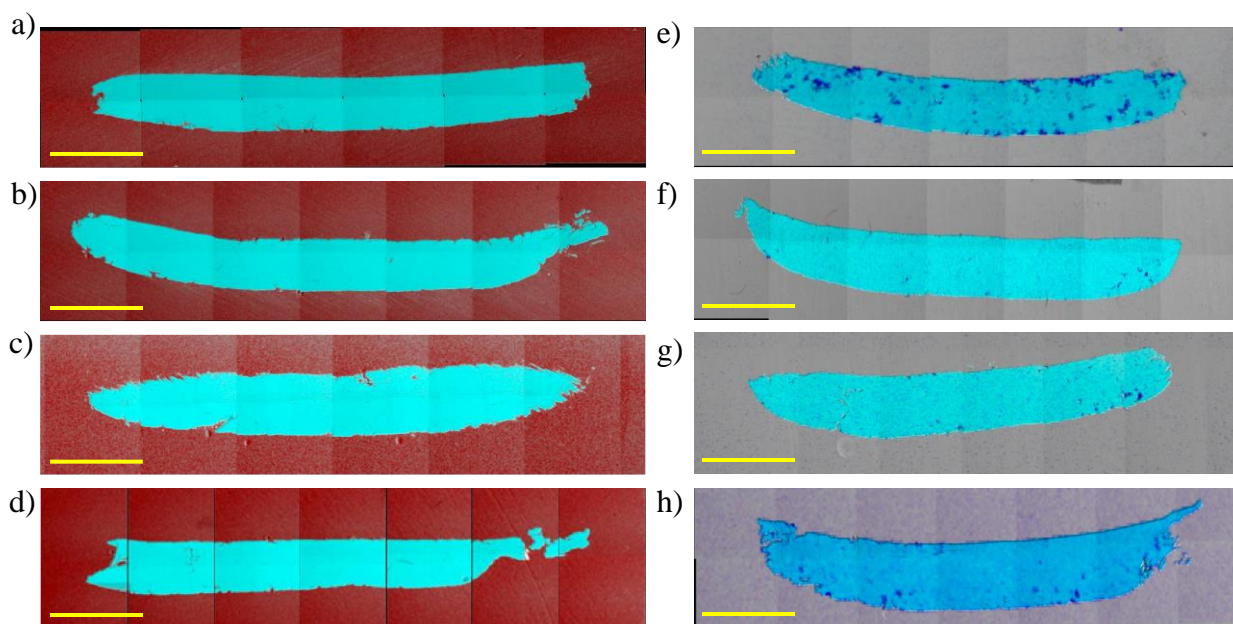


Figure 6.13: SEM-EDS images of binary blends (left) of nonpolar waxes. a) FRP; b) FT; c) Microwax; d) PAO and ternary blends (right) of nonpolar waxes e) FRP; f) FT; g) Microwax; h) PAO. Chloride = blue. Carbon = red. Calcium = purple. Scalebar = 2 mm.



Figure 6.14: FRP ternary blend showing calcium and carbon signal association.

Figure 6.15 showed polar wax extrusions and was constructed in the same manner as Figure 6.13 was constructed for the nonpolar waxes. Complete fusion was achieved throughout the whole sample set of the polar waxes as well. This was significant for the polar waxes as this was not achieved for the nonpolar waxes with the same melting behaviour (above the T_g of PVC). Binary blends of samples a and d showed minor wax inclusion within the PVC matrix. This was interesting as a higher degree of association between these waxes and PVC was also seen with the binary blends during stage 2. Sample b however also showed some association during stage 2 but did not show any inclusion during stage 3. For the ternary blends only sample b showed some wax inclusion.

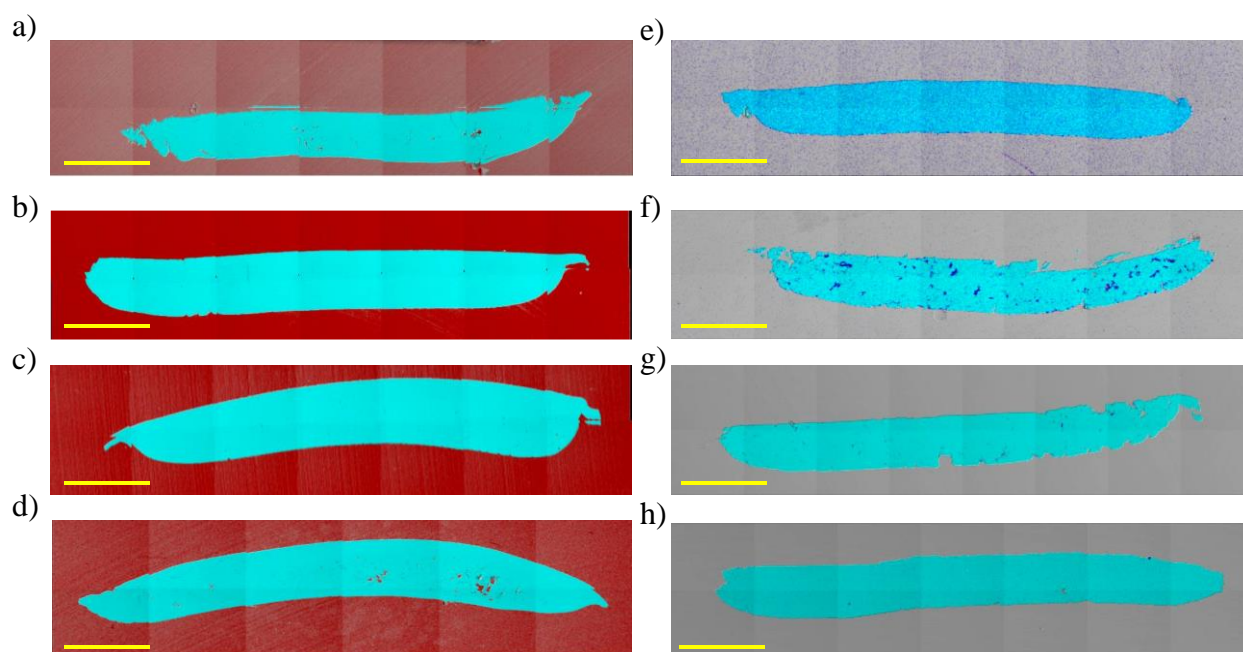


Figure 6.15: SEM-EDS images of binary blends (left) of polar waxes a) oHDPE; b) oLDPE; c) oFT28; d) oFT40 and ternary blends (right) of polar waxes e) oHDPE; f) oLDPE; g) oFT28; h) oFT40. Carbon = red. Calcium = purple. Scalebar = 2 mm.

6.6 Concluding remarks to the method improvement chapter

No relationship between delayed migration during stage 3 could be drawn to any other results of stages 1 and 2. One question which arose was whether the polarity or molecular weight facilitated association in binary blends as seen in Figure 6.11. It was decided that the waxes chosen were too varied in their properties from stage 1. This resulted in too many variables which made drawing any conclusions for results during stages 2 or 3 difficult. It was therefore decided to control some of these variables by synthesizing a new set of waxes to be subjected to the test method.

Chapter 7: Method refinement and commercial testing

In the research to date, a specialized set of waxes were investigated in binary and ternary blends containing wax, CaSt and PVC. The waxes varied in both microstructure and chemical composition. Some conclusions could be drawn from this work; there was an observable effect of CaSt addition to a formulation, for example. Another conclusion that could be drawn was that the incorporation of high melting polar waxes in PVC blends resulted in fusion whereas no fusion was obtained when using the high melting nonpolar waxes. For both sets of waxes (polar and non-polar) it was difficult to observe any trends in binary or ternary blends during stages 2 or 3. This was due to the waxes being too varied in melting range, size distribution, chemical nature, and chain linearity. In an attempt to narrow down on these variables in stage 1 it was decided to synthesize a new set of waxes with varying degrees of polarity for a more comprehensive analysis.

7.1 Oxidized wax synthesis (Wax set 3)

From the preceding chapters there were little effects observed when analysing the nonpolar waxes. It was therefore decided to synthesize a set of more well-defined polar waxes as polarity seemed to exhibit some interesting results. This was done by the controlled oxidation of two known nonpolar waxes. Two linear FT waxes, J75 and J100, of which the analysis results are presented in a previous chapter, were chosen for this investigation. These two waxes are obtained from the same FTS master batch. They were separated from the same master batch through distillation based on their melting behaviour. J100 was a higher melting wax ($M_p \approx 100\text{ }^{\circ}\text{C}$) and J75 was a lower melting wax ($M_p \approx 75\text{ }^{\circ}\text{C}$). In this experiment, both these neat waxes were subjected to ozonolysis which resulted in two sets of waxes with varying degrees of oxidation (Table 7.1).

Ozonolysis was done by bubbling ozone (O_3) gas through the molten wax under constant stirring. Ozone gas was produced by feeding oxygen from a cylinder into an electric discharge ozoniser (Fischer Scientific, Meckenheim Germany). Ozone was introduced at a rate of 6 g/h and was monitored by keeping the O_2 flow (50 L/h) and electrical current (1 A) constant. J75 and J100 were heated to $120\text{ }^{\circ}\text{C}$ and $140\text{ }^{\circ}\text{C}$, respectively, to make sure that the waxes remain in the molten state throughout the oxidation process. The degree of ozonolysis was monitored off-line using attenuated total reflectance Fourier transform infrared (ATR-FTIR) spectroscopy. A commercial oxidized wax, Ceranox 40L90, with an acid number of 40 mg KOH/g exhibited an infrared absorbance in the carboxylic acid signal range at 1715 cm^{-1} . This

signal intensity was at about 40% of the methylene signal at 2920 cm^{-1} . This signal ratio was therefore used to represent the qualitative degree of oxidation.

Comparing the ATR-FTIR spectrum of a sample of oxidized J75 wax (oJ75_40) to that of Ceranox 40L90, showed good agreement (Figure 7.1a). Sample oJ75_40, however, did not exhibit a significant hydroxyl absorbance (Figure 7.1b). Figure 7.1c shows the expanded carbonyl absorbance range. Multiple carbonyl peak splitting could be observed due possibly contributed by different carbonyl species. The main carbonyl peak at 1716 cm^{-1} had the same relative intensity for both waxes. The other two observed shoulders in the carbonyl range were observed at 1734 cm^{-1} and 1776 cm^{-1} , respectively. For both these signals, sample oJ75_40 exhibited a slightly lower signal intensity compared to the Ceranox 40L90 sample, indicating that resultant oxygenate species may differ depending on the method of oxidation and suggest that care should be taking when classifying and comparing oxidized waxes solely on acid numbers. It was however unknown which commercial method was used in synthesizing Ceranox 40L90. Ozonolysis of J100 yielded similar results which are shown in Figure 7.2.

Figure 7.3 shows the progression of oxidation for J75 and J100. In both cases the carbonyl peaks increased with oxidation time. Both samples that were oxidized to 40% showed a new peak at 1167 cm^{-1} , which was associated with C-O stretching⁵⁶. It was decided to conduct further investigation into which oxygen moieties were developing during the ozonolysis reactions.

Table 7.1: Oxidised waxes from ozonolysis procedure.

FT wax	Code	O ₃ (wt. %) ⁷	Oxidation (mol %) ⁸
J75	oJ75_10	24	10
	oJ75_40	92	40
J100	oJ100_10	15	10
	oJ100_40	90	40

⁷ Percentages were calculated as amount of Ozone (g) / total amount of wax (g).

⁸ Percentages were calculated as maximum carbonyl absorbance (1715 cm^{-1}) / maximum methylene absorbance (2920 cm^{-1}).

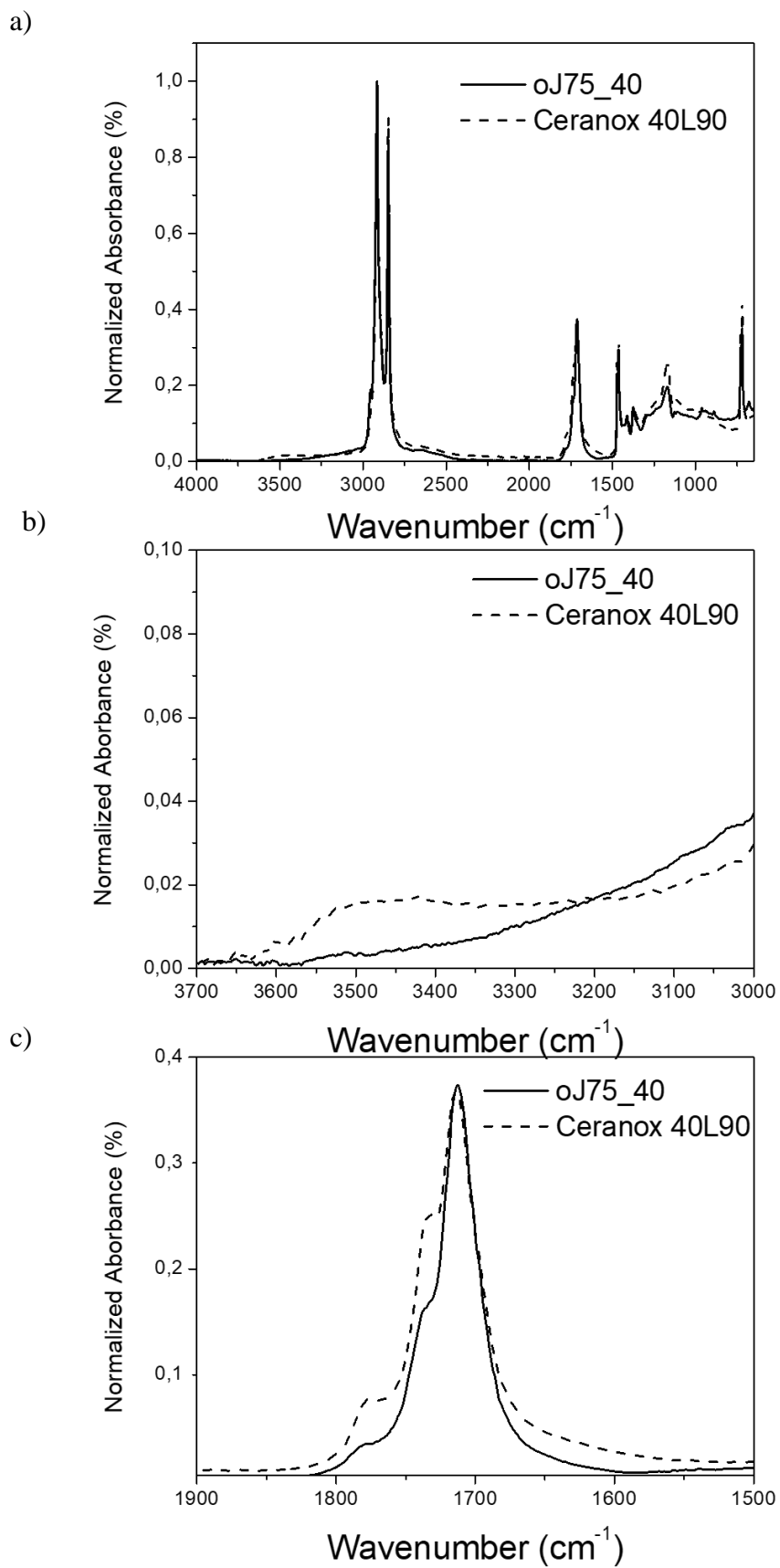


Figure 7.1: ATR-FTIR spectra of oJ75_40 and Ceranox 40L90. The absorbance ranges shown are for the a) full, b) hydroxyl and c) carbonyl regions.

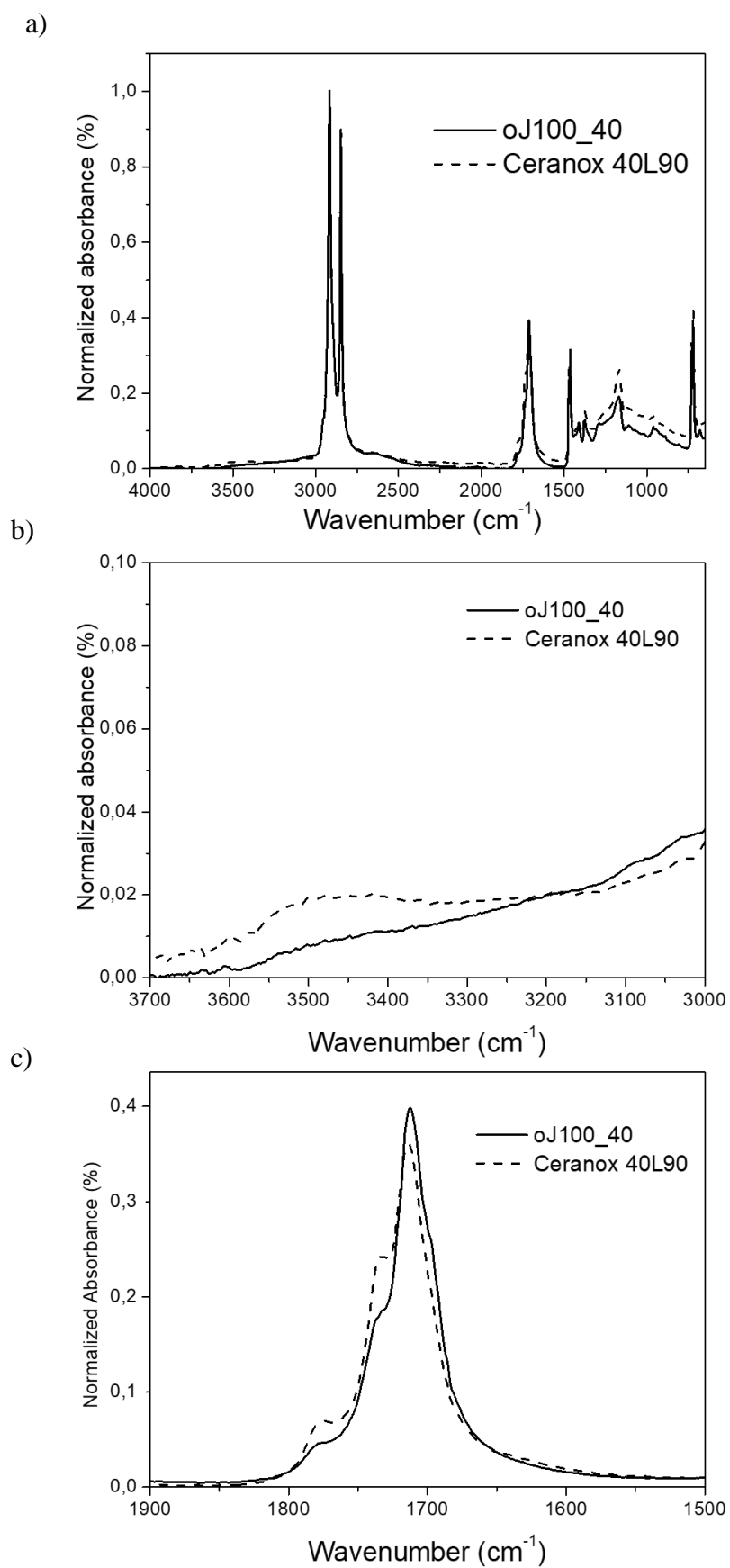


Figure 7.2: ATR-FTIR spectra of oJ100_40 and Ceranox 40L90. The absorbance ranges shown are for the a) full, b) hydroxyl and c) carbonyl regions.

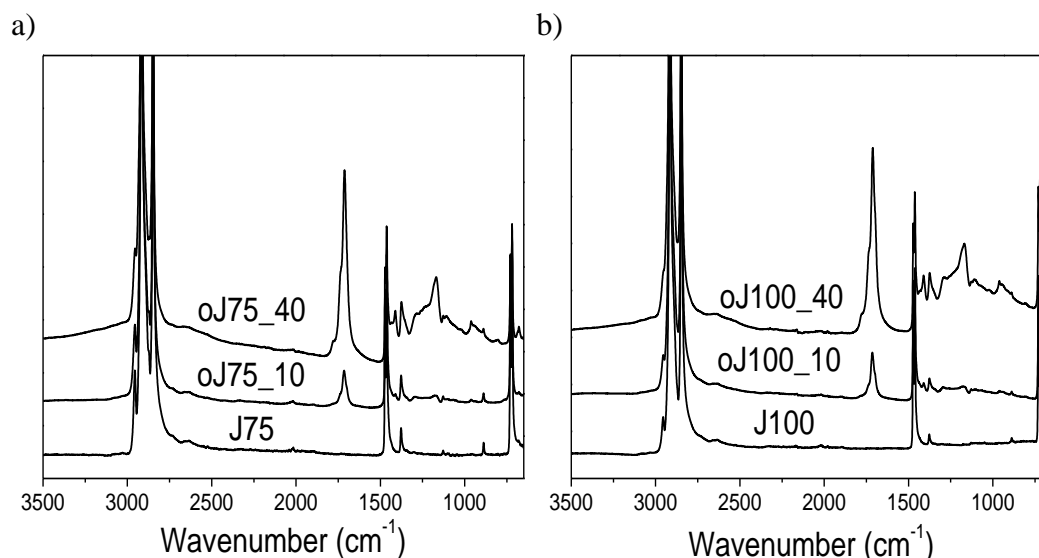


Figure 7.3: ATR-FTIR spectra showing the progression of oxidation during ozonolysis.

7.2 Experimental for stage 1 (Wax set 3):

7.2.1 High temperature - Solvent gradient interaction chromatography (HT-SGIC)

These experiments were performed on a high temperature liquid chromatography system (PolymerChAR, Valencia, Spain), utilizing a solvent gradient during analyses. For solvent gradient elution in HPLC, a high-pressure binary gradient pump (Agilent, Waldbronn, Germany) was used. The evaporative light scattering detector [ELSD, model PL-ELS 1000, Polymer Laboratories, Church Stretton, U.K. (Now Agilent)] was used for all detection purposes.

For the nonpolar separation, a Hypercarb column (Hypercarb®, Thermo Scientific, Dreieich, Germany) with an internal diameter of $100 \times 4.6 \text{ mm}^2$ and packed with porous graphite particles having a particle diameter of 5 μm (making a surface area of $120 \text{ m}^2 \text{ g}^{-1}$) and pore size of 250 Å, was used. These separations occurred according to ethylene sequence length. The column was placed in an oven at 120 °C. The mobile phase consisted of a solvent combination of decane and ODCB with a constant flow rate of 0.5 mL min^{-1} . A sample concentration of 2 mg mL^{-1} was used, and 50 μL of each sample was injected for all the experiments. The evaporative light scattering detector (ELSD) settings used were as follows: a gas flow rate of 0.5 SLM, 140 °C nebuliser temperature and an evaporative temperature of 200 °C.

For separation according to polarity, a silica column (Nucleosil, Macherey-Nagel, Düren, Germany) with a $300 \times 4.6 \text{ mm}^2$ length and internal diameter packed with silica particles of 5

μm and a pore size of 300 \AA , was used. The mobile phase flow rate used was 0.5 mL min^{-1} . 1-Hexanol was used as desorption promoting solvent and the flow rate was adjusted as needed. The ELSD settings used were as follows: a gas flow rate of 0.5 SLM, 140°C nebulizer temperature, and an evaporative temperature of 200°C . Sample concentrations of 2 mg mL^{-1} were used, and $50 \mu\text{L}$ of each sample were injected. All samples were prepared for injection in decane.

7.3 Results and discussion of stage 1 (Wax set 3)

7.3.1 Quantitative ^{13}C Nuclear magnetic resonance spectroscopy (^{13}C NMR)

As it is quite clear that there were differences between the FTIR spectra of the waxes created by the ozonolysis treatment and the commercially available polar wax, further investigation into the chemical nature of the waxes was conducted using quantitative ^{13}C Nuclear magnetic resonance (^{13}C NMR) spectroscopy. From Figures 7.4a and 7.5a the upfield chemical shift region of samples J75 and J100 can be seen, respectively. In this region the chain end carbons (1s-4s) can be seen at 14.2, 22.9, 32.2 and 29.6 ppm, respectively as well as the backbone methylene (CH_2) carbons at 30 ppm. All spectra were normalized to the backbone methylene signals. The chain end carbons had greater intensities for the J75 waxes compared to the J100 waxes. This is shown in Table 7.2 where the J75 chain end carbons showed signal integration values of $\pm 10 \text{ mol\%}$, compared to sample J100 which showed signals of $\pm 5.0 \text{ mol\%}$. This was due to the higher relative concentration of chain end carbons to the backbone carbons for the smaller J75 wax. An increase in the relative intensities of the chain end carbon signals compared to the backbone carbon signals was also observed as oxidation increased indicating a possible decrease in molecular size as oxidation progressed. The J100 sample showed the same increasing chain end concentration. This was a further indication of possible chain scission taking place thus increasing the chain end concentration.

Figures 7.4b and 7.5b show the downfield chemical shift region of J75 and J100 samples, respectively. Carbons that are electronically “de-shielded” due to electronegative functional groups such as carbonyls (170 - 215 ppm) or alkenes (105 - 125 ppm) appear in this region⁷⁰. In these figures, clear evidence of carbonyl functional groups contributed by aldehydes and/or ketones (211 ppm) and carboxylic acids (176 ppm) were seen⁷¹. Initially, sample J75 showed a carbon spectrum resembling that of a linear hydrocarbon. Sample J100 also showed a similar spectrum except for an additional alkene signal. This indicated some unsaturation prior to ozone treatment, which was a significant finding as unsaturated carbons are highly reactive.

This could be a reason for the slightly higher number of carbonyl carbons in the oxidized J100 samples. Progress of the oxidation process was followed by integration of the signal intensities of these carbons. Samples oJ75_10 and oJ100_10 which were subjected to lower amounts of ozone showed some carbonyl and alkene formation. With higher ozone concentrations the signal intensity of aldehydes/ketones and carboxylic acids increased. This was a clear indication of further oxidation. Additionally, new peaks started developing in the aliphatic regions at 43, 34, 25 and 24 ppm which were due to carbons in α and β positions to a specific carbonyl functional group. These carbons together with their associated carbonyl groups are shown in Table 7.2. It was difficult to assign these carbons to their respective groups in the aldehyde/ketone region as some overlap of signals are present together with the unpredictable position of a ketone on the backbone. There was however a definite twofold or threefold increase in intensity of these α and β carbons when compared to their respective carbonyl carbons. Further investigation into the direct quantification of aldehydes and ketones could be of great value, it was however seen as beyond the scope of this study. On the other hand, a clear ratio of 1:1:1 was observed for the carbonyl: α : β carbons of the carboxylic acid functional groups. This was in good agreement since carboxylic acid has only one α and β carbon associated with it.

Unsaturation, however remained relatively constant when compared to carbonyl formation. This could either indicate that alkene unsaturated groups remained constant throughout the ozonolysis process as a spectator group or the unsaturated groups were continuously consumed in the carbonyl product formation reaction.

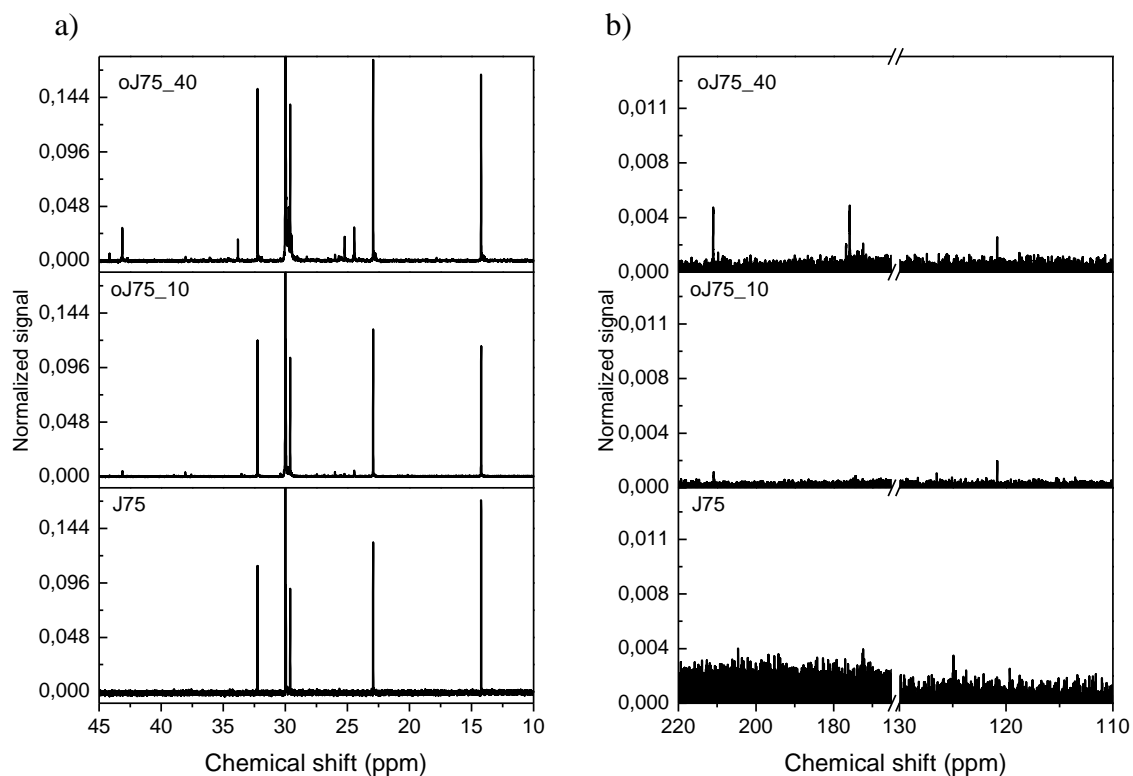


Figure 7.4: Enlarged ^{13}C NMR Spectroscopy results of a) upfield and b) downfield chemical shift regions for J75 samples.

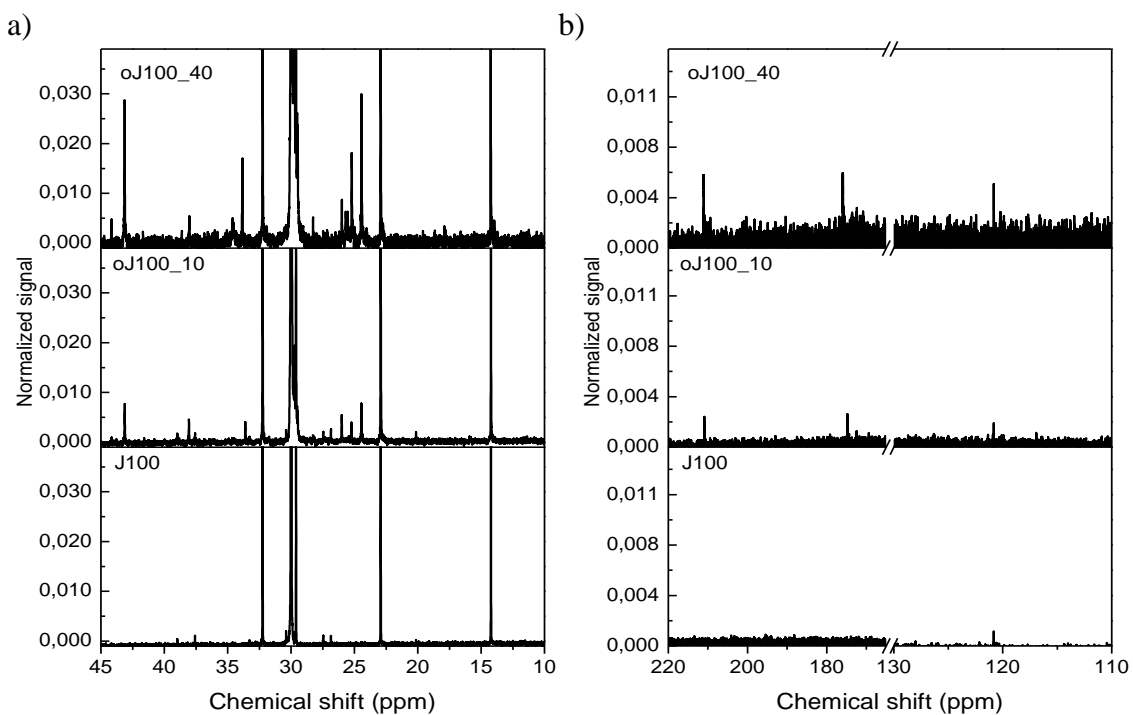


Figure 7.5 Enlarged ^{13}C NMR Spectroscopy results of a) upfield and b) downfield chemical shift regions for J100 samples.

Table 7.2: ^{13}C NMR chemical shifts and integrals of all waxes in the hydrocarbon region.

Functional group		Hydrocarbon			
Carbon assignment	Backbone	1s	2s	3s	4s
Chemical shift (ppm)	30	14.2	22.9	32.2	22.9
J75	100	10.6	10	9	8.4
oJ75_10	100	10.9	10.4	8.9	9.0
oJ75_40	100	12.6	12.0	9.5	9.7
J100	100	5.7	5.5	5.2	4.8
oJ100_10	100	6.0	5.9	5.1	5.5
oJ100_40	100	6.5	6.3	5.6	7.1

Table 7.3: ^{13}C NMR chemical shifts and integrals of all waxes in the carbonyl and alkene regions.

Functional group	Aldehyde/Ketone			Carboxylic acid			Alkene
Carbon assignment	Carbonyl	α	β	Carbonyl	α	β	RC=CR
Chemical shift (ppm)	211	43	24	176	34	25	121
J75	-	-	-	-	-	-	-
oJ75_10	0.2	0.4	0.4	0.2	0.2	0.2	0.2
oJ75_40	1.0	2.5	2.2	1.1	1.1	1.1	0.3
J100	-	-	-	-	-	-	0.1
oJ100_10	0.3	0.8	0.7	0.4	0.4	0.4	0.1
oJ100_40	1.0	3.3	3.4	2.0	2.0	2.0	0.3

7.3.2 Differential scanning calorimetry (DSC)

From differential scanning calorimetry (DSC) experiments a total decrease in crystallinity was seen for both sample sets as oxidation increased. The total crystallinities for both sample sets decreased uniformly from roughly 80% to around 50%, as illustrated in Table 7.4. Figure 7.6 shows the melting endotherms of the waxes as a function of oxidation. There was a more observable shift in the melting endotherm maxima from a higher to a lower temperature for the J100 sample set with progression of oxidation. For the J75 sample set, endothermic melting peak temperatures were less affected by oxidation. However, in both the J75 and J100 sets a

significant broadening in thermograms were seen with increasing degree of oxidation indicating more heterogeneous crystalline morphologies compared to the unoxidized neat wax counterparts.

Both samples showed a characteristic FT wax multimodal melting peak distribution⁷². Multiple factors could affect the crystallinity of the samples. In the case of linear polyethylene molecules, a sample's crystallinity is affected by the number of chains with a chemical composition which allows for the dense packing of molecules, hence crystalline packing⁴³. For linear hydrocarbons this means that degree of linearity should be high and that the degree of branching and presence of any other chemical species should be low. It was therefore expected that an increase in chain alterations would result in a decrease in chain uniformity, limiting the dense chain packing upon crystallization, which in turn would lead to a decrease in degree of crystallinity. As seen from the preceding NMR results, there was a clear increase in oxygenate moieties together with a decrease in chain end intensities. These newly functionalized moieties most likely behaved as crystallinity disrupters and led to other less crystalline domains, and hence the broadening of the thermal transitions seen by DSC.

These results were further accentuated by the crystallization data. In Table 7.5 the onset of crystallization, exotherm maxima, and crystallization enthalpy was seen to decrease with increasing oxidation levels for both sample sets. Figure 7.7 also showed a broadening of the crystallization peaks. This was a clear indication of the crystallization behaviour being disrupted by the increase in the presence of oxygen moieties across the hydrocarbon backbone.

Table 7.4: DSC melting results of all wax samples.

Sample	Onset of melting endotherm (°C)	Endotherm maxima (°C)	Melt Enthalpy (J/g)	Crystallinity (%) ⁹
J75	47	73.4	238.1	81.2
oJ75_10	43	74	224.3	76.6
oJ75_40	31	69	152.7	52.1
J100	52	94; 110	236.2	80.61
oJ100_10	47	87; 105	216.3	73.8
oJ100_40	35	79; 98	151.6	51.7

Table 7.5: DSC crystallization results of all wax samples.

Sample	Onset of crystallization endotherm (°C)	Endotherm maxima (°C)	Crystallization Enthalpy (J/g)
J75	74	68	226
oJ75_10	72	66	200
oJ75_40	69	62	133
J100	103	96; 86	231
oJ100_10	98	95; 83	199
oJ100_40	91	87; 77	123

⁹ The standard heat of fusion for 100% crystalline PE of 293 (J/g) was used.

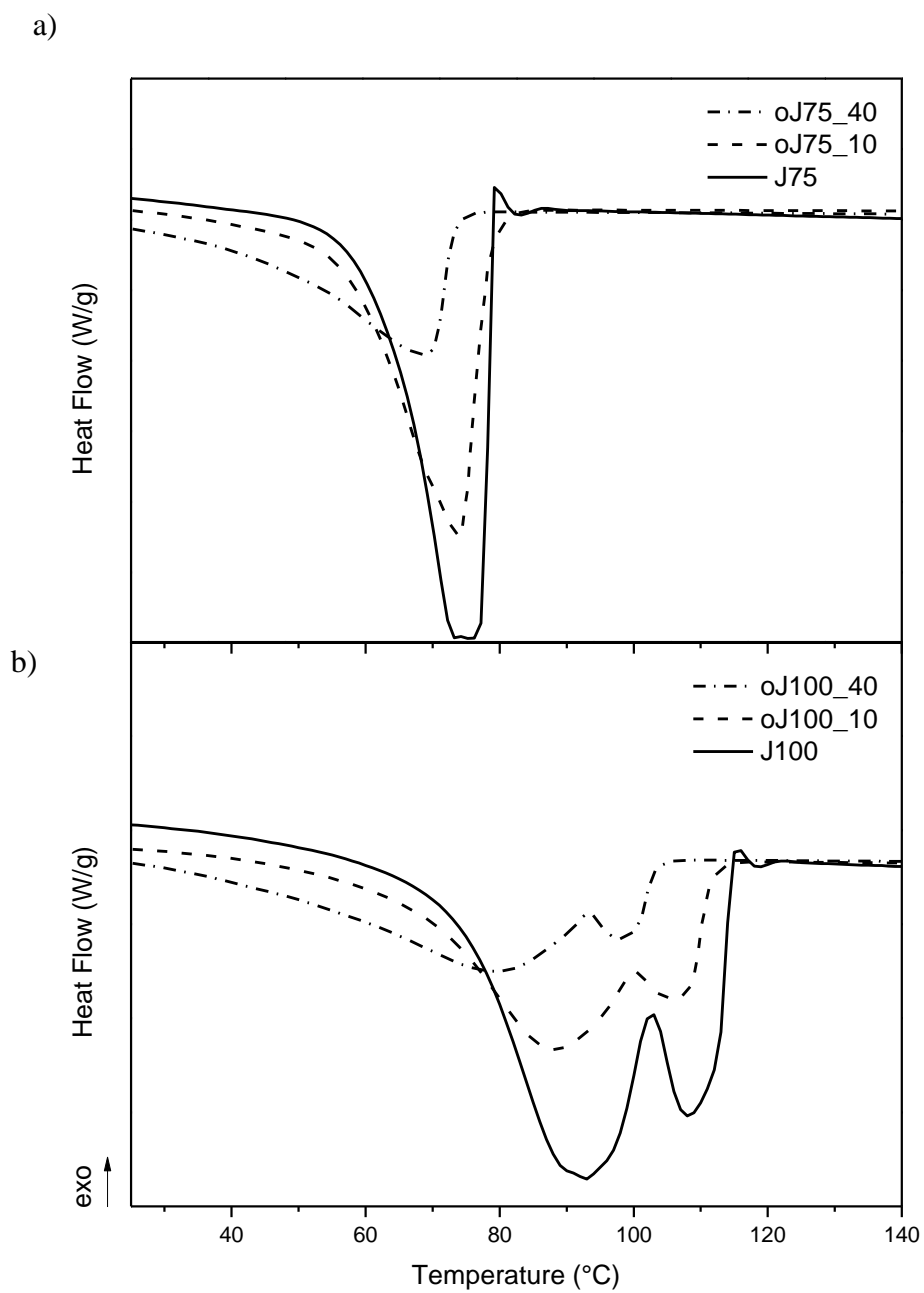


Figure 7.6: DSC melting thermograms showing the effect of oxidation on melting behaviour of a) J75 and b) J100 waxes.

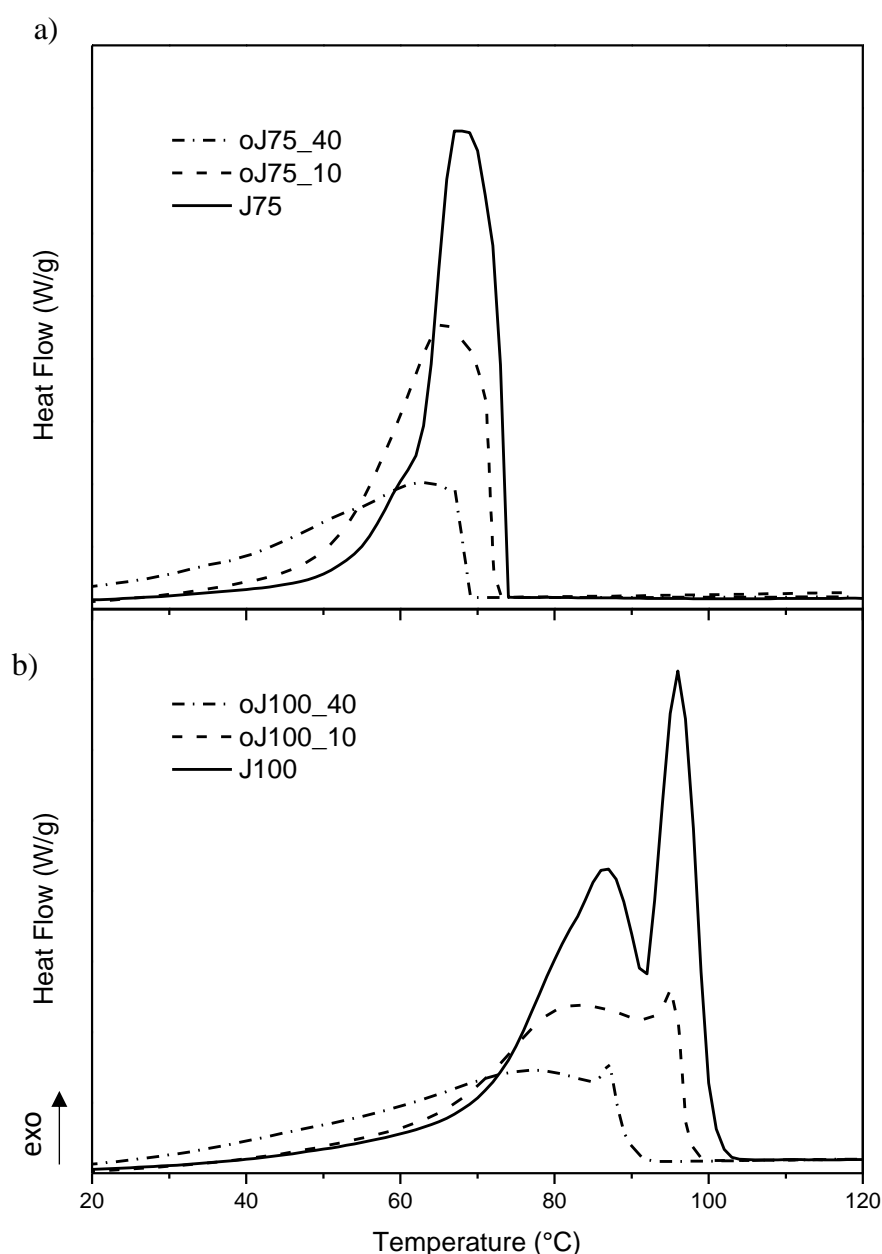


Figure 7.7: DSC crystallization thermograms showing the effect of oxidation on crystallization behaviour of a) J75 and b) J100 waxes.

7.3.4 High temperature - size exclusion chromatography (HT-SEC)

To investigate if molecular size was affected by the oxidation process, it was decided to conduct a high temperature size exclusion chromatography (HT-SEC) experiment. HT-SEC experiments are based on the hydrodynamic volume (H_v) of a molecule in solution. The H_v of the sample is then related back to a molecule's molecular weight (MW) using polyethylene standards of known MW. From Table 7.6 it can be observed that sample J75 had a smaller

number-average molecular weight (M_n) of 525 g/mol compared to sample J100 with a M_n of 969 g/mol. As ozonolysis progressed, the general unimodal shape of the sample was maintained however, the molecular weight distribution for both sample sets broadened. In Figure 7.8a it can be observed that sample oJ75_40 showed increasing detector responses on both sides of the bulk elution peak at 25.5 mL, compared to the neat J75 sample. This implies a simultaneous increase and decrease in H_v . The reason for a decrease in MW was due to the J75 molecules breaking up into smaller molecules during ozonolysis. The increase in MW which showed an increased elution peak between 24 and 25 mL could be due to an association interaction between newly formed species or the effect of oxygen moieties on the H_v of a sample⁷³.

Figure 7.8b shows that the MW distribution increased for sample oJ100_40 but skewed only to the higher elution volume side of 26.5 mL. These large differences at higher volumes were most probably due to chain scission as a result of oxidation. These results show a similar trend as seen in the DSC experiments. From Table 7.4 a decrease in crystallinity is accompanied by an increase in molecular weight dispersity seen in Table 7.6. This effect is more pronounced in the J100 sample set than in the J75 sample set. Both samples with highest ozone exposure had decreased crystallinities of about 50%. The dispersity of oJ100_40 however is much larger at 1.5 compared to the oJ75_40 sample which had a dispersity of only 1.2. This showed that by only changing the degree of dispersity slightly for the smaller J75 sample set had a much greater effect on the crystallinity thereof. As mentioned in the DSC section, chain uniformity is an important property for linear hydrocarbon crystallinity. An effective way to gauge this property is by measuring a sample's ethylene sequence length. A liquid chromatography experiment was therefore conducted to investigate the ethylene sequence lengths of the waxes to gain further insight into the oxidized wax compositions.

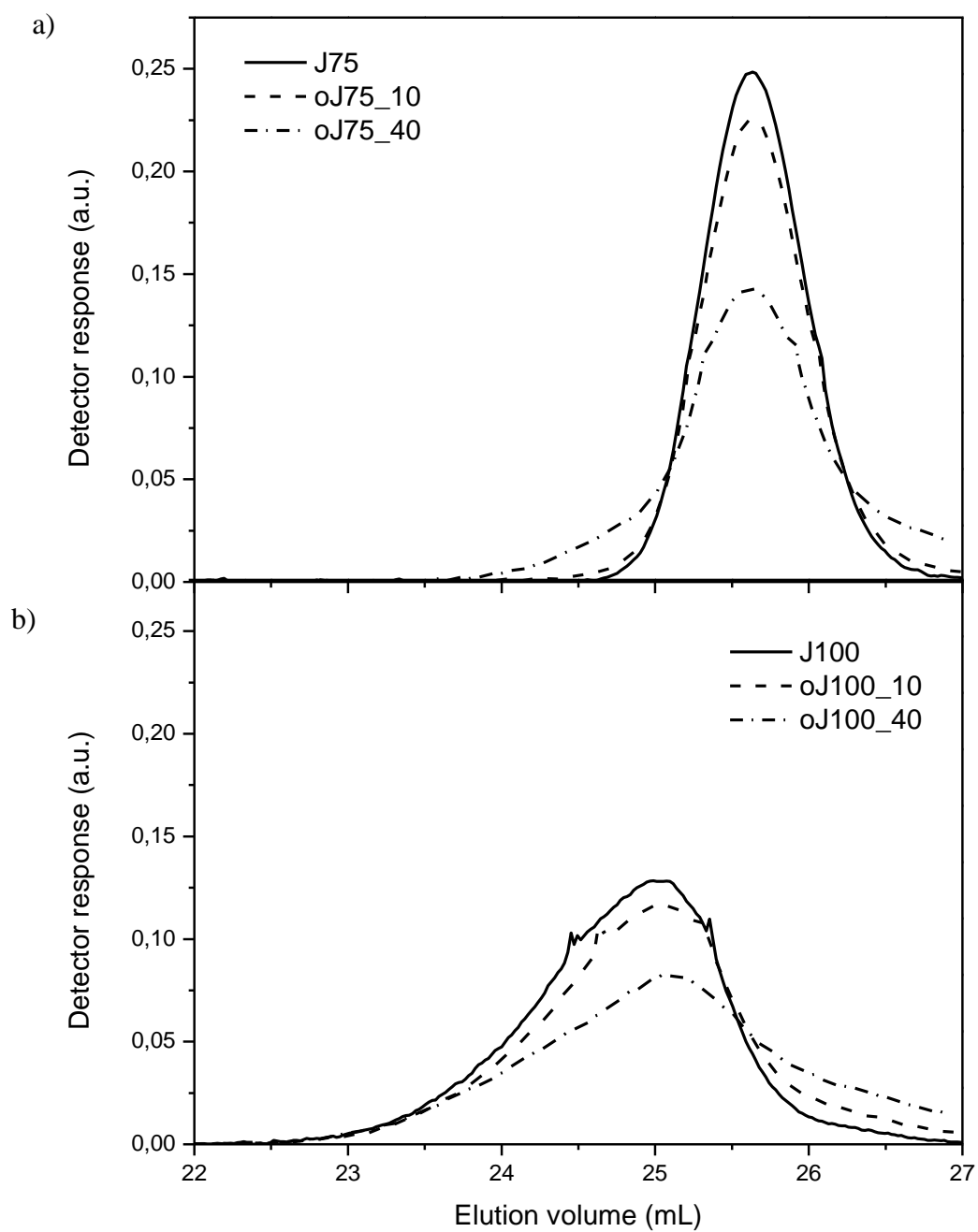


Figure 7.8: HT-SEC chromatograms of a) J75 and b) J100 waxes.

Table 7.6: HT-SEC results of all wax samples.

Sample	M _p (g/mol)	M _n (g/mol)	M _w (g/mol)	Đ
J75	515	525	564	1.1
oJ75_10	520	518	568	1.1
oJ75_40	510	489	617	1.2
J100	880	969	1142	1.2
oJ100_10	821	843	1057	1.3
oJ100_40	831	694	1012	1.5

7.3.5 High temperature - solvent gradient interaction chromatography (HT-SGIC)

7.3.5.1 Reverse phase HT-SGIC

High-temperature solvent gradient interaction chromatography (HT-SGIC) was used to probe the nonpolar ethylene sequence length (ESL) of the waxes. This was achieved by fractionating wax samples on a nonpolar porous graphite column (stationary phase) combined with a controlled solvent gradient elution profile (mobile phase). By using a nonpolar stationary phase, the nonpolar ethylene sequences are adsorbed onto it by means of van der Waal's force interactions. Initially the mobile phase was in isocratic mode, using decane as solvent. During isocratic mode, any weak adhering molecules such as molecules with short ESLs, eluted with the decane solvent whereas molecules with longer ESLs had higher affinity to adsorb to the stationary phase. Gradual addition of a desorption promoting solvent such as dichlorobenzene to the mobile phase allowed samples with stronger adhesion (or longer ESLs) to desorb from the column and elute. Using a solvent gradient, the samples should therefore elute in order of increasing column adhesion strength. In this experiment all samples were doped with a standard linear C₅₀ hydrocarbon oligomer marker to comparatively gauge where the waxes eluted.

When comparing Figures 7.9 and 7.10 a clear difference in elution profiles can be seen with the J75 sample set eluting much earlier than the J100 sample set. The bulk of the J75 samples also eluted before the C₅₀ marker, whereas the peak of the J100 samples eluted around the same time as the marker. In addition, the J75 samples showed narrower elution profiles compared to the J100 samples, correlating with the narrower, more homogeneous molecular weight distribution seen for the J75 sample in HT-SEC. It can therefore be concluded that the J75

samples consisted of short and narrow ESL distributions, whereas the J100 samples exhibit longer ethylene sequences and broad ESL distributions. These results compare well with the trends seen from the HT-SEC experiments, from which it was concluded that as the ethylene sequences were interrupted, they were broken down into smaller chains.

The effect of oxidation was seen in both sample sets as a decrease in the earlier eluting signal with increasing ozone exposure. A study done by Ndiripo et al.⁷⁴ has shown this to be as a result of the difficulty in detecting multifunctional species within the evaporative light scattering detector (ELSD). In their study on oxidized and non-oxidized waxes, it was concluded that the decrease in detector signal was due to the fact that neat waxes have different refractive indices than waxes with oxygen functionalities. In both cases the signal decreased throughout the entire elution profile range. From these results it can therefore be concluded that the entire ESL range was disrupted by oxygen functionality. Hence, the ozonolysis process had no major preference for affecting either the short or long chain sequences within the waxes.

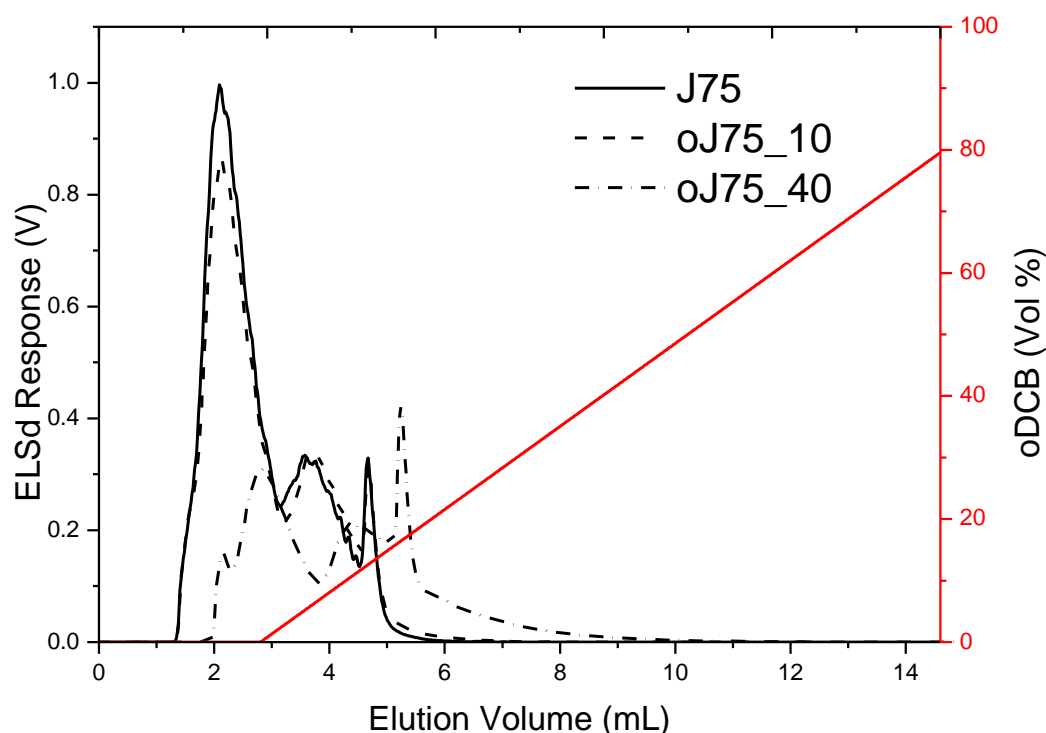


Figure 7.9: Reverse phase HT-SGIC elution profiles for the J75 sample set.

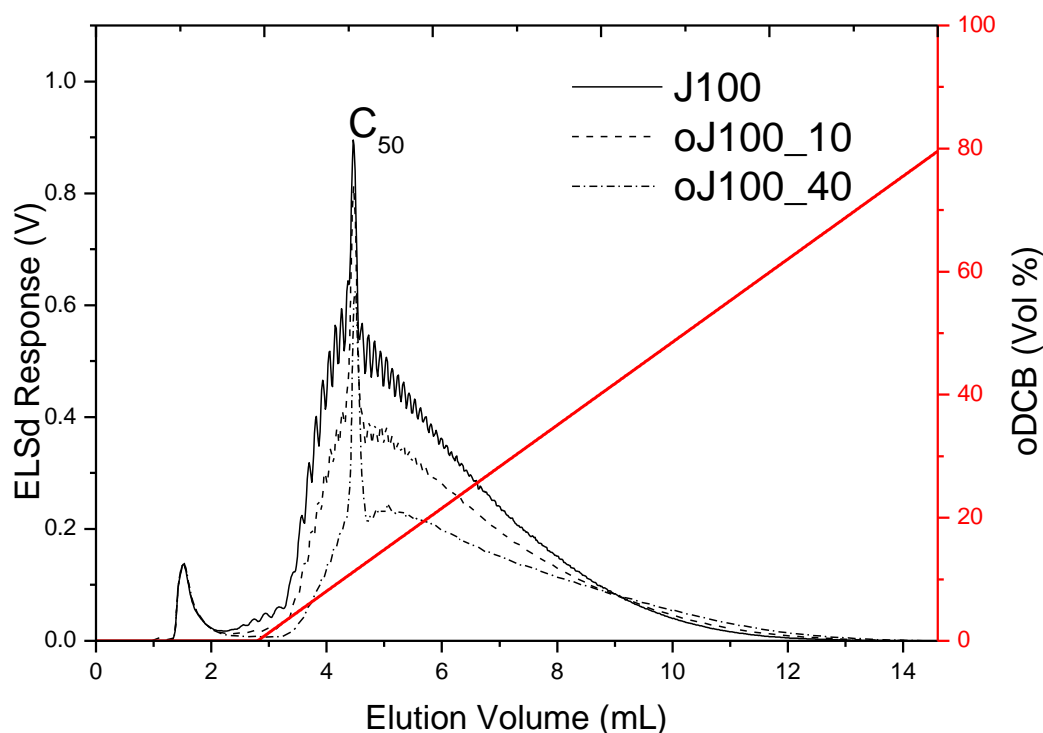


Figure 7.10: Reverse-phase HT-SGIC elution profiles for the J100 sample set.

7.3.5.2 Normal phase HT-SGIC

Polar separation was achieved using a polar silica column together with a nonpolar mobile phase. During isocratic mode it allowed all non-retained nonpolar wax molecules to elute. Thereafter, the polarity of the mobile phase was increased by systematic addition of a desorption promoting polar solvent (1-Hexanol). This resulted in the desorption of slightly retained (slightly oxidized) material. By further increasing the mobile phase polarity, the strongly retained (highly oxidized) material could be eluted⁷⁴.

Polarity of a wax is governed by the number and type of oxygenates present on a specific chain. In each sample set the neat samples eluted entirely during the isocratic mode at around 3 mL (Figures 7.11 and 7.12). This nonpolar peak broadened as oxidation increased and the broadening was more pronounced for the J100 sample set. This might be due to the larger J100 molecules which consists of a longer nonpolar chain segment, resulting in relatively higher nonpolar contribution to the overall polarity of the sample.

As oxidation increased, the nonpolar peak intensity reduced as a new peak started appearing at around 9 mL. These peaks appearing at later elution volumes was due to chains with higher

polarity. To elute the highly oxidized fractions, the volume of 1-Hexanol was increased greatly. Samples oJ75_40 and oJ100_40 showed a highly oxidized sample peak at around 11.5 mL.

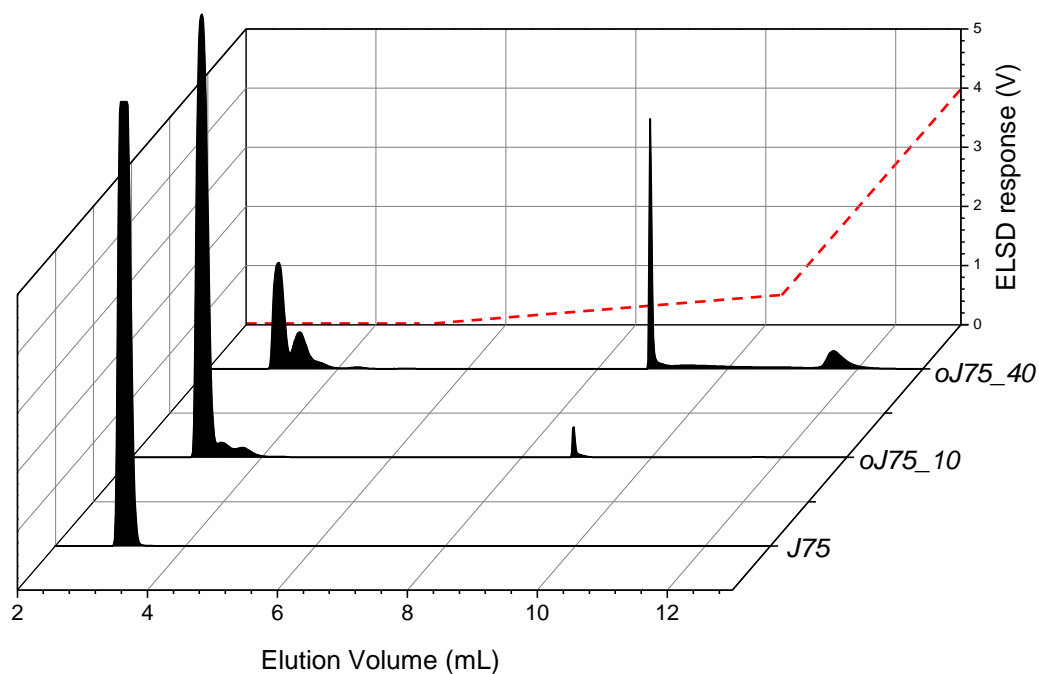


Figure 7.11: Normal-phase HT-SGIC elution profiles of the J75 sample set. 1-Hexanol flow rate profile = red dashed line.

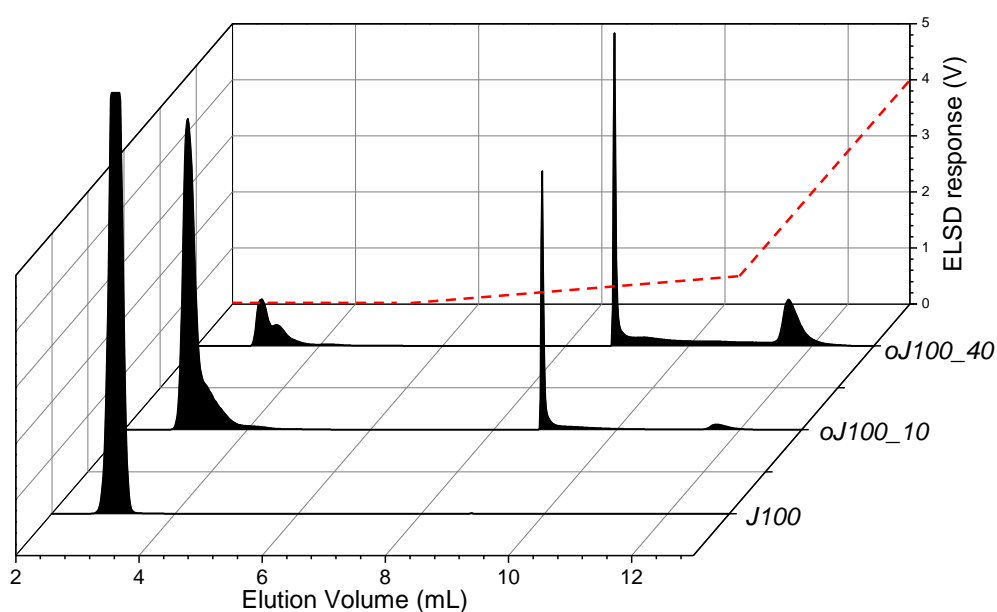


Figure 7.12: Normal-phase HT-SGIC elution profiles of the J100 sample set. 1-Hexanol flow rate profile = red dashed line.

The preceding data shows that two linear hydrocarbon FT waxes of different molecular weights were successfully oxidized to varying degrees and characterized. In both sample sets, two levels of oxidation were achieved by varying the amount of ozone gas introduced to each sample. Initially, the level of oxidation was tracked using an off-line ATR-FTIR analysis technique wherein the carbonyl region was measured relative to the hydrocarbon methylene stretching bands. The types of oxygenates were probed using quantitative ^{13}C -NMR. DSC analysis showed that the inclusion of these oxygenates interrupted the crystallinity and melting behaviour of the samples. HT-SEC and HT-SGIC showed complimentary results wherein it could be concluded that the samples were broken down into smaller chains as the ESL was influenced.

The samples were synthesized under similar experimental conditions, resulting in them having comparable chemical and morphological properties. This allowed for conclusions to be drawn to any of these properties when the samples are applied to the method that was developed later on in this chapter.

7.4 Results and discussion of stage 2 (Wax set 3)

In Figure 7.13 during the stage 2 experiment with binary blends, no association of wax with the PVC particles was observed. This finding was unexpected as it was believed that oxygenate moieties should introduce some associative character. The question then arises as to why Ceranox 40L90 and oHDPE showed association (Chapter 6). One major difference between these waxes and the two oFT waxes from this experiment was that they were of higher molecular weight, thus apart from polarity, chain mobility and melt viscosity could also have been factors influencing the wax dispersion across PVC particles. In Figures 7.14 and 7.15 the ternary blends are shown. In these figures all the waxes showed greater dispersion regardless of their MW or degree of oxidation.

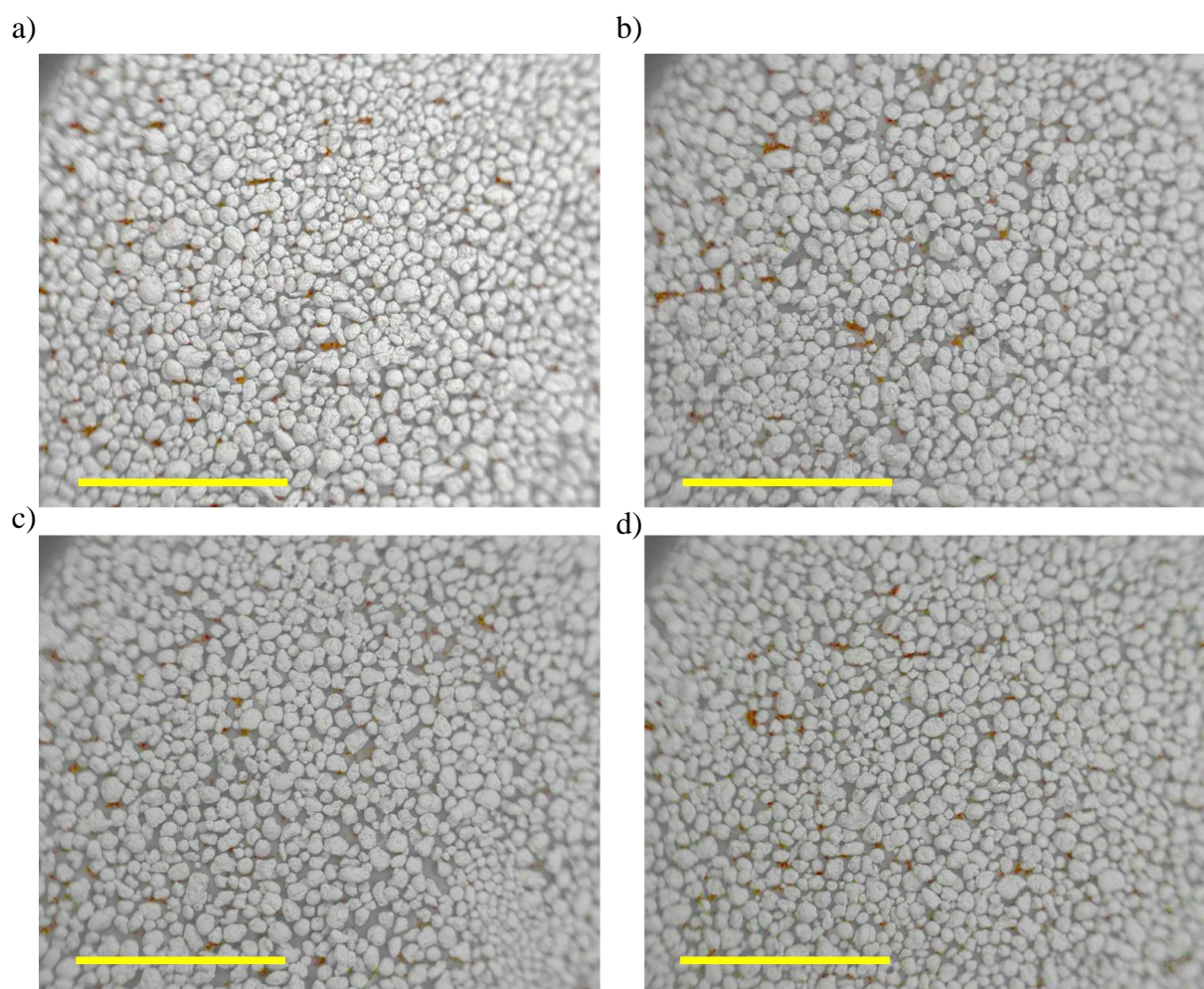


Figure 7.13: SEM-EDS images of PVC/wax binary blends for a) oJ75_10; b) oJ75_40; c) oJ100_10 and d) oJ100_40. Electron image = grey; Carbon = red; Oxygen = green. Scale bar = 2 mm.

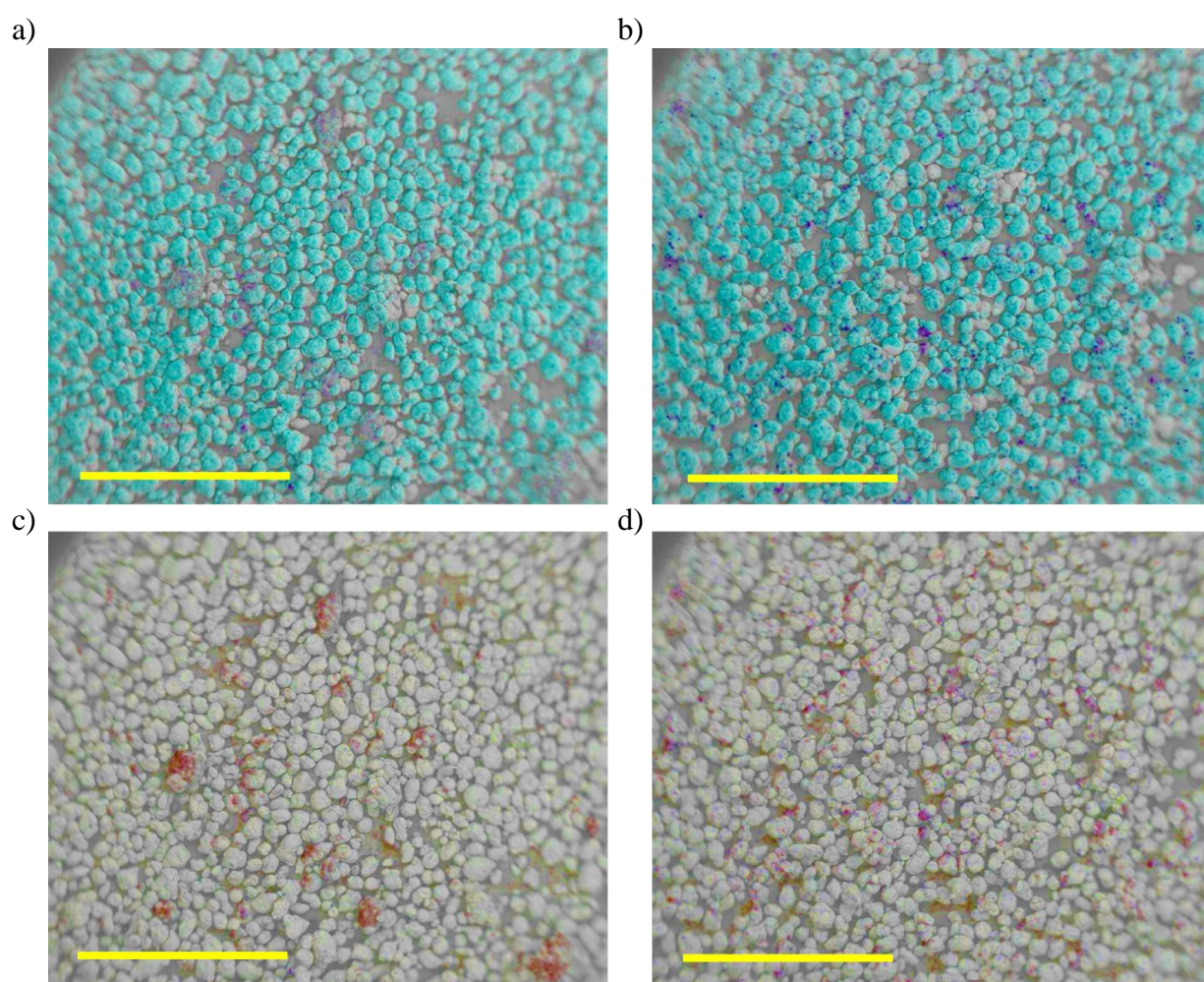


Figure 7.14: SEM-EDS images of PVC/wax/CaSt ternary blends for a and c) oJ75_10; b and d) oJ75_40. Electron image = grey; Chloride = blue; Carbon = red. Calcium = purple; Oxygen = green. Scale bar = 2 mm.

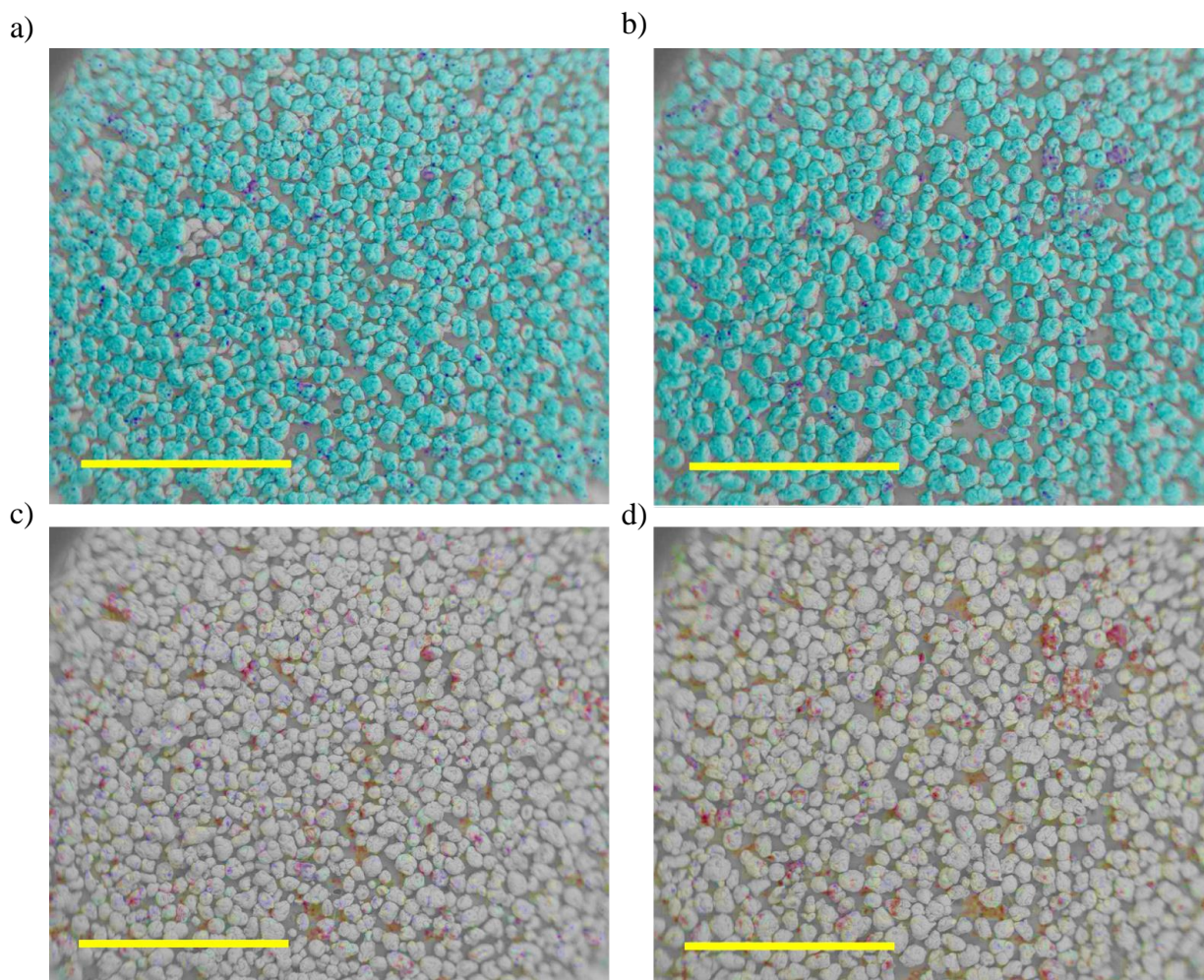


Figure 7.15: SEM-EDS images of PVC/wax/CaSt ternary blends a and c) oJ100_10; b and d) oJ100_40. Electron image = grey; Chloride = blue; Carbon = red. Calcium = purple. Scale bar = 2mm.

7.5 Results and discussion of stage 3 (Wax set 3)

Figure 7.16 shows all the stage 3 experiments for both binary and ternary blends of these samples. Sample oJ75_10 showed complete fusion for the binary blend (Figure 7.13a) but not for the ternary blend (Figure 7.13e), where some wax inclusion could still be observed in the ternary blend. Sample oJ75_40, however, showed complete fusion in both the binary and the ternary blend.

From previous stage 3 experiments it was found that high melting point (above the T_g of PVC) waxes such as J100 did not fuse properly at these extruder conditions. Experiments that followed showed that polar waxes, also consisting of peak melting points above the T_g of PVC, did in fact fuse at these extruder conditions. It was therefore concluded that the effect of polarity played a big role in fusion behaviour. Interestingly however, in this sample set of oxidized FT waxes, sample oJ100_10 also showed insufficient fusion for both the binary and

ternary samples (Figures 7.13c and 7.13g). This could be seen due from the disruption of the chloride signal uniformity. Sample oJ100_40 with a higher degree of oxidation showed complete fusion, it did however also have a decreased melting temperature due to the oxidation process (Figure 7.5). The effect of fusion could therefore not only be ascribed to an increased oxidation level and hence polarity, but an additional effect of decreased melting behaviour and possibly differences in chain mobility should also be taken into account.

Performing fusion studies on the Brabender extruder could not provide much information on fusion times and efficiency. To further investigate the effect on fusion parameters it was decided to do a series of fusion studies on these waxes using a more commercially relevant torque rheometry method.

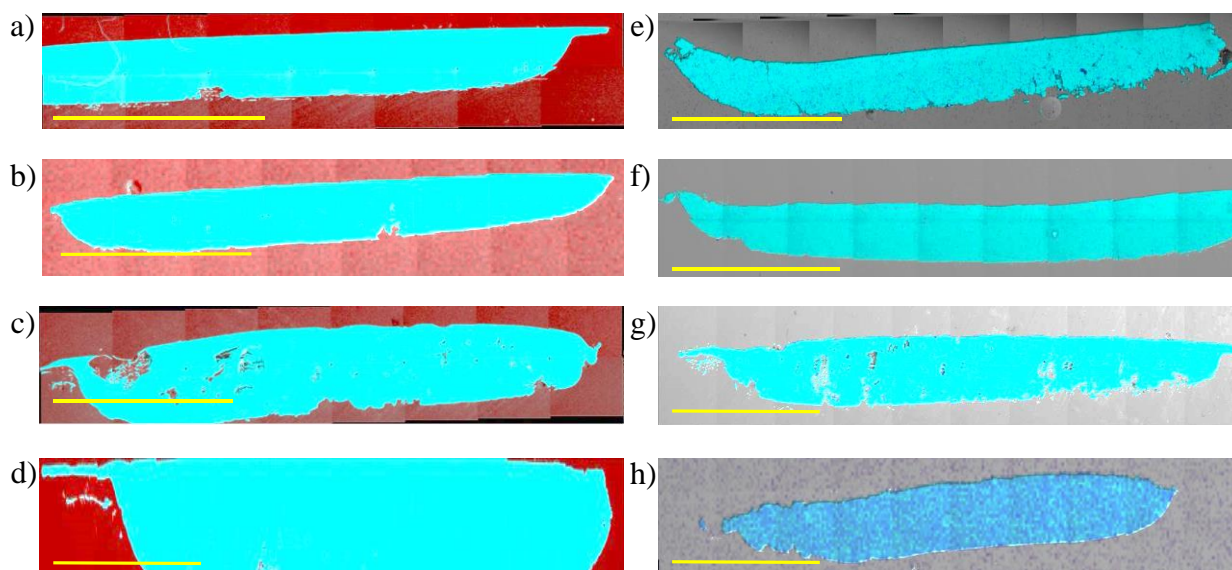


Figure 7.16: SEM-EDS images of binary blends a) oJ75_10; b) oJ75_40; c) oJ100_10 and d) oJ100_40 and ternary blends e) oJ75_10; f) oJ75_40; g) oJ100_10 and h) oJ100_40 after screw freezing. Electron image = grey; Chloride = blue; Carbon = red. Calcium = purple. Scalebar = 5 mm.

7.6 Commercial application (Fusion testing)

During the stage 3 experiments it was concluded that the waxes plated out (migrate to extrudate surface) due to their absence in the micrographs (Figure 7.16). To further investigate if these synthesized waxes had any effect on the fusion behaviour of PVC, a series of fusion studies were proposed. Commercially relevant lubricant concentrations were used to formulate PVC blends that are comparable to that of industry standards. Formulation ingredients were in alignment with acceptable limits as documented within the TR-2 guidelines as published by

the Plastics Pipe Institute (PPI). The formulations that were tested are listed in Table 7.7. The set of waxes that were investigated were the J75 series consisting of neat nonpolar J75 and two oxidised oJ75_10 and, oJ75_40 waxes as well as the J100 series consisting of neat nonpolar J100 and two oxidised oJ100_10 and, oJ100_40 waxes. Apart from the full ternary formulation containing both internal and external lubricants, binary blends were also analysed to investigate the fusion behaviour in the absence of the calcium stearate component.

Table 7.7: Formulation composition of binary and ternary PVC blends.

Compound	Ternary blend (phr)	Binary blend (phr)
PVC	100	100
Wax	0.9	0.9
Calcium Stearate	0.6	-
Tin stabilizer	0.6	0.6

Fusion studies were performed on a Thermo Scientific torque rheometer coupled with a Haake Rheomixer. Two time-dependant torque measurements were conducted at 65 rpm and experimental temperatures of 185 and 190 °C, respectively. The total mass of each sample was 65 g. The general interpretation of a PVC fusion curve is shown in Figure 7.17 where an increased torque at point A represents the fusion event and region B represents the stable time of a formulation. The stable time is therefore measured as the time elapsed between fusion event and the onset of degradation. The onset of degradation can be seen by the increase in torque towards higher time values. From point A the fusion time and torque can be obtained.

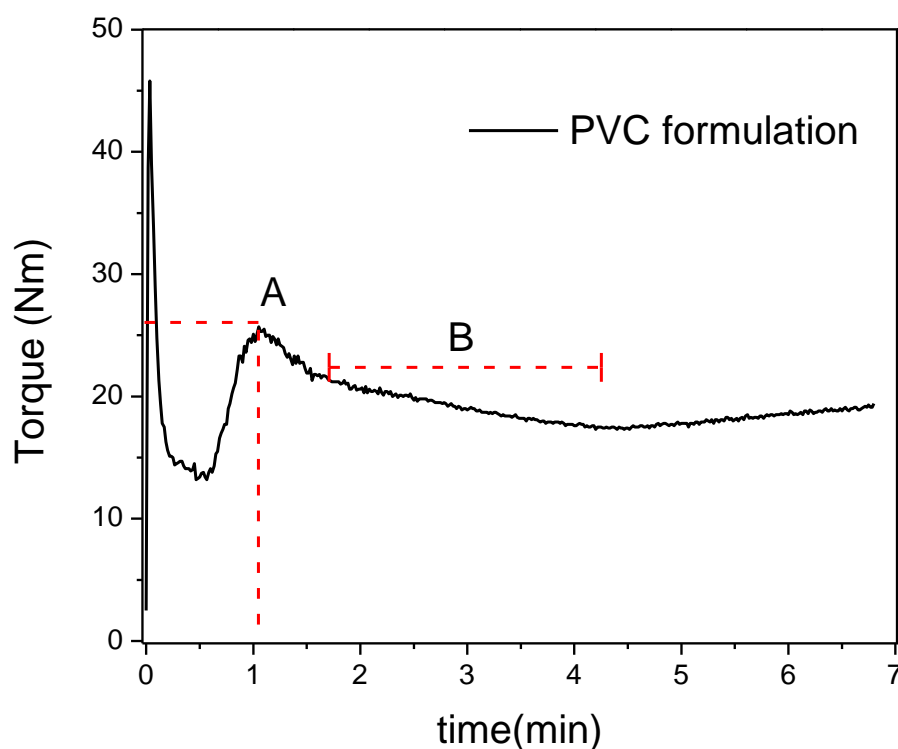


Figure 7.17: General interpretation of a PVC fusion curve.

Figure 7.18 shows the fusion curves of the ternary blends. Figure 7.18a shows that the unoxidized J75 sample did not fuse at 185 °C. It also shows that by slightly increasing the level of oxidation, fusion was promoted with an increase in torque as fusion time decreased. This effect however might not solely be due to increased polarity but as was observed from the preceding characterization sections within this chapter, oxidation affected the wax properties in various ways. The melting temperature and molecular size decreased with increased oxidation, both of which can lead to earlier fusion. The overall effect can therefore not only be ascribed to an increase in polarity, but a combination of effects should be considered. Figure 7.18b shows that by increasing the temperature, the unoxidized J75 sample fused. Additionally, for the oxidized samples, differences in fusion time and torque are minimized with an increase in temperature due to the increase in thermal energy overcoming the smaller morphological differences and intermolecular forces at play. Figure 7.18c shows that both the unoxidized J100 and oxidised oJ100_10 samples did not fuse at the lower experimental temperature of 185 °C, despite oJ100_10 having comparable oxidation levels as oJ75_10. This must therefore be due to the molecular size or melting temperature differences between the two samples. As the

temperature was increased to 190 °C in Figure 7.18d, both oxidised oJ100_10 and oJ100_40 resulted in fusion. The neat nonpolar J100 wax formulation needed even higher thermal energy (above 190 °C) to promote fusion. This clearly shows that by slightly increasing the level of oxidation in the wax, feasible fusion times (3 - 5 min) can be achieved at lower temperatures.

When comparing the J75 and J100 series, the J75 series were more versatile with respect to changes in experimental conditions. It also showed that the degree of oxidation influenced the fusion behaviour and that the effect was more accentuated for the smaller J75 wax molecules since the oJ75_10 sample fuses at 185 °C whereas the oJ100_10 did not fuse. This leads us to believe that the overall polarity is more important than just the degree of oxidation. Moreover, the effect that oxidation has on the other morphological properties of the wax, also plays an important role in manipulating the fusion behaviour of a PVC formulation.

Further comparing all the highly oxidized samples (40 % oxidation), all the samples showed similar, rapid fusion with fusion times of ± 1 min and torque readings of ± 30 Nm. The lower oxidized samples (10 % oxidation) however showed more varying fusion behaviour. High friction leads to rapid fusion due to inefficient lubrication or high association of the lubricant towards the PVC matrix. This suggests that there exists an oxidation limit where the wax loses its slip agent functionality and becomes more of a surfactant. There should therefore exist an inflection point where the level of oxidation becomes the dominating factor when compared to other wax properties such as melting point, molecular size and molecular chain mobility (melt viscosity). Also, oJ100_10 showed a similar fusion profile to that of sample J75 which highlights the fact that similar fusion profiles can be achieved by simply modifying the oxidation state of a hydrocarbon wax.

The stable times of the formulations remained unchanged with an increase in oxidation level which is an interesting finding as this shows shorter fusion times with minimal changes in stable time. Stable times decreased marginally with an increase in temperature.

Binary systems were also investigated (Figure 7.19). These samples were expected to show a delay in fusion with the absence of an internal fusion promoter, as per conventional lubricant classifications²⁴. This was however not the case as all the samples fused rapidly under 2 min. The cause for this behaviour could be that too little wax lubricant was present in the formulation which resulted in the rapid fusion thereof. Although the wax concentration was constant for binary and ternary systems, in the absence of calcium stearate in the binary blends the wax molecules might have penetrated deeper into PVC crevices and interparticle voids,

thus lowering the relative wax concentration at the metal surface interface. This suggests that if the effect of a binary system, using modified wax as multifunctional lubricant, is to be investigated and careful considerations are needed in adjusting lubricant concentrations.

Comparing these findings to the SEM-EDS micrographs taken for these samples in stage 3 provided plenty of information to try and explain the mechanism at hand. It should however be remembered that in stage 3 the temperature was set to 190 °C and that higher wax concentrations were used for the formulations. The neat J75 stage 3 micrograph seen earlier in Figure 6.13 showed complete fusion in both the binary and ternary blends. The J100 sample was excluded from the Wax set 2 selection as it did not fuse under the selected Brabender conditions. These two results correlated well with what was seen from the fusion studies as complete fusion was seen for the J75 sample and no fusion was observed for the J100 sample. From this data it can be concluded that due to no wax being present in the micrographs, for complete fusion to have occurred, all the wax must have migrated outwards towards the instrument sidewalls. The J100 sample however, stayed in powder form and did not fuse which means that these larger wax molecules took too long to migrate out to the sidewalls. This can be overcome by the addition of more thermal energy which would result in increased molecular motion of the wax molecules and therefore promote earlier fusion. In Figure 7.16 all the samples, except for oJ100_10, showed complete fusion. This also shows that for complete fusion to take place, all the lubricant needs to be expelled from the PVC matrix which would therefore allow it to fuse. To explain the fusion trends that were observed for increasing wax oxidation levels, the mechanism of surfactants and slip agents proposed by Rabinovitch (Figure 1.2) can be used. In this mechanism, CaSt acts as a surfactant and wax acts as a slip agent. A nonpolar wax would therefore have the least association with CaSt and therefore delay the fusion to a greater extent. As oxidation is increased the degree of chemical association between the CaSt and the wax is also increased. The oxidized wax would then also act as more of a surfactant rather than a slip agent, and in doing so increase the overall friction thus resulting in earlier fusion.

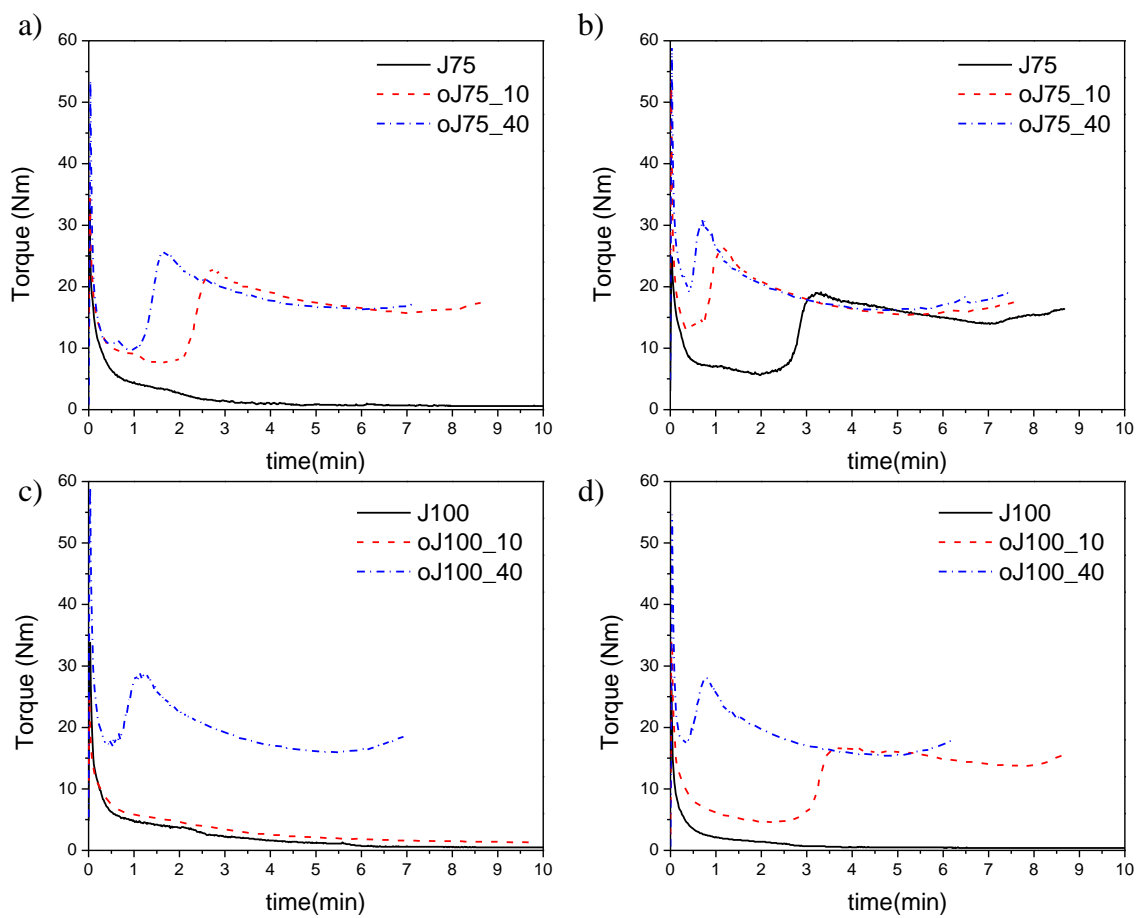


Figure 7.18: Fusion curves of the ternary blends of the J75 series at a) 185 °C and b) 190 °C and the J100 series at c) 185 °C and d) 190 °C.

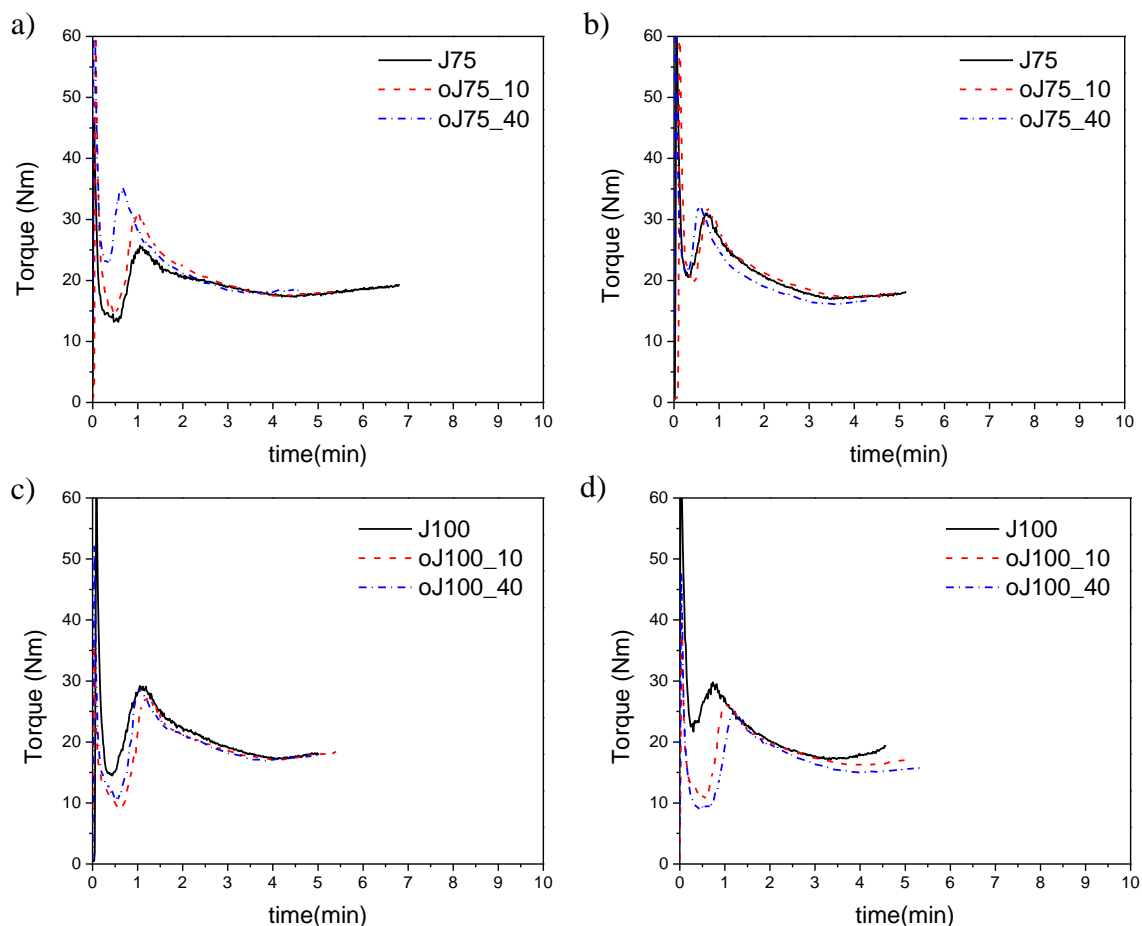


Figure 7.19: Fusion curves of the binary blends of the J75 series at a) 185 °C and b) 190 °C and the J100 series at c) 185 °C and d) 190 °C

7.7 Association interactions using SS NMR

Another method used for determining whether there exists any association between the blend constituents, was SS-NMR. Binary samples were high-speed mixed in a 50:50 wt.% blend ratio at high temperature to ensure that the molten wax completely coated the PVC particles. Two sets of samples were analysed namely the unfused mixed blends as well as a set of Samples that were melt-pressed using a pre-heated hydraulic press at 190 °C and 100 kg/m² for 1 minute. This was done to partially resemble the fusion conditions experienced in the rheometer. The unfused and the partially fused samples were analysed by implementing a T1 rho relaxation SS-NMR experiment. This technique was used to probe the rigidity of the PVC's immediate environment by measuring the amount and time it takes for the methine (CH) and methylene (CH₂) protons of PVC to return to an unexcited state after being pulsed. A high magnetization value observed from a T1 rho relaxation experiment indicates a higher amount of mobile PVC

material present and a low magnetization indicates that these protons were in more rigid domains. Figure 7.20 shows the relaxation curves for the neat PVC, J75 series and J100 series. In Figure 7.20a the neat PVC had a high amount of mobile material and after being melt-pressed (Figure 7.20b) this amount drastically decreased due to the solidification as a result of interparticle fusion. The neat nonpolar J75 blend showed that the PVC was in a highly rigid environment and could have been due to the highly crystalline J75 wax encapsulating the PVC particles resulting in a rigid signal. With the slightly oxidized wax samples the PVC protons are in a less rigid state. After melt-pressing, the oxidized wax blends kept some of the protons appeared to be in a more mobile environment compared to the neat J75 wax blend, but more rigid compared to the neat PVC signals. This suggests that the oxidised wax-coated PVC particles were more mobile compared to the nonpolar wax-coated PVC particles, implying that the oxidation indeed affected chain mobility of the waxes. Improved interactions between wax and PVC could also have been facilitated by oxidation. This effect was greater for the highly oxidized sample (oJ75_40) which could be due to the higher overall polar nature or the smaller interpenetrating molecules.

In Figure 7.20c, the J100 and oJ100_10 samples showed similar trends to that of the J75 sample. The oJ100_40 sample did show some mobile PVC material. This increase in mobile material could only be due to the increase in overall polarity, that ultimately affected the wax-PVC interactions and/or wax mobility as well. It cannot be due to a decrease in wax melting temperature as it melted in the same region as neat J75 (Table 7.3) which did not show association. It is also unlikely to be due to a smaller molecular size which can penetrate into a PVC particle as oJ100_40 had roughly double the molecular size of the J75 series (Table 7.5).

Upon melt-pressing the samples, the PVC is shown to be in an even more rigid environment than neat PVC. This indicates that the constituents possibly completely phase separated and showed no association which can therefore be linked to the combination of smaller sized waxes and polarity playing a role in the melt-pressed samples in the J75 series.

These results showed that the oxidized waxes did not only interact with the CaSt but also to the PVC to some extent as the waxes increase in surfactant-like nature. It would therefore be of great value to do further investigation on binary and ternary blends using this technique.

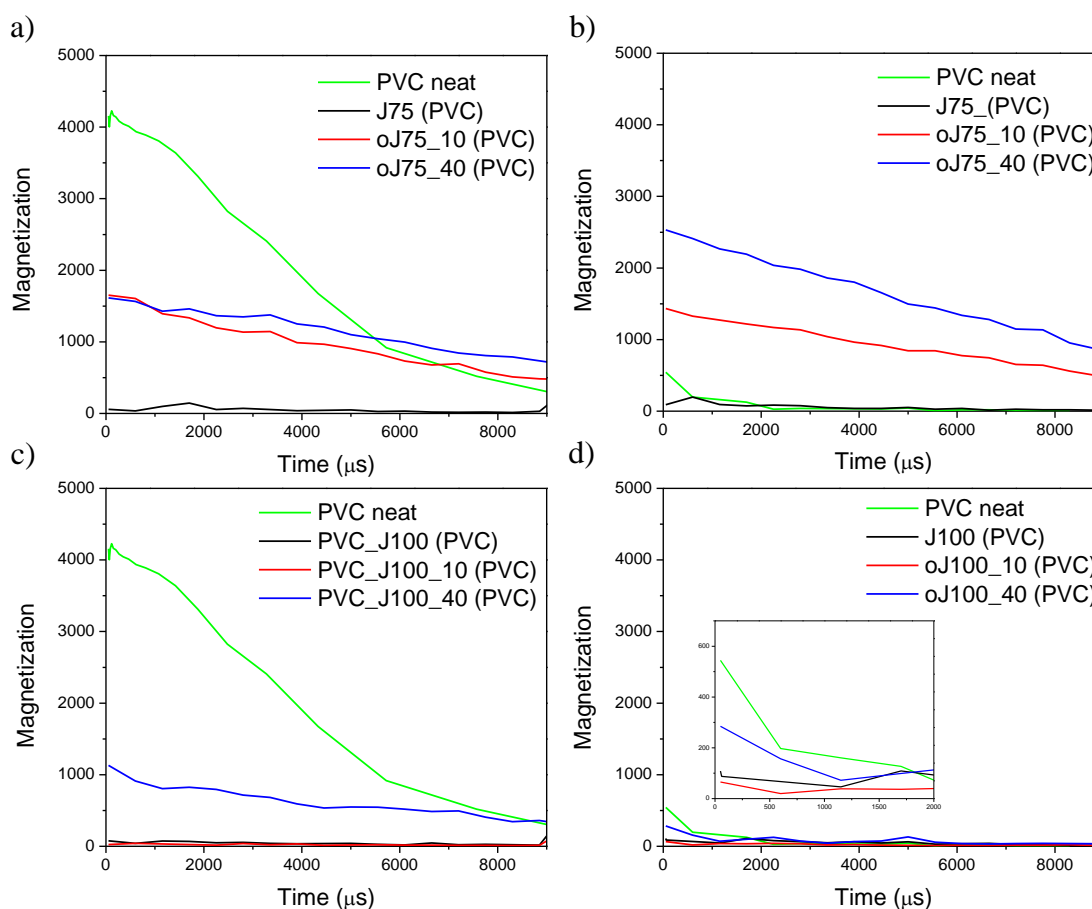


Figure 7.20: T1 rho SS-NMR proton relaxation curves of the unfused blends a) J75 series and c) J100 series and the melt-pressed blends of the b) J75 series and d) J100 series.

7.8 Concluding remarks

Two sets of oxidized waxes were successfully synthesized using controlled ozonolysis of FT waxes. This resulted in two sets of well-defined oxidized waxes with varying degrees of oxidation. The waxes were successfully characterized in stage 1. Stage 1 was further expanded to characterize the degree of oxygenation using HT-SGIC. Some key correlations that were drawn from stage 1 are listed below.

- FTIR experiments correlated well with that of NMR where an increase in oxygenates were seen with an increase in degree of ozonolysis.
- NMR also showed that as ozonolysis progressed, a simultaneous increase of chain end carbons together with an increase in oxygenate carbon signals indicated that as chains were broken up some of them were functionalized.

- HT-SEC results confirmed that chains were broken up and showed an increased molecular weight distribution with increased ozone exposure. This result correlated well with the DSC results which showed a decrease in overall crystallinity as ozonolysis progressed.
- Reverse phase HT-SGIC results gave additional information which corresponded well with the above results and showed that ozonolysis took place across the whole molecular chain regardless of the ESL.
- Normal phase HT-SGIC corresponded well to all the results as it showed that as the samples were oxidized, they formed new species. These results also showed that not all the samples were slightly oxidized but specific molecules were oxidized to a greater extent.

In stage 2, no association was seen in the binary phase. This was unexpected as it was initially thought that degree of oxidation would lead to increased association in this phase as seen from chapter 6. Clear association between all the components were seen in the ternary blends.

Stage 3 showed that all the samples fused completely except for the oJ100_10 sample. This was a similar result as seen for the neat J100 sample. The oJ100_40 sample did however fuse, which showed that oxidation did promote fusion.

Further investigation was done into the fusion behaviour of the samples. These results showed that oxidation did promote fusion. Through combining the results from the screw freezing experiments with the results from the fusion experiments it was possible to expand on the current model proposed by Rabinovitch. Additionally, it was shown that there exists a maximum degree of oxidation where all the samples showed similar fusion behaviour.

Further association studies using solid state NMR also showed that association is influenced by a combination of molecular size and polarity.

General conclusion and suggestions for future studies

Initially, existing models used to explain the lubrication mechanism of uPVC during extrusion were identified. The most recent model suggested that lubricants do not behave as internal or external lubricants but rather as surfactants and slip agents. This model, however, has only been proven by data extrapolation and assumptions on component behaviour were made purely by classifying the compounds according to chemical nature. The aim of this study was therefore to prove or disprove this model by developing a new lubricant tracking method. Since lubricants are defined by the areas at which they associate within the PVC blend and extruder interface, this method was based on the tracking of lubricant sites throughout the processing thereof.

A set of commercial waxes (Wax set 1) were selected to determine the sensitivity of the method and if it was able to differentiate between these various waxes. In stage 1 the waxes were successfully characterized according to their morphological and chemical properties. In stage 2 some differences in behaviour and association of the components were established. Stage 3 also showed some promising results in establishing differences in wax migration behaviour. The method was then used to test an extensive set of waxes. Key characteristics in lubricant behaviour that were revealed at this point, were that:

- CaSt showed some inherent association with PVC.
- Nonpolar wax showed no association with PVC.
- CaSt facilitated the dispersion of nonpolar wax across the PVC particles' surface.
- Polar wax showed some inherent association with PVC.
- Some sort of competition effect exists between CaSt and polar wax.

In Wax set 1, the differences in behaviour that were identified were due to differences in polarity. A new set of waxes (Wax set 2) was selected. In this set a polar group and a nonpolar group were selected to differentiate between microstructural differences within the two main chemical groups. A screw freezing method was also applied at this stage to overcome some problems with the rod extrusion method. This new method eliminated the problem of residual cleaning agent fouling which caused contamination resulting in signal interference during SEM-EDS analyses and additionally, in-extruder sampling was now possible.

One observation was that polar samples of a higher melting nature could fuse under experimental Brabender conditions where high melting nonpolar waxes could not. The

microstructural differences, however, were too vast and no trends in behaviour could be observed.

In the final part of the study a set of oxidized waxes were synthesized (Wax set 3) and subjected to the test method. Ozonolysis showed good control over the oxidation process and resulted in two well-defined sets of oxidized waxes. The characterization stage for this set of waxes was expanded to include HT-SGIC which allowed for some in-depth knowledge on the degree of oxidation on all the samples. During stage 2 it was seen that oxidation was not the only factor to be considered in facilitating association towards PVC as no association was seen for the binary blends. Addition of CaSt showed high levels of association between all the components. In stage 3 the screw freezing results showed that for fusion to occur, all the lubricant has to migrate away from the PVC to allow the PVC particles to compress, allowing interparticle friction and thus fuse. This was counterintuitive as it was thought that an increase in the polarity of the wax would lead to an increased association thereof with PVC which would result in more of the wax being visible in the fused PVC matrix. From the fusion studies it was found that waxes with a higher degree of oxidation led to faster fusion times which showed that those waxes had to migrate out of the PVC's vicinity more quickly. This also led to the conclusion that there exists a limit of oxidation where the migration is so fast that fusion occurs around 1 min irrespective of the molecular size. The combination of CaSt and wax had a greater association with the slightly oxidized metal interface than with the PVC and therefore by further increasing the oxidation the wax migrates away even faster. These conclusions were then applied to the currently accepted model of surfactants and slip agents where it could be seen that by increasing the oxidation state of a wax its surfactant-like properties were also increased together with a loss of slip agent properties. The current model of surfactants and slip agents therefore appears to hold for oxidized waxes as well.

The method that was developed in this study allowed for great insight into the behaviour and migration patterns of waxes. Further investigation should be done to determine the crossover point at which the degree of oxidation versus the molecular weight become the determining factor in fusion behaviour. Another study that could stem from this work and be of great advantage for the industry is whether oxidized wax can be used to substitute an internal lubricant. SS NMR experiments also revealed some interesting findings and should therefore also be expanded to include the neat waxes as well as ternary blends.

List of references

1. Gilbert, M. Crystallinity in poly(vinyl chloride). *J. Macromol. Sci. Part C* **34**, 77–135 (1994).
2. Mohamed, N. A. Antimicrobial itaconimido aromatic hydrazide derivatives for inhibition of the thermal degradation of rigid PVC. *Polym. Bull.* **76**, 2341–2365 (2019).
3. Al-Malack, M. H. Migration of lead from unplasticized polyvinyl chloride pipes. *J. Hazard. Mater.* **82**, 263–274 (2001).
4. Coomans, S. Development and evaluation of an acrylic lubricant for PVC formulations. (MSc Thesis, Hasselt University, 2017).
5. Townsend Solutions. *Global trends in PVC resin applications and additives usage*. (2018).
6. Schiller, M. *PVC additives*. (Hanser publications, 2015).
7. Titow, W. V. *PVC plastics: Properties, processing, and applications*. (Elsevier Ltd, 1990).
8. Mallakpour, S. & Shafiee, E. The synthesis of poly(vinyl chloride) nanocomposite films containing ZrO₂ nanoparticles modified with vitamin B1 with the aim of improving the mechanical, thermal and optical properties. *Des. Monomers Polym.* **20**, 378–388 (2017).
9. Gilbert, M. & Patrick, S. Poly(Vinyl Chloride). in *Brydson's Plastics Materials: Eighth Edition* 329–388 (Elsevier Ltd, 2017).
10. Smallwood, P. V. Vinyl chloride suspension polymerisation and the control of polymer properties. *Makromol. Chemie. Macromol. Symp.* **29**, 1–19 (1989).
11. Gilbert, M. Poly(vinyl chloride)(PVC)-based nanocomposites. in *Advances in Polymer Nanocomposites: Types and Applications* 216–237 (Woodhead Publishing Limited, 2012).
12. Guo, R., Yu, E., Liu, J. & Wei, Z. Agitating transformation during vinyl chloride suspension polymerization: Aggregation morphology and PVC properties. *RSC Adv.* **7**, 24022–24029 (2017).

13. Coelho, J. F. J., Fonseca, A. C., Goncalves, P. M. F. O., Popov, A. V. & Gil, M. H. Particle features and morphology of poly(vinyl chloride) prepared by living radical polymerisation in aqueous media. Insight about particle formation mechanism. *Polymer (Guildf)*. **52**, 2998–3010 (2011).
14. Barclay, L. M. Formation and structure of PVC particles. *Die Angew. Makromol. Chemie* **52**, 1–20 (1976).
15. Varshney, N. Lubrication effects on die plateout in lead stabilised rigid poly(vinyl chloride) extrusion. (PhD Thesis, Loughborough University of Technology, 2004).
16. Summers, J. W. Lubrication mechanism of poly(vinyl chloride) compounds: Changes upon PVC fusion (gelation). *J. Vinyl Addit. Technol.* **11**, 57–62 (2005).
17. Burgess, R. H. *Manufacture and processing of PVC. Construction Materials* (Elsevier Ltd, 2005).
18. Demirci, A., Teke, I., Goger, A., Canbaz, E. & Vlachopoulos, J. Gelation of poly(vinyl chloride) inside a single screw extruder and its effect on product properties. *J. Vinyl Addit. Technol.* **25**, E174–E180 (2019).
19. Tomaszewska, J., Sterzyński, T. & Piszczek, K. Rigid poly(vinyl chloride) (PVC) gelation in the brabender measuring mixer. I. Equilibrium state between sliding, breaking, and gelation of PVC. *J. Appl. Polym. Sci.* **93**, 966–971 (2004).
20. Comeuax, E., Chen, C., Collier, J. & Wesson, R. Fusion study of polyvinyl chloride (PVC): Relation of processing time and processing temperature to the degree of fusion. *Polym. Bull.* **33**, 701–708 (1994).
21. Chen, C. H., Wesson, R. D., Collier, J. R. & Lo, Y. W. Studies of rigid poly(vinyl chloride) (PVC) compounds. II. Determination of the fusion level. *J. Appl. Polym. Sci.* **58**, 1093–1099 (1995).
22. Logan, M. S. & Chung, C. I. Effects of lubricants on the second fusion behavior of rigid polyvinyl chloride. *Polym. Eng. Sci.* **19**, 1110–1116 (1979).
23. Yu, B. Y., Lee, A. R. & Kwak, S. Y. Gelation/fusion behavior of PVC plastisol with a cyclodextrin derivative and an anti-migration plasticizer in flexible PVC. *Eur. Polym. J.* **48**, 885–895 (2012).

24. Pedersen, T. C. Process and material considerations in the industrial application of lubricants in rigid PVC extrusion. *Journal of Vinyl Technology* **6**, 104–109 (1984).
25. Kazmer, D. O., Grosskopf, C. M. & Venoor, V. Vortical fountain flows in plasticating screws. *Polymers (Basel)*. **10**, 1–14 (2018).
26. Saerens, L., Vervaet, C., Remon, J. P. & De Beer, T. Process monitoring and visualization solutions for hot-melt extrusion: A review. *J. Pharm. Pharmacol.* **66**, 180–203 (2014).
27. Shapiro, J., Halmos, A. L. & Pearson, J. R. A. Melting in single screw extruders. *Polymer (Guildf)*. **17**, 905–918 (1976).
28. Lawal, A., Kalyon, D. M. & Yilmazer, U. Extrusion and lubrication flows of viscoplastic fluids with wall slip. *Chem. Eng. Commun.* **122**, 127–150 (1993).
29. Pepper, S. T. The interaction of fillers and lubricants in rigid PVC compositions. (PhD Thesis, Loughborough University of Technology, 1988).
30. Gilbert, M. & Vyvoda, J. C. Thermal analysis technique for investigating gelation of rigid PVC compounds. *Polymer (Guildf)*. **22**, 1134–1136 (1981).
31. Rabinovitch, E. B., Lacatus, E. & Summers, J. W. The lubrication mechanism of calcium stearate/paraffin wax systems in PVC compounds. *J. Vinyl Technol.* **6**, 98–103 (1984).
32. Girois, S., Disson, J. P. & Latil, L. Innovation in antisticking process aids for PVC. *Plast. Rubber Compos.* **34**, 127–133 (2005).
33. King, L. F. & Noël, F. Characterization of lubricants for polyvinyl chloride. *Polym. Eng. Sci.* **12**, 112–119 (1972).
34. Mount, E. M. & Chung, C. I. Melting behavior of solid polymers on a metal surface at processing conditions. *Polym. Eng. Sci.* **18**, 711–720 (1978).
35. Fisch, M. & Bacaloglu, R. Study of additive compatibility with poly(vinyl chloride) (PVC). 2. Dynamic mechanical analysis of PVC lubrication by stearic acid and its derivatives. *Annu. Tech. Conf. - ANTEC, Conf. Proc.* **3**, 3593–3597 (1998).
36. Lindner, R. A., Montgomery, P., Dudek, E. & Bershire, M. External lubricant and stabilizer compositions for rigid vinyl polymers. **71**, (1995).
37. Fredriksen, O. Calcium stearate–stearic acid as lubricants for rigid poly(vinyl chloride)

- (PVC). Capillary rheometer measurements and extrusion properties. *J. Appl. Polym. Sci.* **13**, 69–80 (1969).
38. Hartitz, J. E. The effect of lubricants on the fusion of rigid poly(vinyl chloride). *Polym. Eng. Sci.* **14**, 392–398 (1974).
 39. Treffler, B. Impact of lubricants on processing behaviour of U-PVC. *Plast. Rubber Compos.* **34**, 143–147 (2005).
 40. Spiekermann, R. New lubricants offer higher efficiency in PVC extrusion. *Plast. Addit. Compd.* **10**, (2008).
 41. Sperber, O., Kaminsky, W. & Geißler, A. Structure analysis of paraffin waxes by ¹³C-NMR spectroscopy. *Pet. Sci. Technol.* **23**, 47–54 (2005).
 42. Robertson, D., van Reenen, A. & Duveskog, H. A comprehensive investigation into the structure-property relationship of wax and how it influences the properties of hot melt adhesives. *Int. J. Adhes. Adhes.* **99**, 102559 (2020).
 43. Méndez, C. I. & Ancheyta, J. Kinetic models for Fischer-Tropsch synthesis for the production of clean fuels. *Catal. Today* **353**, 3–16 (2020).
 44. Saeidi, S. *et al.* Mechanisms and kinetics of CO₂ hydrogenation to value-added products: A detailed review on current status and future trends. *Renew. Sustain. Energy Rev.* **80**, 1292–1311 (2017).
 45. Yang, J. Il *et al.* Highly effective cobalt catalyst for wax production in Fischer-Tropsch synthesis. *Fuel* **89**, 237–243 (2010).
 46. Ramachandrarao, B., Naresh, K., Panday, A. & Venkateswarlu Choudary, N. A rapid Py-GC/MS study for linear alpha olefin production from fast pyrolysis of wax and waste polyethylene. *ChemistrySelect* **4**, 13245–13249 (2019).
 47. Lappin, G. R., Nemec, L. H., Sauer, J. D. & Wagner, J. D. Olefins, Higher. in *Kirk-Othmer Encyclopedia of Chemical Technology* 1–20 (John Wiley & Sons, Inc., 2010).
 48. Zawadiak, J., Orlińska, B. & Marek, A. A. Catalytic oxidation of polyethylene with oxygen in aqueous dispersion. *J. Appl. Polym. Sci.* **127**, 976–981 (2013).
 49. Huang, W., Cong, Y. & Wang, X. Preparation of high-hardness oxidized wax. *Pet. Sci. Technol.* **29**, 1825–1829 (2011).

50. Radecka, I. *et al.* Oxidized polyethylene wax as a potential carbon source for PHA production. *Materials (Basel)*. **9**, 1–16 (2016).
51. Hohner, G. Process for the oxidation of polyethylene waxes Patent number: US 6211303 B1. 5 (2001).
52. Zamyatnin, A. A. Amino Acid, Peptide, and Protein Volume in Solution. *Annu. Rev. Biophys. Bioeng.* **13**, 145–165 (1984).
53. Li, H. W., Strauss, H. L. & Snyder, R. G. Differences in the IR methylene rocking bands between the crystalline fatty acids and n-alkanes: Frequencies, intensities, and correlation splitting. *J. Phys. Chem. A* **108**, 6629–6642 (2004).
54. Snyder, R. G., Maroncelli, M., Strauss, H. L. & Hallmark, V. M. Temperature and phase behavior of infrared intensities: The poly (methylene) chain. *J. Phys. Chem.* **90**, 5623–5630 (1986).
55. Hagemann, H., Snyder, R. G., Peacock, A. J. & Mandelkern, L. Quantitative infrared methods for the measurement of crystallinity and its temperature dependence. Polyethylene. *Macromolecules* **22**, 3600–3606 (1989).
56. Motaung, T. E. & Luyt, A. S. Effect of maleic anhydride grafting and the presence of oxidized wax on the thermal and mechanical behaviour of LDPE/silica nanocomposites. *Mater. Sci. Eng. A* **527**, 761–768 (2010).
57. Martinez De Salazar, J. & BaltáCalleja, F. J. Influence of chain defects on the crystallization of polyethylene with reference to crystal size and perfection. *J. Cryst. Growth* **48**, 283–294 (1980).
58. Pereira, A. G. B., Gouveia, R. F., de Carvalho, G. M., Rubira, A. F. & Muniz, E. C. Polymer blends based on PEO and starch: Miscibility and spherulite growth rate evaluated through DSC and optical microscopy. *Mater. Sci. Eng. C* **29**, 499–504 (2009).
59. Vold, R. D., Grandline, J. D. & Vold, M. J. Polymorphic transformations of calcium stearate and calcium stearate monohydrate. *J. Colloid Sci.* **3**, 339–361 (1948).
60. Moore, S. *Global trends in PVC resin applications and additives usage. Townsend solutions.* (2018).
61. Jeon, S., Kim, K.-T. & Choi, K. Migration of DEHP and DINP into dust from PVC

- flooring products at different surface temperature. *Sci. Total Environ.* **547**, 441–446 (2016).
62. Maes, T., Jessop, R., Wellner, N., Haupt, K. & Mayes, A. G. A rapid-screening approach to detect and quantify microplastics based on fluorescent tagging with Nile Red. *Sci. Rep.* **7**, 44501 (2017).
 63. Mao, F. Permeation of hydrocarbons through polyvinyl chloride (PVC) and polyethylene (PE) pipes and pipe gaskets. (PhD Thesis, Iowa state University, 2008).
 64. Yashwant, S. S. PVC pipe market. *Market Research Report* 157 (2019).
 65. M. Moghri, H. Garmabi, M. A. Effects of additives on fusion parameters of rigid PVC formulations. *J Vinyl Addit. Technol* **21**, 129–133 (2008).
 66. Chung, C. I., Hennessey, W. J. & Tusim, M. H. Frictional behavior of solid polymers on a metal surface at processing conditions. *Polym. Eng. Sci.* **17**, 9–20 (1977).
 67. Erwin, L. Theory of mixing sections in single screw extruders. *Polym. Eng. Sci.* **18**, 572–576 (1978).
 68. Varshney, N., Gilbert, M., Walon, M. & Michael, S. Plate-out in PVC extrusion. II. Lubricant effects on the formation of die plate-out in lead-based rigid PVC formulations. *J Vinyl Addit. Technol* **18**, 209–215 (2012).
 69. Webber, G. The origin of multiple DSC melting peaks of Fischer-Tropsch hard waxes. PhD Thesis University of Cape Town. (2009).
 70. Diehl, B. NMR Applications for polymer characterization. in 157–180 (2011).
 71. Cistola, D. P., Small, D. M. & Hamilton, J. A. Carbon 13 NMR studies of saturated fatty acids bound to bovine serum albumin. I. The filling of individual fatty acid binding sites. *J. Biol. Chem.* **262**, 10971–10979 (1987).
 72. Novák, I., Krupa, I. & Luyt, A. S. Modification of a Fischer-Tropsch wax by grafting with maleic anhydride. *J. Appl. Polym. Sci.* **93**, 662–668 (2004).
 73. Ndiripo, A. & Pasch, H. A multidimensional fractionation protocol for the oligomer analysis of oxidized waxes. *Anal. Chim. Acta* **1027**, 137–148 (2018).
 74. Ndiripo, A. & Pasch, H. Comprehensive analysis of oxidized waxes by solvent and thermal gradient interaction chromatography and two-dimensional liquid

- chromatography. *Anal. Chem.* **90**, 7626–7634 (2018).
75. Thermal analysis application brief: Determination of polymer crystallinity by DSC. *TA instruments* (2000).